UNIVERSITY OF CALIFORNIA SAN DIEGO

Organization of Spatiotemporal Frequency Tuning in the Mouse Visual System

A dissertation submitted in partial satisfaction of the requirements for the degree Doctor of Philosophy

in

Neurosciences

by

Helen Wang

Committee in Charge:

Professor Edward Callaway, Chair
Professor Pamela Reinagel, Co-Chair
Professor Judith Fan
Professor John Serences
Professor Tatyana Sharpee

2022

The dissertation of Helen Wang is approved, and it is acceptable in quality and form for publication on microfilm and electronically.

University of California San Diego

2022

DEDICATION

To my parents, Ying Lu and Jinxue Wang, and my siblings Connie and Jack.

To my husband, Lucas Chang.

And to Albert.

TABLE OF CONTENTS

LIST OF ABBREVIATIONS

2PCI	2-photon calcium imaging
AL	Anterolateral area of visual cortex
dLGN	Dorsal lateral geniculate nucleus
ET	Extratelencephalic
HVA	Higher visual area
IT	Intratelencephalic
L4, L5, ect.	Layers 4, 5, etc. of the cerebral cortex
M	Magnocellular
P	Parvocellular
PM	Posteromedial area of visual cortex
ROI	Region of interest
RGC	Retinal ganglion cell
SF	Spatial frequency
STF	Spatiotemporal frequency
TF	Temporal frequency
V1	Primary visual cortex

LIST OF FIGURES

LIST OF TABLES

ACKNOWLEDGEMENTS

I would like to thank Professor Edward Callaway for his steadfast support as the chair of my committee and my mentor. His guidance over the last 5 years has been instrumental to my development as a scientist, directly through meetings and conversations and indirectly through the example he sets forth in lab. I would also like thank all the members of the Callaway lab for their scientific and personal support over the years. In particular, I would like to thank Oyshi Dey and Willian Nuñez Lagos for their invaluable technical support over the course of my dissertation, and Dr. Benjamin K. Stafford for his collaboration on the work detailed in Chapter 2 of this dissertation.

I would also like to thank the UCSD Medical Scientist Training Program (MSTP) and Neurosciences Graduate Program (NGP) for their support and their dedication to creating a community of scientists, physicians, and friends.

Finally, I would like to thank my thesis committee for their feedback and advice over the years and acknowledge funding from the National Institutes of Health that has supported this research.

Chapter 1, in full, is currently being prepared for submission for publication and will include Oyshi Dey and Willian N. Lagos as co-authors and Professor Edward Callaway as the senior author. The dissertation author was the primary investigator and author of this material.

Chapter 2, in full, is currently being prepared for submission for publication and will include Oyshi Dey, Willian N. Lagos, and Noor Behnam as co-authors and Professor Edward Callaway and Dr. Benjamin K. Stafford as co-senior authors. The dissertation author was the primary investigator and author of this material.

VITA

2014 Bachelor of Science, Biomedical Engineering, Yale University

2022 Doctor of Philosophy, Neurosciences, University of California San Diego

PUBLICATIONS

Farina, M. G., Sandhu, M. R. S., Parent, M., Sanganahalli, B. G., Derbin, M., Dhaher, R., **Wang, H.**, Zaveri, H. P., Zhou, Y., Danbolt, N. C., Hyder, F., & Eid, T. (2021). Small loci of astroglial glutamine synthetase deficiency in the postnatal brain cause epileptic seizures and impaired functional connectivity. *Epilepsia*, *62*(11), 2858–2870.

Wang, H., Huang, Y., Coman, D., Munbodh, R., Dhaher, R., Zaveri, H. P., Hyder, F., & Eid, T. (2017). Network evolution in mesial temporal lobe epilepsy revealed by diffusion tensor imaging. *Epilepsia*, *58*(5), 824–834.

Kaneko, G., Sanganahalli, B. G., Groman, S. M., **Wang, H.**, Coman, D., Rao, J., Herman, P., Jiang, L., Rich, K., de Graaf, R. A., Taylor, J. R., & Hyder, F. (2017). Hypofrontality and Posterior Hyperactivity in Early Schizophrenia: Imaging and Behavior in a Preclinical Model. *Biological Psychiatry*, *81*(6), 503–513.

Albright, B., Dhaher, R., **Wang, H.**, Harb, R., Lee, T.-S. W., Zaveri, H., & Eid, T. (2017). Progressive neuronal activation accompanies epileptogenesis caused by hippocampal glutamine synthetase inhibition. *Experimental Neurology*, *288*, 122–133.

Shu, C. Y., Herman, P., Coman, D., Sanganahalli, B. G., **Wang, H.**, Juchem, C., Rothman, D. L., de Graaf, R. A., & Hyder, F. (2016). Brain region and activity-dependent properties of M for calibrated fMRI. *NeuroImage*, *125*, 848–856.

Gruenbaum, S. E., **Wang, H.**, Zaveri, H. P., Tang, A. B., Lee, T.-S. W., Eid, T., & Dhaher, R. (2015). Inhibition of glutamine synthetase in the central nucleus of the amygdala induces anhedonic behavior and recurrent seizures in a rat model of mesial temporal lobe epilepsy. *Epilepsy & Behavior : E&B*, *51*, 96–103.

Dhaher, R., **Wang, H.**, Gruenbaum, S. E., Tu, N., Lee, T.-S. W., Zaveri, H. P., & Eid, T. (2015). Effects of site-specific infusions of methionine sulfoximine on the temporal progression of seizures in a rat model of mesial temporal lobe epilepsy. *Epilepsy Research*, *115*, 45–54.

Dhaher, R., Damisah, E. C., **Wang, H.**, Gruenbaum, S. E., Ong, C., Zaveri, H. P., Gruenbaum, B. F., & Eid, T. (2014). 5-aminovaleric acid suppresses the development of severe seizures in the methionine sulfoximine model of mesial temporal lobe epilepsy. *Neurobiology of Disease*, *67*, 18–23.

FIELDS OF STUDY

Major Field: Neurosciences

Studies in Systems Neurosciences
Professor Edward Callaway

Major Field: Biomedical Engineering

Studies in Biomedical Imaging, Epilepsy
Professors Tore Eid and Fahmeed Hyder

ABSTRACT OF DISSERTATION

Organization of Spatiotemporal Frequency Tuning in the Mouse Visual System

by

Helen Wang

Doctor of Philosophy in Neurosciences

University of California San Diego 2022

Professor Edward Callaway, Chair

Professor Pamela Reinagel, Co-Chair

The mouse visual cortex is a hierarchical and parallel system that consists of primary visual cortex and several higher visual cortical areas. Historically, the low acuity of the mouse visual system garnered little interest, and many early principles of visual and cortical circuits were initially characterized in primate and cat vision. Advances in transgenic mice, genetically

targeted viral tools, and novel recording methods have led to a renewed interest and appreciation in the mouse visual system. A detailed understanding of the mouse visual system on its own, as well as in comparison to other species, is critical for understanding how different visual areas and their cell types work to process visual input. In Chapter 1, two methods for recording single cell activity are used to measure the spatiotemporal frequency and direction tuning properties of deep layer cortical neurons in primary visual cortex and two higher visual cortical areas. While previous studies have characterized the functional tuning properties of superficial (layer 2/3) neurons in mice, the tuning properties of deep layer (layer 5/6) and different projection classes of layer 5 neurons have been less well characterized. We use extracellular electrophysiology and two-photon calcium imaging and find that while deeper layer neurons are specialized for different spatial and temporal frequencies, we also find more overlap in tuning between higher visual areas than previous reports that focused on superficial layers. We also find much stronger direction tuning in extratelencephalically projecting layer 5 neurons compared to intratelencephalically projecting layer 5 neurons in multiple visual areas. In Chapter 2, we characterize two different transgenic mouse lines that label layer 4 neurons in primary visual cortex to determine if a parallel organization for spatial and temporal frequency channels found in primates is conserved in mice. We find that the neurons labeled in layer 4 by these two mouse lines are both morphologically and functionally different, with biases in their laminar location, apical dendrite length, and tuning properties for spatial frequency, temporal frequency, and direction. Together, this dissertation seeks to elucidate an understanding of the functional organization of visual tuning in the mouse visual system, with a focus on layer 4 and layer 5 cell types in primary visual cortex and higher visual cortical areas.

Introduction

Our day-to-day use of visual information is often taken for granted, but if we pause to ask *how* we process a visual scene, the complexity of the task at hand can be appreciated. Even simply looking across a room, the visual scene can be broken down into many components, such as contrasts, edges, colors, speeds, and motion directions that together may form objects or backgrounds. How the visual system identifies these components and transforms them into relevant information is a multifaceted question that continues to intrigue scholars across many disciplines, including neuroscientists, cognitive scientists, and psychologists.

At the level of neurons and circuits, the earliest recordings of individual neurons in cat primary visual cortex (V1) identified neurons that responded to different orientations of bars, indicating that neurons in the brain could be "tuned" to certain visual features (Hubel & Wiesel, 1959). Since then, responses for many other visual features have been identified. Additionally, multiple subcortical and cortical areas work together to segregate and/or combine visual information through various circuits to build both hierarchical and parallel structures for vision. Many principles of neural coding and circuitry, while first characterized in the visual system, have had a profound effect on the way neuroscientists think about the organization of other neural systems, such as coding in other sensory systems as well as computational models of cortical circuitry. At the same time, our understanding of neurons and circuits is still incomplete. And despite many conserved features, not all cortical areas share the same cell types or circuits as the visual system (Tasic et al., 2018). And our existing knowledge of disordered circuits continues to fail to provide effective treatments or clear mechanisms for the symptoms and pathophysiology of many neuropsychiatric disorders.

Of mice and other mammalian visual systems

While historically ignored for its "low-acuity vision," (Hübener, 2003) the mouse visual system today has emerged as a key model for addressing questions about how cell types and circuits are organized across multiple stages of visual processing (Niell & Stryker, 2008). The availability of transgenic tools, novel recording methods, and viral labeling strategies in mice have allowed for the characterization and manipulation of not only increasingly specific cell types, but also simultaneous functional recordings from thousands of cells and multiple regions (Daigle et al., 2018; J. A. Harris et al., 2014, 2019; Siegle et al., 2019; Tasic et al., 2018). While many principles of visual circuits first described in cats and primates are conserved in mice, there are key differences, some of which remain to be resolved. For example, although the overarching hierarchical structure of the visual system is conserved in mice from retina to thalamus to V1 to higher visual areas (HVAs) (Figure 0.1), it is not clear if the HVAs in the mouse visual system play a similar "dorsal" and "ventral" stream role in extrastriate cortex as they have been found to in primates (Glickfeld & Olsen, 2017). In primates, direction selectivity emerges *de novo* in simple cells of V1 and is not found in the earliest stages of visual processing (Livingstone, 1998). However, in mice while direction selectivity can also arise *de novo* in layer 4 cells (Lien & Scanziani, 2018), there are also direction selective retinal ganglion cells (RGCs) and direction selective responses in the dorsal lateral geniculate nucleus (dLGN) that encode direction selectivity much earlier in the visual hierarchy and from which V1 neurons can inherit direction selectivity (Hillier et al., 2017; Huberman et al., 2009; Sun et al., 2006). In both primates and mice, visual areas are retinotopically organized, but unlike primates, mice appear to lack a spatial map for many tuning properties and instead have more of a "salt and pepper" map (Kondo & Ohki, 2016). As new findings emerge, these comparisons present an opportunity to determine

what principles of visual circuitry are conserved across species and/or visual tasks. Where they differ, comparative studies have the potential to reveal alternative strategies for visual processing. In the next sections, I review what is currently understood of the early mouse visual system and its basic functions for processing visual information, highlighting gaps in knowledge and places where comparisons to other mammalian visual systems have fallen short.

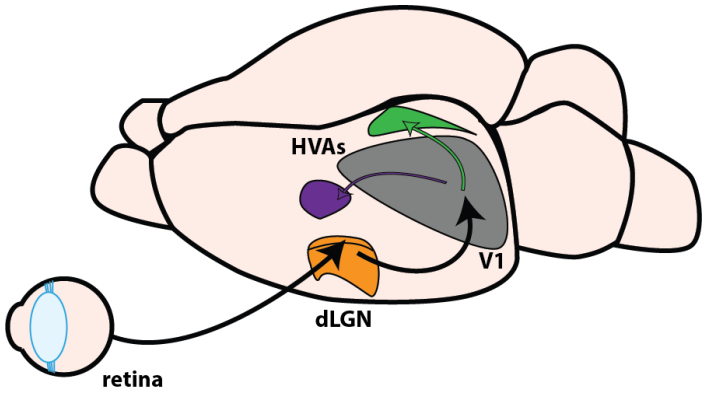

Figure 0.1: Schematic of the retinogeniculocortical pathway in the mouse visual system. Visual input from the retina is transmitted feedforward from retinal ganglion cells (RGCs) to the dorsal lateral geniculate nucleus (dLGN), and then to primary visual cortex (V1). From V1, higher visual areas (HVAs) receive different input from V1 depending on their functional specialization. Here, only 2 HVAs are shown for clarity. Area anterolateral (AL) in purple, and area posteromedial (PM) in green.

Organization of the visual system

Visual processing begins in the retina where neurons respond to relatively simple visual features such as spots of increasing or decreasing light in different parts of the visual field. In the mouse retina, at least 30 types of RGCs tile the visual field, each encoding a parallel visual channel, such as different temporal or spatial frequencies (Baden et al., 2016). Due to anatomical limitations of the optic nerve, these channels cannot represent every visual feature and thus RGCs must encode only the most fundamental features to send to central nervous system targets, such as the dLGN (Nassi & Callaway, 2009). At later stages (V1, extrastriate/higher visual cortical areas), these parallel pathways are combined to represent more complex visual features,

such as orientation, direction, and speed. These transformations from parallel inputs to integrated features are believed to be fundamental to visual processing. The visual system uses multiple strategies to create these transformations including cell type specific connections and hierarchical processing (Felleman & Van Essen, 1991). In addition to this retinogeniculocortical pathway, other visual pathways from the retina exist, such as those from the superior colliculus to thalamus to cortex (Bickford et al., 2015). Anatomical and functional studies in the mouse visual cortex demonstrate that the overarching structure of the retinogeniculocortical pathway is conserved in mice (J. A. Harris et al., 2019; Siegle et al., 2021). However, colliculogeniculate and pulvinar mediated inputs also appear to play a substantial role in both driving and modulating responses, particularly in HVAs, as discussed below.

Functional specialization of higher visual areas

Work in the mouse visual cortex has identified at least 9 HVAs (Garrett et al., 2014; Wang & Burkhalter, 2007). These areas anatomically surround V1 and are thought to be specialized for different visual features and tasks. However, the exact role each HVA plays in processing different visual information remains to be fully elucidated. While each HVA has its own retinotopic map of the visual space, the coverage of visual space is not uniform and is biased depending on the visual area (Garrett et al., 2014), suggesting that certain areas are dedicated to processing information relevant to specific parts of the visual scene (*e.g.* the sky versus the ground) (Saleem, 2020). In terms of responses to classic visual features, such as orientation, spatial frequency (SF), temporal frequency (TF), motion, etc., studies have found biases to these stimuli in varying HVAs (Andermann et al., 2011; Marshel et al., 2011; Sit &

Goard, 2020). More recent studies have also tried to determine how different HVAs and V1 may be involved in different types of visually guided behavioral tasks (Jin & Glickfeld, 2020).

In addition to research determining the role of each HVA in visual processing, there is also extensive research on how each HVA becomes specialized. While our understanding of the differences between HVAs continues to be refined, studies have taken advantage of the existing known differences in tuning of HVAs to draw insights into cortical specialization. Two HVAs that have been particularly fruitful for this are areas anterolateral (AL) and posteromedial (PM) due to their differences in tuning for spatial frequency (SF, cycles per degree (cpd)) and temporal frequency (TF, degrees per second (Hz)). Together, the ratio of TF/SF encode the speed of visual motion. Studies characterizing basic visual tuning have found that AL prefers high TF, low SF, and fast speeds, whereas PM prefers the opposite: low TF, high SF, and slow speeds (Andermann et al., 2011; Marshel et al., 2011). Functional and anatomical studies suggest that these differences are in part inherited from distinct, targeted projections from V1 (Glickfeld et al., 2013; E. J. Kim et al., 2020; M. H. Kim et al., 2018), but potentially also from the pulvinar nucleus of the thalamus (Blot et al., 2021), or from different local computations within each region (Li et al., 2020). None of these proposed mechanisms alone can fully explain the responses of neurons in AL and PM, and much work is still needed to understand the full range of tuning properties in these areas, as well as their behaviorally relevant functions and underlying circuits.

HVAs receive different inputs not only from V1 but also from the pulvinar nucleus of the thalamus (Bennett et al., 2019; Blot et al., 2021; Juavinett et al., 2019). Indirect inputs from the superior colliculus through pulvinar to HVAs may play a strong role in the tuning and response properties of some HVAs (Beltramo & Scanziani, 2019) or certain tuning properties like visual

speed (Tohmi et al., 2014). Inputs from pulvinar to AL versus PM have also been demonstrated to be functionally specialized for SFs and TFs but tuned differently from V1 inputs (Blot et al., 2021). How pulvinar inputs may interact with V1 inputs in HVAs is not well understood, though it has been suggested that pulvinar inputs may integrate both visual and motor signals while V1 inputs are predominantly visual (Blot et al., 2021).

Functional specialization by cell types and classes

The studies discussed previously have primarily focused on area-specific differences in functional tuning. However, within each visual area, there are also multiple cell types that can be divided by laminar location and projection pattern. Within V1, functional studies have demonstrated that layer 5 excitatory neurons with different projection targets (intratelencephalic versus extratelencephalic) are tuned to different visual features, exhibiting biases in their SF and TF tuning that are hypothesized to be related to the processing role of their projection targets (E. J. Kim et al., 2015; Lur et al., 2016). Tracing studies in V1 and other sensory cortices also demonstrate that long range cortical inputs to layer 2/3 and layer 5/6 are biased for "like to like" (*e.g.* layer 2/3 receives more input from other layer 2/3 neurons) (DeNardo et al., 2015; E. J. Kim et al., 2015). While multiple studies have characterized the basic tuning properties of V1 and most HVAs, many of these studies have primarily focused on the tuning properties of neurons in layer 2/3 (Andermann et al., 2011; Marshel et al., 2011; Roth et al., 2012). Studies that measure cell type or projection type differences in functional tuning in deeper layer neurons and in HVAs have been more limited, but their findings suggest circuit-related differences. One study looking at AL and PM layer 5 neurons that provide feedback to V1 found that these feedback neurons were more specialized for SF compared to "neighbor" (putative non-feedback) layer 5 neurons in

these regions (Huh et al., 2018), suggesting differences in visual tuning between neurons that provide cortical feedback versus other neurons. In Chapter 1, I address gaps in our current knowledge of tuning preferences in visual cortical areas by targeting deep layer neurons in V1 and areas AL and PM to determine if excitatory deep layer neurons are also functionally specialized for SF, TF, and speed. Additionally, I use transgenic mouse lines to selectively label and record from intratelencelphalically and extratenencephalically projecting layer 5 cell classes to further differentiate between layer 5 neurons and their tuning properties.

Sampling methods and sampling space

Other considerations in defining an area or neuron and its responses are the sampling method and sampling space. While new electrophysiology and imaging techniques allow scientists to acquire data from up to thousands of neurons simultaneously, each methodology and the method by which this large volume of data is processed has intrinsic limitations and biases. For example, many of the early studies fundamentally characterizing mouse HVAs and their responses were focused on superficial layer 2/3 cells due to limitations in the depth of imaging possible at the time. While laminar electrophysiology probes allow for sampling of neurons deeper in cortex, the population of neurons recorded from can be biased based on how responsive a neuron is and its spiking pattern, which can impact if a given neuron can be "well-isolated" and further analyzed (K. D. Harris et al., 2016). Some visual properties, like speed tuning require sampling from multiple combinations of SF and TFs, which involves large stimulus sets that often must trade off with other features, such as direction or contrast (Priebe et al., 2003). In Chapter 1, by using both extracellular electrophysiology and 2-photon calcium imaging to record tuning responses, I examine how these two different methods may impact the

assessment of tuning properties found in visual areas V1, AL, and PM. I also compare how differences in the range of stimuli sampled may impact the tuning preferences found.

Processing of visual information in the retinogeniculocortical pathway

Visual responses as early as the retina are selective for different visual features. In primates and cats, cells that are tuned to different visual features are segregated through distinct anatomical and cell type specific connections that form "parallel channels." This is most clearly demonstrated by the magnocellular (M) versus parvocellular (P) pathways in the primate retinogeniculocortical system, where each circuit originates from RGCs with different morphology, connections, and functional properties (parasol versus midget RGCs respectively) that project to distinct layers of the dLGN (magnocellular versus parvocellular layers) and V1 (layer 4Cα versus layer 4Cβ) (Callaway, 2005; Nassi & Callaway, 2009). These pathways are thought to be biased for coarse/fast (high TF, low SF) and fine/slow (low TF, high SF) visual information respectively. In mice, evidence for a similar parallel organization of visual information from the retina into layer 4 is lacking, or weak at best. This may be due to less clearly organized anatomical structures for these circuits in mice, making the pathways harder to identify. Transgenic and viral tools that allow for cell type or functional type targeting could potentially help reveal parallel circuits that are otherwise intermingled anatomically. Additionally, the mouse visual system may have adopted other visual processing strategies that differ from those of "high acuity" mammals. Computational models using constrained convolutional neural networks have hypothesized that a more "shallow" hierarchical system with fewer hierarchical steps, like the mouse visual system, may create complex tuning earlier in a hierarchical model compared to "deeper" hierarchical systems, like the primate visual system

(Lindsey et al., 2019). Consistent with this, functional studies have identified a greater diversity of cell types and responses in RGCs, as well as the emergence of "complex" tuning properties, like direction selectivity, at earlier stages of visual processing in mice compared to primates (Baden et al., 2016; Huberman et al., 2009; Marshel et al., 2012).

Inputs and outputs from the dLGN to V1

The strongest evidence for a "parallel" pathway in mice is a circuit originating from direction selective RGCs to the outer, superficial "shell" of the dLGN to layer 1 of V1 that is thought to directly transmit direction selectivity to V1 (Cruz-Martín et al., 2014). However, given the circuity and cell types of the dLGN shell, this circuit may be more analogous to the less understood koniocellular pathway in primates (Bakken et al., 2021; Bickford et al., 2015; Krahe et al., 2011). Rather, "core" dLGN neurons provide the primary thalamic input to layer 4 of V1 in mice. Although cortical neurons in deep layers can receive input from apical dendrites that are present in layer 1, and dLGN axons that branch into layer 6, most of the feedforward input to cortex is believed to come from layer 4 (Felleman & Van Essen, 1991).

The dLGN core consists of neurons tuned to diverse visual features and that exhibit multiple morphologies (Piscopo et al., 2013). However, it remains unclear if there are specific dLGN core cell types in mice, and if different cell types project to specific populations of neurons in layer 4 of V1 through parallel channels. Like V1, the mouse dLGN core lacks a clear anatomical organization for different visual responses and cell types and may have more of a "salt and pepper" tuning map through the dLGN core (Piscopo et al., 2013). Morphologically, Y, X, and W-like cells, which appear morphologically similar to dLGN cell types found in cats, have been identified in mouse dLGN (Friedlander et al., 1981; Krahe et al., 2011). W-like cells

are biased to the shell, while X and Y-like cells are more likely to be found in the core (Krahe et al., 2011). But while these cells in cat dLGN differ in their intrinsic properties and functional tuning for SF and TF, they do not appear to differ substantially in their properties in mice (Friedlander et al., 1981; Krahe et al., 2011). Relatedly, other studies have also failed to find to a strong correlation between response properties and tuning properties in dLGN that would support a simple M versus P pathway analog in mice (*e.g.* transient versus sustained responses and its relation to SF, TF tuning) (Grubb & Thompson, 2003; Piscopo et al., 2013). A recent single cell transcriptomic study of the mouse dLGN also failed to identify distinct core cell types, instead only noting a gradient between core versus shell isolated neurons (Bakken et al., 2021).

One limiting aspect in our understanding of dLGN core types is the still evolving understanding of RGC inputs to mouse dLGN. In mice, there are multiple RGC types and these RGCs can provide input to dLGN neurons in two different modes based on an anatomical tracing study (Rompani et al., 2017). In one mode, more analogous to the primate retinogeniculate system, 1-2 RGC types provide input to a single dLGN neuron, termed "relay mode" (Rompani et al., 2017). In another, termed "combination mode," multiple RGC types provide input to a dLGN neuron (Rompani et al., 2017). However, it is not necessarily the case that all anatomical RGC inputs contribute to the functional properties of the dLGN neurons on which they synapse. A study looking at dLGN neurons that receive anatomically binocular RGC input found that dLGN neurons were functionally dominated by monocular input (Bauer et al., 2021). Modeling of dLGN responses based on RGC responses can also predict dLGN visual responses from a linear combination of around 5 RGC types, with 2 RGC types dominant (Román Rosón et al., 2019). Interestingly, in a study that imaged the tuning properties of RGC boutons in the dLGN, it was found, that while RGC boutons with different tuning properties may converge onto the same

dLGN dendrite, 1-2 of the tuning properties are often shared across the boutons (Liang et al., 2018). Thus, despite diverse anatomical projections, the functional impact of RGC inputs to dLGN neurons may be limited to only a few types of RGCs or a few tuning properties.

Organization of mouse layer 4 in primary visual cortex

While functional studies have identified neurons in V1 that are biased towards different SFs and TFs like those found in the primate M and P pathways (Gao et al., 2010), the RGC and dLGN inputs for V1 neurons with different SF, TF tuning properties have not been characterized in mice. In primates, layer 4 of visual cortex is unique compared to layer 4 of other sensory cortices due to additional laminations that represent the M and P input channels to layer 4Cα and 4Cβ. In mice, however, the question of distinct layer 4 cell types in V1 remains unresolved and overlooked. Transcriptomic studies of cell types in visual cortex conflict on the number of distinct cell "clusters" that are present in layer 4 (Tasic et al., 2016, 2018). In Chapter 2, I address the question of parallel pathways in the mouse visual system by characterizing neurons in the primary input layer of V1, or layer 4. I identify and characterize 2 transgenic mouse lines that label potentially overlapping but biased groups of layer 4 neurons that differ in their visual responses to SF, TF, and direction and in their morphology and depth in cortex.

An appreciation for expected and unexpected functional diversity

As is often the case in biology, for every "principle," there are many exceptions. Principles are useful for organizing how we think about cell types and connectivity, and exceptions can often be frustrating caveats. However, they should also be celebrated for the opportunities they provide to understand how and why differences emerge. This is true when

considering comparisons between the visual systems of different species, as well as when comparing tuning properties across different visual areas and cell types. In this dissertation, I address questions about the organization of neurons in the mouse visual system and their processing of visual speed and other visual features. While these systems have been characterized in the past, incomplete sampling methods have not allowed for a full characterization of all cell types or responses. In Chapter 1, I use two complementary recording technologies, extracellular electrophysiology and 2-photon calcium imaging to examine deep layer cortical neurons in V1 and higher visual areas AL and PM to characterize their responses to spatiotemporal frequencies and speeds. In Chapter 2, I functionally characterize two layer 4 transgenic mouse lines that provide evidence for different functional cell groups in layer 4. Together, these studies contribute toward a greater understanding of the diversity of functional tuning properties across cell types in the mouse visual cortex.

0.1 References

Andermann, M. L., Kerlin, A. M., Roumis, D. K., Glickfeld, L. L., & Reid, R. C. (2011). Functional specialization of mouse higher visual cortical areas. *Neuron*, *72*(6), 1025–1039. https://doi.org/10.1016/j.neuron.2011.11.013

Baden, T., Berens, P., Franke, K., Román Rosón, M., Bethge, M., & Euler, T. (2016). The functional diversity of retinal ganglion cells in the mouse. *Nature*, *529*(7586), 345–350. https://doi.org/10.1038/nature16468

Bakken, T. E., van Velthoven, C. T., Menon, V., Hodge, R. D., Yao, Z., Nguyen, T. N., Graybuck, L. T., Horwitz, G. D., Bertagnolli, D., Goldy, J., Yanny, A. M., Garren, E., Parry, S., Casper, T., Shehata, S. I., Barkan, E. R., Szafer, A., Levi, B. P., Dee, N., Smith, K. A., Sunkin, S. M., Bernard, A., Phillips, J., Hawrylycz, M. J., Koch, C., Murphy, G. J., Lein, E., Zeng, H., & Tasic, B. (2021). Single-cell and single-nucleus RNA-seq uncovers shared and distinct axes of variation in dorsal LGN neurons in mice, non-human primates, and humans. *ELife*, *10*, e64875. https://doi.org/10.7554/eLife.64875

Bauer, J., Weiler, S., Fernholz, M. H. P., Laubender, D., Scheuss, V., Hübener, M., Bonhoeffer, T., & Rose, T. (2021). Limited functional convergence of eye-specific inputs in the retinogeniculate pathway of the mouse. *Neuron*, 1–12. https://doi.org/10.1016/j.neuron.2021.05.036

Beltramo, R., & Scanziani, M. (2019). A collicular visual cortex: Neocortical space for an ancient midbrain visual structure. *Science*, *363*(6422), 64–69. https://doi.org/10.1126/science.aau7052

Bennett, C., Gale, S. D., Garrett, M. E., Newton, M. L., Callaway, E. M., Murphy, G. J., & Olsen, S. R. (2019). Higher-Order Thalamic Circuits Channel Parallel Streams of Visual Information in Mice. *Neuron*, *102*(2), 477-492.e5. https://doi.org/10.1016/j.neuron.2019.02.010

Bickford, M. E., Zhou, N., Krahe, T. E., Govindaiah, G., & Guido, W. (2015). Retinal and Tectal "Driver-Like" Inputs Converge in the Shell of the Mouse Dorsal Lateral Geniculate Nucleus. *Journal of Neuroscience*, *35*(29), 10523–10534. https://doi.org/10.1523/JNEUROSCI.3375-14.2015

Blot, A., Roth, M. M., Gasler, I., Javadzadeh, M., Imhof, F., & Hofer, S. B. (2021). Visual intracortical and transthalamic pathways carry distinct information to cortical areas. *Neuron*, *109*(12), 1996-2008.e6. https://doi.org/10.1016/j.neuron.2021.04.017

Callaway, E. M. (2005). Structure and function of parallel pathways in the primate early visual system. *The Journal of Physiology*, *566*(1), 13–19. https://doi.org/10.1113/jphysiol.2005.088047

Cruz-Martín, A., El-Danaf, R. N., Osakada, F., Sriram, B., Dhande, O. S., Nguyen, P. L., Callaway, E. M., Ghosh, A., & Huberman, A. D. (2014). A dedicated circuit links direction-selective retinal ganglion cells to the primary visual cortex. *Nature*, *507*(7492), 358–361. https://doi.org/10.1038/nature12989

Daigle, T. L., Madisen, L., Hage, T. A., Valley, M. T., Knoblich, U., Larsen, R. S., Takeno, M. M., Huang, L., Gu, H., Larsen, R., Mills, M., Bosma-Moody, A., Siverts, L. A., Walker, M., Graybuck, L. T., Yao, Z., Fong, O., Nguyen, T. N., Garren, E., Lenz, G. H., Chavarha, M., Pendergraft, J., Harrington, J., Hirokawa, K. E., Harris, J. A., Nicovich, P. R., McGraw, M. J., Ollerenshaw, D. R., Smith, K. A., Baker, C. A., Ting, J. T., Sunkin, S. M., Lecoq, J., Lin, M. Z., Boyden, E. S., Murphy, G. J., da Costa, N. M., Waters, J., Li, L., Tasic, B., & Zeng, H. (2018). A Suite of Transgenic Driver and Reporter Mouse Lines with Enhanced Brain-Cell-Type Targeting and Functionality. *Cell*, *174*(2), 465-480.e22. https://doi.org/10.1016/J.CELL.2018.06.035

DeNardo, L. A., Berns, D. S., DeLoach, K., & Luo, L. (2015). Connectivity of mouse somatosensory and prefrontal cortex examined with trans-synaptic tracing. *Nature Neuroscience*, *18*(11), 1687–1697. https://doi.org/10.1038/nn.4131

Felleman, D. J., & Van Essen, D. C. (1991). Distributed hierarchical processing in the primate cerebral cortex. *Cerebral Cortex*, *1*(1), 1–47. https://doi.org/10.1093/cercor/1.1.1-a

Friedlander, M. J., Lin, C. S., Stanford, L. R., & Sherman, S. M. (1981). Morphology of functionally identified neurons in lateral geniculate nucleus of the cat. *Journal of Neurophysiology*, *46*(1), 80–129. https://doi.org/10.1152/jn.1981.46.1.80

Gao, E., DeAngelis, G. C., & Burkhalter, A. (2010). Parallel Input Channels to Mouse Primary Visual Cortex. *Journal of Neuroscience*, *30*(17), 5912–5926. https://doi.org/10.1523/JNEUROSCI.6456-09.2010

Garrett, M. E., Nauhaus, I., Marshel, J. H., & Callaway, E. M. (2014). Topography and Areal Organization of Mouse Visual Cortex. *Journal of Neuroscience*, *34*(37), 12587–12600. https://doi.org/10.1523/JNEUROSCI.1124-14.2014

Glickfeld, L. L., Andermann, M. L., Bonin, V., & Reid, R. C. (2013). Cortico-cortical projections in mouse visual cortex are functionally target specific. *Nature Neuroscience*, *16*(2), 219–226. https://doi.org/10.1038/nn.3300

Glickfeld, L. L., & Olsen, S. R. (2017). Higher-Order Areas of the Mouse Visual Cortex. *Annu. Rev. Vis. Sci*, *3*, 251–273. https://doi.org/10.1146/annurev-vision-102016

Grubb, M. S., & Thompson, I. D. (2003). Quantitative Characterization of Visual Response Properties in the Mouse Dorsal Lateral Geniculate Nucleus. *Journal of Neurophysiology*, *90*(6), 3594–3607. https://doi.org/10.1152/jn.00699.2003

Harris, J. A., Hirokawa, K. E., Sorensen, S. A., Gu, H., Mills, M., Ng, L. L., Bohn, P., Mortrud, M., Ouellette, B., Kidney, J., Smith, K. A., Dang, C., Sunkin, S., Bernard, A., Oh, S. W., Madisen, L., & Zeng, H. (2014). Anatomical characterization of Cre driver mice for neural circuit mapping and manipulation. *Frontiers in Neural Circuits*, *8*(July), 76. https://doi.org/10.3389/fncir.2014.00076

Harris, J. A., Mihalas, S., Hirokawa, K. E., Whitesell, J. D., Choi, H., Bernard, A., Bohn, P., Caldejon, S., Casal, L., Cho, A., Feiner, A., Feng, D., Gaudreault, N., Gerfen, C. R., Graddis, N., Groblewski, P. A., Henry, A. M., Ho, A., Howard, R., Knox, J. E., Kuan, L., Kuang, X., Lecoq,

J., Lesnar, P., Li, Y., Luviano, J., Mcconoughey, S., Mortrud, M. T., Naeemi, M., Ng, L., Oh, S. W., Ouellette, B., Shen, E., Sorensen, S. A., Wakeman, W., Wang, Q., Wang, Y., Williford, A., Phillips, J. W., Jones, A. R., Koch, C., & Zeng, H. (2019). Hierarchical organization of cortical and thalamic connectivity. *Nature*. https://doi.org/10.1038/s41586-019-1716-z

Harris, K. D., Quiroga, R. Q., Freeman, J., & Smith, S. L. (2016). Improving data quality in neuronal population recordings. *Nature Neuroscience*, *19*(9), 1165–1174. https://doi.org/10.1038/nn.4365

Hillier, D., Fiscella, M., Drinnenberg, A., Trenholm, S., Rompani, S. B., Raics, Z., Katona, G., Juettner, J., Hierlemann, A., Rozsa, B., & Roska, B. (2017). Causal evidence for retina-dependent and -independent visual motion computations in mouse cortex. *Nature Neuroscience*, *20*(7), 960–968. https://doi.org/10.1038/nn.4566

Hubel, D. H., & Wiesel, T. N. (1959). Receptive fields of single neurones in the cat's striate cortex. *The Journal of Physiology*, *148*(3), 574–591. https://doi.org/10.1113/jphysiol.1959.sp006308

Hübener, M. (2003). Mouse visual cortex. *Current Opinion in Neurobiology*, *13*(4), 413–420. https://doi.org/10.1016/S0959-4388(03)00102-8

Huberman, A. D., Wei, W., Elstrott, J., Stafford, B. K., Feller, M. B., & Barres, B. A. (2009). Genetic Identification of an On-Off Direction- Selective Retinal Ganglion Cell Subtype Reveals a Layer-Specific Subcortical Map of Posterior Motion. *Neuron*, *62*(3), 327–334. https://doi.org/10.1016/j.neuron.2009.04.014

Huh, C. Y., Peach, J. P., Bennett, C., Vega, R. M., & Hestrin, S. (2018). Feature-Specific Organization of Feedback Pathways in Mouse Visual Cortex. *Current Biology*, *28*, 114-120.e5. https://doi.org/10.1016/j.cub.2017.11.056

Jin, M., & Glickfeld, L. L. (2020). Mouse Higher Visual Areas Provide Both Distributed and Specialized Contributions to Visually Guided Behaviors. *Current Biology*, *30*(23), 4682-4692.e7. https://doi.org/10.1016/j.cub.2020.09.015

Juavinett, A. L., Kim, E. J., Collins, H. C., & Callaway, E. M. (2019). A systematic topographical relationship between mouse lateral posterior thalamic neurons and their visual cortical projection targets. *Journal of Comparative Neurology*, *528*(1), 99–111. https://doi.org/10.1002/cne.24737

Kim, E. J., Juavinett, A. L., Kyubwa, E. M., Jacobs, M. W., & Callaway, E. M. (2015). Three Types of Cortical Layer 5 Neurons That Differ in Brain-wide Connectivity and Function. *Neuron*, *88*(6), 1253–1267. https://doi.org/10.1016/j.neuron.2015.11.002

Kim, E. J., Zhang, Z., Huang, L., Ito-Cole, T., Jacobs, M. W., Juavinett, A. L., Senturk, G., Hu, M., Ku, M., Ecker, J. R., & Callaway, E. M. (2020). Extraction of Distinct Neuronal Cell Types from within a Genetically Continuous Population. *Neuron*, *107*(2), 274-282.e6. https://doi.org/10.1016/j.neuron.2020.04.018

Kim, M. H., Znamenskiy, P., Iacaruso, M. F., & Mrsic-Flogel, T. D. (2018). Segregated Subnetworks of Intracortical Projection Neurons in Primary Visual Cortex. *Neuron*, *100*(6), 1313-1321.e6. https://doi.org/10.1016/j.neuron.2018.10.023

Kondo, S., & Ohki, K. (2016). Laminar differences in the orientation selectivity of geniculate afferents in mouse primary visual cortex. *Nature Neuroscience*, *19*(2), 316–319. https://doi.org/10.1038/nn.4215

Krahe, T. E., El-Danaf, R. N., Dilger, E. K., Henderson, S. C., & Guido, W. (2011). Morphologically distinct classes of relay cells exhibit regional preferences in the dorsal lateral geniculate nucleus of the mouse. *Journal of Neuroscience*, *31*(48), 17437–17448. https://doi.org/10.1523/JNEUROSCI.4370-11.2011

Li, J. Y., Hass, C. A., Matthews, I., Kristl, A. C., & Glickfeld, L. L. (2020). *Distinct recruitment of feed-forward and recurrent pathways across higher-order areas of mouse visual cortex* [Preprint]. Neuroscience. https://doi.org/10.1101/2020.09.24.312140

Liang, L., Fratzl, A., Goldey, G., Ramesh, R. N., Sugden, A. U., Morgan, J. L., Chen, C., & Andermann, M. L. (2018). A Fine-Scale Functional Logic to Convergence from Retina to Thalamus. *Cell*, *173*(6), 1343-1355.e24. https://doi.org/10.1016/j.cell.2018.04.041

Lien, A. D., & Scanziani, M. (2018). Cortical direction selectivity emerges at convergence of thalamic synapses. *Nature*, 1. https://doi.org/10.1038/s41586-018-0148-5

Lindsey, J., Ocko, S. A., Ganguli, S., & Deny, S. (2019). A unified theory of early visual representations from retina to cortex through anatomically constrained deep cnNs. *7th International Conference on Learning Representations, ICLR 2019*. https://github.com/ganguli-lab/RetinalResources.

Livingstone, M. S. (1998). Mechanisms of direction selectivity in macaque V1. *Neuron*, *20*(3), 509–526. https://doi.org/10.1016/S0896-6273(00)80991-5

Lur, G., Vinck, M. A., Tang, L., Cardin, J. A., & Higley, M. J. (2016). Projection-Specific Visual Feature Encoding by Layer 5 Cortical Subnetworks. *Cell Reports*, *14*(11), 2538–2545. https://doi.org/10.1016/j.celrep.2016.02.050

Marshel, J. H., Garrett, M. E., Nauhaus, I., & Callaway, E. M. (2011). Functional specialization of seven mouse visual cortical areas. *Neuron*, *72*(6), 1040–1054. https://doi.org/10.1016/j.neuron.2011.12.004

Marshel, J. H., Kaye, A. P., Nauhaus, I., & Callaway, E. M. (2012). Anterior-Posterior Direction Opponency in the Superficial Mouse Lateral Geniculate Nucleus. *Neuron*, *76*(4), 713–720. https://doi.org/10.1016/j.neuron.2012.09.021

Nassi, J. J., & Callaway, E. M. (2009). Parallel processing strategies of the primate visual system. *Nature Reviews Neuroscience*, *10*(5), 360–372. https://doi.org/10.1038/nrn2619

Niell, C. M., & Stryker, M. P. (2008). Highly Selective Receptive Fields in Mouse Visual Cortex. *Journal of Neuroscience*, *28*(30), 7520–7536. https://doi.org/10.1523/JNEUROSCI.0623-08.2008

Piscopo, D. M., El-Danaf, R. N., Huberman, A. D., & Niell, C. M. (2013). Diverse Visual Features Encoded in Mouse Lateral Geniculate Nucleus. *Journal of Neuroscience*, *33*(11), 4642–4656. https://doi.org/10.1523/JNEUROSCI.5187-12.2013

Priebe, N. J., Cassanello, C. R., & Lisberger, S. G. (2003). The neural representation of speed in macaque area MT/V5. *The Journal of Neuroscience*, *23*(13), 5650–5661. https://doi.org/23/13/5650 [pii]

Román Rosón, M., Bauer, Y., Kotkat, A. H., Berens, P., Euler, T., & Busse, L. (2019). Mouse dLGN Receives Functional Input from a Diverse Population of Retinal Ganglion Cells with Limited Convergence. *Neuron*. https://doi.org/10.1016/j.neuron.2019.01.040

Rompani, S. B., Müllner, F. E., Wanner, A., Zhang, C., Roth, C. N., Yonehara, K., & Roska, B. (2017). Different Modes of Visual Integration in the Lateral Geniculate Nucleus Revealed by Single-Cell-Initiated Transsynaptic Tracing. *Neuron*, *93*(4), 767-776.e6. https://doi.org/10.1016/j.neuron.2017.01.028

Roth, M. M., Helmchen, F., & Kampa, B. M. (2012). Distinct Functional Properties of Primary and Posteromedial Visual Area of Mouse Neocortex. *Journal of Neuroscience*, *32*(28), 9716–9726. https://doi.org/10.1523/JNEUROSCI.0110-12.2012

Saleem, A. B. (2020). Two stream hypothesis of visual processing for navigation in mouse. *Current Opinion in Neurobiology*, *64*(LM), 70–78. https://doi.org/10.1016/j.conb.2020.03.009

Siegle, J. H., Jia, X., Durand, S., Gale, S., Bennett, C., Graddis, N., Heller, G., Ramirez, T. K., Choi, H., Luviano, J. A., Groblewski, P. A., Ahmed, R., Arkhipov, A., Bernard, A., Billeh, Y. N., Brown, D., Buice, M. A., Cain, N., Caldejon, S., Casal, L., Cho, A., Chvilicek, M., Cox, T. C., Dai, K., Denman, D. J., de Vries, S. E. J., Dietzman, R., Esposito, L., Farrell, C., Feng, D., Galbraith, J., Garrett, M., Gelfand, E. C., Hancock, N., Harris, J. A., Howard, R., Hu, B., Hytnen, R., Iyer, R., Jessett, E., Johnson, K., Kato, I., Kiggins, J., Lambert, S., Lecoq, J., Ledochowitsch, P., Lee, J. H., Leon, A., Li, Y., Liang, E., Long, F., Mace, K., Melchior, J., Millman, D., Mollenkopf, T., Nayan, C., Ng, L., Ngo, K., Nguyen, T., Nicovich, P. R., North, K., Ocker, G. K., Ollerenshaw, D., Oliver, M., Pachitariu, M., Perkins, J., Reding, M., Reid, D., Robertson, M., Ronellenfitch, K., Seid, S., Slaughterbeck, C., Stoecklin, M., Sullivan, D., Sutton, B., Swapp, J., Thompson, C., Turner, K., Wakeman, W., Whitesell, J. D., Williams, D., Williford, A., Young, R., Zeng, H., Naylor, S., Phillips, J. W., Reid, R. C., Mihalas, S., Olsen, S. R., & Koch, C. (2021). Survey of spiking in the mouse visual system reveals functional hierarchy. *Nature*, *592*(7852), 86–92. https://doi.org/10.1038/s41586-020-03171-x

Siegle, J. H., Jia, X., Durand, S., Gale, S., Bennett, C., Graddis, N., Heller, G., Ramirez, T. K., Choi, H., Luviano, J. A., Groblewski, P. A., Ahmed, R., Arkhipov, A., Bernard, A., Billeh, Y. N., Brown, D., Buice, M. A., Cain, N., Caldejon, S., Casal, L., Cho, A., Chvilicek, M., Cox, T. C., Dai, K., Denman, D. J., Vries, S. E. J. de, Dietzman, R., Esposito, L., Farrell, C., Feng, D., Galbraith, J., Garrett, M., Gelfand, E. C., Hancock, N., Harris, J. A., Howard, R., Hu, B., Hytnen,

R., Iyer, R., Jessett, E., Johnson, K., Kato, I., Kiggins, J., Lambert, S., Lecoq, J., Ledochowitsch, P., Lee, J. H., Leon, A., Li, Y., Liang, E., Long, F., Mace, K., Melchior, J., Millman, D., Mollenkopf, T., Nayan, C., Ng, L., Ngo, K., Nguyen, T., Nicovich, P. R., North, K., Ocker, G. K., Ollerenshaw, D., Oliver, M., Pachitariu, M., Perkins, J., Reding, M., Reid, D., Robertson, M., Ronellenfitch, K., Seid, S., Slaughterbeck, C., Stoecklin, M., Sullivan, D., Sutton, B., Swapp, J., Thompson, C., Turner, K., Wakeman, W., Whitesell, J. D., Williams, D., Williford, A., Young, R., Zeng, H., Naylor, S., Phillips, J. W., Reid, R. C., Mihalas, S., Olsen, S. R., & Koch, C. (2019). A survey of spiking activity reveals a functional hierarchy of mouse corticothalamic visual areas. *BioRxiv*, 805010. https://doi.org/10.1101/805010

Sit, K. K., & Goard, M. J. (2020). Distributed and retinotopically asymmetric processing of coherent motion in mouse visual cortex. *Nature Communications*, *11*(1), 1–14. https://doi.org/10.1038/s41467-020-17283-5

Sun, W., Deng, Q., Levick, W. R., & He, S. (2006). ON direction-selective ganglion cells in the mouse retina. *Journal of Physiology*, *576*(1), 197–202. https://doi.org/10.1113/jphysiol.2006.115857

Tasic, B., Menon, V., Nguyen, T. N., Kim, T. K., Jarsky, T., Yao, Z., Levi, B., Gray, L. T., Sorensen, S. A., Dolbeare, T., Bertagnolli, D., Goldy, J., Shapovalova, N., Parry, S., Lee, C., Smith, K., Bernard, A., Madisen, L., Sunkin, S. M., Hawrylycz, M., Koch, C., & Zeng, H. (2016). Adult mouse cortical cell taxonomy revealed by single cell transcriptomics. *Nature Neuroscience*, *19*(2), 335–346. https://doi.org/10.1038/nn.4216

Tasic, B., Yao, Z., Graybuck, L. T., Smith, K. A., Nguyen, T. N., Bertagnolli, D., Goldy, J., Garren, E., Economo, M. N., Viswanathan, S., Penn, O., Bakken, T., Menon, V., Miller, J., Fong, O., Hirokawa, K. E., Lathia, K., Rimorin, C., Tieu, M., Larsen, R., Casper, T., Barkan, E., Kroll, M., Parry, S., Shapovalova, N. V., Hirschstein, D., Pendergraft, J., Sullivan, H. A., Kim, T. K., Szafer, A., Dee, N., Groblewski, P., Wickersham, I., Cetin, A., Harris, J. A., Levi, B. P., Sunkin, S. M., Madisen, L., Daigle, T. L., Looger, L., Bernard, A., Phillips, J., Lein, E., Hawrylycz, M., Svoboda, K., Jones, A. R., Koch, C., & Zeng, H. (2018). Shared and distinct transcriptomic cell types across neocortical areas. *Nature*, *563*(7729), 72–78. https://doi.org/10.1038/s41586-018-0654-5

Tohmi, M., Meguro, R., Tsukano, H., Hishida, R., & Shibuki, K. (2014). The extrageniculate visual pathway generates distinct response properties in the higher visual areas of mice. *Current Biology*, *24*(6), 587–597. https://doi.org/10.1016/j.cub.2014.01.061

Wang, Q., & Burkhalter, A. (2007). Area map of mouse visual cortex. *Journal of Comparative Neurology*, *502*(3), 339–357. https://doi.org/10.1002/cne.21286

Chapter 1. Diversity in spatial frequency, temporal frequency and speed tuning across mouse visual cortical areas and layers

1.1 Abstract

The mouse visual system consists of several visual cortical areas thought to be specialized for different visual features and/or tasks. Previous studies have revealed differences between primary visual cortex (V1) and other higher visual areas, namely anterolateral (AL) and posteromedial (PM), and their tuning preferences for spatial and temporal frequency. However, these differences have primarily been characterized using methods that are biased towards superficial layers of cortex, such as 2-photon calcium imaging. Fewer studies have investigated cell types in deeper layers of these areas and their tuning preferences. Because superficial versus deep layer neurons and different types of deep layer neurons are known to have different feedforward and feedback inputs and outputs, comparing the tuning preferences of these groups is important for understanding cortical visual information processing. In this study, we used extracellular electrophysiology and 2-photon calcium imaging targeted towards two different layer 5 cell classes to characterize their tuning properties in V1, AL, and PM. We find that deep layer neurons, similar to superficial layer neurons, are also specialized for different spatial and temporal frequencies, with the strongest differences between AL-V1 and AL-PM, but not V1-PM. However, we note that the deep layer neuron populations preferred a larger range of SFs and TFs compared to previous studies. We also find that extratelencephalically projecting layer 5 neurons are more direction selective than intratelencephalically projecting layer 5 neurons.

1.2 Introduction

A fundamental principle of mammalian visual systems is the specialization of visual cortical areas for processing different types of visual features (Mishkin et al., 1983; Nassi and Callaway, 2009). This specialization is thought to arise from differential sampling of inputs from the primary visual cortex, but potentially also from higher order visual thalamus and/or differences in local computations (Nassi and Callaway, 2009; Lyon et al., 2010; Glickfeld and Olsen, 2017; Li et al., 2020). In the mouse visual system, there are at least 9 different higher visual areas (HVAs) that have been identified by functional and anatomical methods (Wang and Burkhalter, 2007; Garrett et al., 2014; Glickfeld and Olsen, 2017). Although the visual information processing roles of these areas are still largely unclear, previous studies have reported that these areas contain populations of neurons that are biased in their tuning for spatial and temporal visual features, such as spatial frequency (SF), temporal frequency (TF), and/or speed (TF/SF), suggesting functional specialization (Andermann et al., 2011; Marshel et al., 2011; Roth et al., 2012).

Past studies have focused on two higher mouse visual cortical areas, anterolateral (AL) and posteromedial (PM), due to reports of strong biases in their preferred visual responses to SF, TF, and speed. AL appears to prefer high TF, low SF, or fast speeds, while PM appears to prefer low TF and high SF, or slow speeds (Andermann et al., 2011; Marshel et al., 2011; Roth et al., 2012). These biases in tuning between AL and PM have made them the subject of frequent comparative studies that examine how cortical specialization may arise from pre-defined inputs, versus *de novo* computations. For example, it has been suggested that the specialization found in AL and PM for SF, TF, and speed arises from segregated inputs from V1 to AL and PM

(Glickfeld et al., 2013), and that V1 neurons that are AL versus PM-projecting have differential gene expression (Kim et al., 2020).

Fewer studies have investigated if neurons in deeper layers of AL and PM exhibit similar biases in tuning. Superficial versus deep cortical layers are known to play different roles in cortical circuit computations, such as receiving different feedforward and feedback inputs, as well as targeting different output regions (DeNardo et al., 2015; Kim et al., 2015; Harris et al., 2019). Additionally, excitatory neurons in layers 5 and 6 can be further divided into 2 major classes based on their outputs, either extratelencephalically projecting (ET) or intratelencephalically projecting (IT) (Baker et al., 2018). In V1, previous studies have demonstrated that different layer 5 classes exhibit different projection patterns, morphology, and responses to visual stimuli (Kim et al., 2015; Lur et al., 2016). For example, layer 5 ET (L5ET) neurons labeled by the Glt25d2-Cre mouse line are tuned to faster TFs compared to layer 5 IT (L5IT) neurons labeled by the Tlx3-Cre mouse line (Kim et al., 2015). In a different study, layer 5 neurons providing feedback from AL or PM to V1 had biases in their preferred SF, with AL feedback neurons preferring low SFs and PM feedback neurons preferring high SFs (Huh et al., 2018). Interestingly, when measuring the preferred SF and TF of L5 neurons in AL and PM that did not directly project to V1 (termed “neighbors” in Huh et al.), smaller differences in preferred SF and TF were found (Huh et al., 2018). Thus, L5IT neurons, especially those that send targeted “like-to-like” feedback to V1 (Kim et al., 2020) may be functionally specialized in specific HVAs, but L5ET neurons may exhibit different tuning preferences.

Here, we used laminar extracellular electrophysiology with high-density electrode arrays and 2-photon calcium imaging (2PCI) to look across cortical areas, layers, and cell classes to determine if tuning properties in V1, AL or PM differ between superficial versus deep layers and

whether neurons in deep layers of V1, AL and PM differ from each other. From electrophysiology recordings, we find a greater diversity of tuning properties in AL and PM than previously found with superficial layer 2PCI studies. We also conducted 2PCI of genetically-targeted layer 5 excitatory neuron classes in V1, AL and PM and found differences in their preferred visual responses that were not previously revealed from V1 or superficial layer studies. Together, these results demonstrate that, while biases exist in the overall tuning preferences of AL and PM, layer and cell type specific diversity can be found within each of these regions that do not allow AL and PM to be simply classified based on their visual response properties to different SFs and TFs.

1.3 Methods

To examine the visual response properties of neurons across different layers of visual cortex, we used laminar extracellular electrophysiology recording probes (Du et al., 2011) to record from visual cortical areas V1, AL, and PM. To further characterize distinct layer 5 cell classes, we also injected Cre-dependent AAVs expressing GCaMP6s into V1, AL or PM of either Tlx3-Cre (L5IT) (Gerfen et al., 2013) or Npr3-Cre-NEO-IRES (L5ET) (Daigle et al., 2018) mice (Figure 1.1a schematic) and used 2PCI to record their visual responses. Laminar locations of electrode contacts in electrophysiology studies were identified using current source density (CSD) analysis (Figure 1.1b) (Pettersen et al., 2006). Electrophysiology and imaging locations in V1, AL and PM were guided by intrinsic signal imaging (ISI) maps overlaid on images of the surface blood vessels in each mouse (Figure 1.1d) (Juavinett et al., 2016). Trial responses to different visual stimuli presented were then averaged over the stimulus presentation window to calculate the mean response to each condition (Figure 1.1c and e).

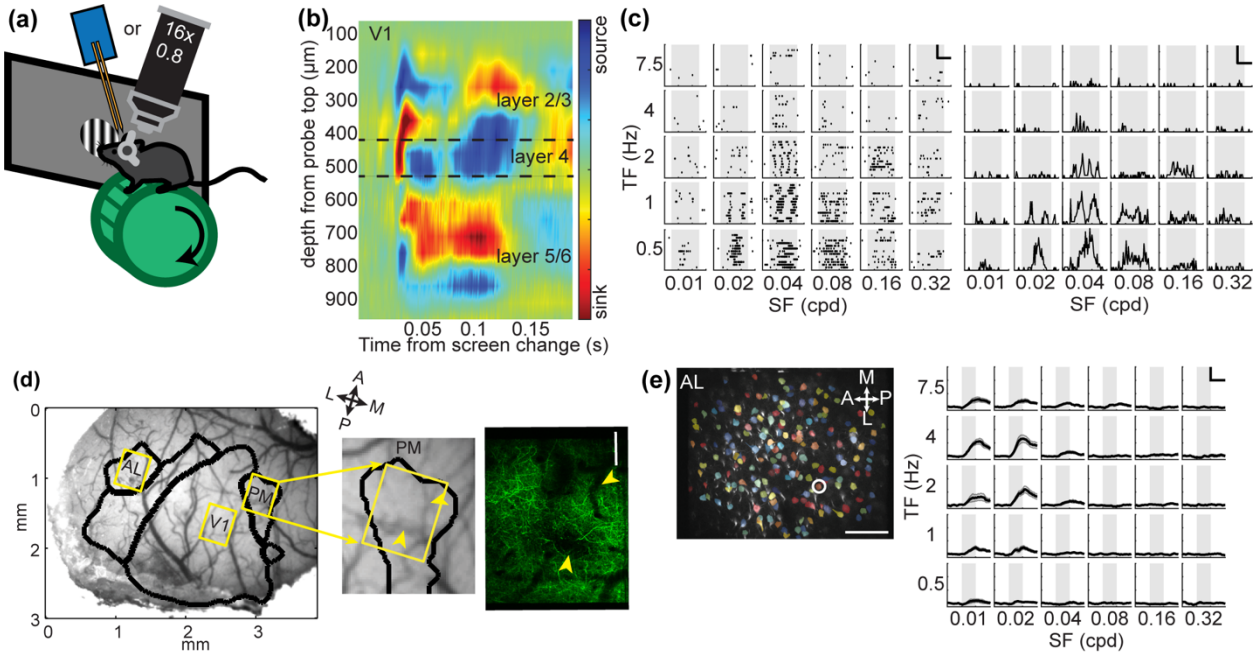

Figure 1.1: Identification of visual cortical areas and layers for electrophysiology and imaging experiments. (a) Experimental setup. (b) Example CSD from a V1 electrophysiology experiment with laminar borders outlined. Granular layers (layer 4) were identified as the 2-3 channels (~100-150 µm) that spanned the earliest current sink following the screen change. (c) Example spike raster (left) and mean peri-stimulus time histogram (right) of responses to different SFs and TFs presented at the neuron's preferred direction. Gray shading represents the stimulus presentation window. Scale bars: left y= 5 trials, x=1 second; right y=10 Hz, x= 1 second. (d) Example blood vessel map overlaid with HVA borders generated using ISI. Sample field of views (FOVs) from imaging are highlighted in yellow and were identified by matching up blood vessel patterns at the surface of each FOV to ISI maps. Scale bar = 100 µm. (e) Left: Sample FOV at layer 5 imaging depth. Segmented ROI masks are pseudo-colored randomly. Scale bar = 100 µm. Right: averaged dF/F traces of circled ROI and it's responses to SFs and TFs at it's preferred direction. Shaded gray box represents the stimulus presentation window and gray shading around black mean dF/F trace represents the standard error (sem). Scale bar y=2 dF/F, x= 2 seconds. Abbreviations: TF = temporal frequency, SF = spatial frequency, cpd = cycles per degree, dF/F = change in fluorescence from baseline divided by baseline fluorescence, DV = dorsoventral, A = anterior, P = posterior, M = medial, L = lateral.

Animals

All experiments and procedures followed procedures approved by the Salk Animal Care and Use Committee. Male and female mice were used for all experiments. For extracellular electrophysiology experiments, Nr5a1-Cre, Scnn1a-Tg3-Cre, PV-Cre, transgenic mice and C57BLJ wildtype mice were used and ranged in age from 70-139 days. For 2PCI experiments,

Tlx3-Cre and Npr3-Cre-NEO-IRES mice were used and ranged in age from 79-119 days. See Supporting Table S1.1 and Supporting Table S1.2 for mice used in each experiment.

Surgeries and viral injections

For all surgical procedures, mice were anesthetized with either isoflurane (0.5%-2%) or a ketamine/xylazine cocktail (100 mg/kg ketamine, 10 mg/kg xylazine) and secured in a stereotaxic frame. Mice were implanted with a custom-built circular headframe centered over the left hemisphere. For surgeries that involved craniotomies >1 mm, such as cranial window implant or prior to electrophysiology recording, carprofen (5 mg/kg) and dexamethasone (2 mg/kg) were administered prior to surgery. For all surgeries, animals were given analgesics (buprenorphine SR, 0.5-1.0 mg/kg, SQ) at the end of the procedure. Some animals were also given ibuprofen medicated water (0.11 mg/mL) or enrofloxacin medicated water (0.28 mg/mL).

For all surgical procedures, mice were anesthetized with either isoflurane (0.5%-2%) or a ketamine/xylazine cocktail (100 mg/kg ketamine, 10 mg/kg xylazine) and secured in a stereotaxic frame. Mice were implanted with a custom-built circular headframe centered over the left hemisphere. For surgeries that involved craniotomies >1 mm, such as cranial window implant or prior to electrophysiology recording, carprofen (5 mg/kg) and dexamethasone (2 mg/kg) were administered prior to surgery. For all surgeries, animals were given analgesics (buprenorphine SR, 0.5-1.0 mg/kg, SQ) at the end of the procedure. Some animals were also given ibuprofen medicated water (0.11 mg/mL) or enrofloxacin medicated water (0.28 mg/mL).

For electrophysiology, a subset of mice used in this analysis were injected with AAV5-EF1a-DIO-eNpHR3.0-eYFP (3-4e12 GC/ml, UNC), AAV5-EF1a-DIO-hChR2(H134R)-eYFP (Addgene #20298) (4E12 GC/mL, UNC), or AAV1-EF1a-DIO-hChR2(H134R)-

eYFP.WPRE.hGH (Addgene #20298) (3.5E12 GC/mL, Addgene) mixed 1:1 or 2:1 with AAV8-CAG-mRuby (2.4E12 GC/mL, Salk Vector Core) for a total volume of 100-275 nL in V1 at 300-500 μm below the surface, 3-6 weeks prior to headframe implantation. Following headframe implantation, ISI was performed as described in previous publications to identify the location and retinotopy of V1 and HVAs (Juavinett et al., 2016). ISI maps were overlaid on images of cortical surface blood vasculature to target electrophysiology probe insertions (Figure 1.1d). For 2PCI experiments, ISI maps were used to guide injections of AAV1-Syn-Flex-GCaMP6s-WPRE-SV40 (Addgene #100845) (100-150 nL, 4E12-8E12 GC/ml, Addgene) into the centers of V1, AL and PM at a depth of ~500-550 μm to target layer 5 neurons through a 4-5 mm wide craniotomy (Figure 1.1d). Following injections, the craniotomy was covered with a glass coverslip (4-5 mm) (Warner Instruments) mounted on a custom-built ring and sealed to the rest of the headframe with dental cement. Animals were allowed to recover while the virus was expressed over ~2 weeks.

In vivo electrophysiology

Mice were acclimated to the running wheel and visual stimulus setup through 2-3 days of training sessions (15 minutes and up to 1.5 hour) prior to recordings, and given 1-3 days to recover from ISI procedures. On the day of the recording, a ~1.5 mm craniotomy was performed over V1, AL and PM. Craniotomies were targeted based on alignment of ISI maps to blood vessel patterns in the brain surface and targeted to the center of the retinotopic map of each area. Mice were given ~1.5-2 hours to recover following craniotomies and prior to the start of recording. Mice were head-fixed to the recording setup and allowed to freely run on the running wheel. Their running speed was recorded using a rotary encoder. During each recording session,

1-2 regions were targeted with silicon microprobes. Typically, regions AL and PM were recorded during 1 session, and then V1 recorded from the following day. Each microprobe contained 64-128 channels across 1-2 shanks (probe configurations 64D, 128AN, 128M) (Du et al., 2011; Shobe et al., 2015). Each shank contained channels that covered a vertical span of ~1 mm to ensure that all layers of the cortex could be recorded simultaneously. Prior to insertion, probe shanks were coated with lipophilic DiI' or DiD' (D282 or D7757, Thermo Fisher) to allow histological verification of recording sites. Probes were lowered with a manual micromanipulator until they penetrated the cortical surface, at which point the probes and the headframe were covered with 3% agarose (A9793, Sigma-Aldrich) to ground and stabilize the recording preparation. The probe was then slowly lowered at ~100 μm/minute until a final depth of 800-1200 μm was reached, at which point the probe was left to settle for at least 30 minutes before recordings began. Electrophysiological data were acquired at 20 kHz through the OpenEphys recording system connected to an Intan RHD2000 128-channel headstage (Siegle et al., 2017). Following the first recording session, probes and agarose were removed from the headframe and the craniotomies were covered with a silicone elastomer (Kwik-Cast, World Precision Instruments) until the next day.

In the subset of mice that were previously injected with AAV, a LED fiber was positioned over V1. Trials during which either a red LED (power ~ 8 mW) or blue LED (power ~0.8-1.5 mW) was turned on were randomly interleaved during half of the trials. For this study, only trials during which the light condition was off were used for analysis.

In vivo 2-photon calcium imaging

2PCI was performed on a custom microscope setup which includes a Sutter movable objective microscope (Sutter Instruments) with a resonant scanner (Cambridge Instruments). Data acquisition was controlled by a customized version of Scanbox (Neurolabware). GCaMP6s was excited by a Ti:sapphire laser (Chameleon Ultra II, Coherent) at 920 nm. Imaging was collected at 1-2 planes. For uniplanar experiments, continuous unidirectional scanning was done at 15.49 Hz. For biplanar experiments, an optotune lens was used to alternate between depths and a scanning rate of 7.745 Hz per plane. Planes were set ~20-30 um apart. An area of approximately 400x600 μm (some experiments 500x720 μm) was imaged using a 16x, 0.8 NA objective lens (Nikon Corporation) through the headframe filled with Immersol-W (Carl Zeiss Microscopy). Prior to imaging, mice were acclimated to the running wheel and visual stimulus setup over 3 days of training sessions. Running speed was recorded using a rotary encoder. During at least one of these training sessions, GCaMP6s expression was checked in AL, PM, and V1. If the imaging field of view (FOV) over the area of expression was obscured due to tissue growth or had poor expression of GCaMP6s, that region was not imaged. Imaging FOVs were identified by matching up the blood vessel patterns on the surface of the brain with images taken during ISI (Figure 1.1d). For each mouse, we imaged 1 FOV per session, per day. Most mice were imaged over 3 days, 1 day per region.

Visual stimulation

Visual stimuli were generated using custom MATLAB code and Psychtoolbox-3 and presented on a gamma corrected LCD monitor (electrophysiology, Acer S231HL, 24'' and 2PCI, Asus PG279Q, 27'', both 60 Hz refresh rate) positioned ~15-18 cm away from the mouse's right

eye. Prior to SF and TF tuning preferences characterization, receptive field locations were mapped by using flashed vertical and horizontal bars, or by manually moving a small drifting stimulus across the monitor until the location that elicited the most multi-unit activity for each probe shank and/or region was identified. The bar receptive field stimuli consisted of vertical or horizontal bars that were 20-21° wide that tiled the entire screen and flashed from black to white over 2 seconds with a TF = 1 Hz and a gray pre/post-stimulus screen and was repeated 10-12 times. For 2PCI experiments, responses to different bar locations were averaged across the entire FOV and the combination of vertical and horizontal bar positions that elicited the strongest response was set as the receptive field center. For electrophysiology experiments, average firing rates to each bar position from multi-unit spikes from 2-3 channels along each probe shank were used to determine the bar positions that corresponded to the receptive field location. For electrophysiology experiments, we additionally presented a sparse noise stimulus towards the end of each recording, where black or white squares 3-6° in size were flashed across the screen tiling a 50x50° area, repeated 12-15 times, and this stimulus was used to generate spike triggered average receptive fields for each sorted unit. The receptive fields for all the sorted units for each laminar shank were plotted and only shanks in which receptive fields were centered within 40° of the center of the visual stimulus were included.

To identify laminar borders in electrophysiology experiments, a full field flashed screen stimulus was presented for current source density analysis (CSD) at the beginning and end of each experiment. CSD signatures that identify laminar locations of recording contacts were found to differ between cortical areas. Details of results, and criteria used to assign layers are found below.

SF, TF, and speed tuning were measured using a series of drifting sine wave gratings that varied in 5-6 SFs (0.01-0.32 cycles per degree (cpd) in octave increments), 5 TFs (0.5-7.5 Hz in octave increments), and 2-4 directions (0, 90, 180, 270° or 90, 180°) and were presented in a 40° diameter circular aperture. Each stimulus was repeated 12-15 times. For 2PCI orientation tuning experiments, gratings varied across 8 directions (0-315° in 45° increments), and for AL and PM two SF/TFs combinations (SF/TF = 0.04 cpd/4 Hz and 0.16 cpd/1 Hz). For V1, orientation tuning was measured at SF = 0.04 cpd, and TF = 1 Hz. Each stimulus was repeated 15-20 times. For all experiments, stimulus conditions were presented randomly. For electrophysiology experiments, a 0.5 second gray screen preceded and followed each 1 second stimulus presentation. For 2PCI, a 2 second gray screen preceded and followed each 2 second stimulus presentation. For all drifting grating experiments, a stimulus that consisted of a gray screen "blank" was interleaved randomly in 10% of trials.

Histology

After all recording or imaging sessions were completed, animals were euthanized by intraperitoneal injection of euthasol (>100 mg/kg) and then perfused with phosphate-buffer saline (PBS), followed by 4% paraformaldehyde (PFA). Brains were removed from skulls and post-fixed in 2% PFA and 15% sucrose at 4C for 24 hours before being transferred to 30% sucrose at 4C for at least another 24 hours. Brains were sectioned coronally and DAPI stained. For 2PCI brains, immunohistochemistry was also performed to verify GCaMP6s viral expression by incubating sections with chicken anti-GFP (1:1000, GFP-1020, Aves Labs) at 4° overnight in 1% normal donkey serum/0.1% Triton-X 100 in PBS, followed by Alexa 488 (1:500, 703-545-

155, Jackson ImmunoResearch) secondary for 2 hours. Sections were imaged on an Olympus BX63 microscope using a 10x/0.4 NA objective (Olympus).

Spike sorting and electrophysiology data processing

Single unit spikes were extracted by automated template matching using Kilosort2 and sorted into "clusters" that were assigned as good/single unit, multi-unit, or bad (Pachitariu, Steinmetz, et al., 2016). Clusters and their labels were visually inspected using phy2 and reassigned based on spike wave-form shape, presence throughout the entire recording, and refractory period violations. Cluster quality was further assessed by measuring the fraction of refractory period violations and the "isolation distance" (Schmitzer-Torbert et al., 2005) of each unit. Only units with refractory period violations of <0.5% and isolation distance >=15 were included in subsequent grouped analysis. Refractory period violations were calculated by taking the number of spikes in the refractory period (1.5 ms) divided by total spikes. Fast spiking and regular spiking clusters were separated based on peak to trough (PtT) timing. When plotting all units, a clear separation at 0.6 ms could be seen between two peaks. Units with PtT < 0.6 ms were considered fast spiking and excluded from group analysis, while units with PtT >= 0.6 ms were classified as regular spiking. We only included regular spiking units for all analysis of tuning properties.

Current source density analysis and laminar assignment

We used a combination of current source density (CSD) and histology to estimate the borders between layers 2/3, layer 4, and layers 5/6 in the visual cortex (Figure 1.1b). CSDs were computed using CSDPlotter to calculate the second spatial derivative of the low-pass filtered

(<1000 Hz) local field potential during the flashed screen visual stimulus (Pettersen et al., 2006). For V1, the borders of layer 4 were identified as the 3-4 channels where an early sink was found. For AL and PM, the CSD maps exhibited a less consistent layer 4 sink, but nevertheless, other patterns in the order of current sinks and sources for AL and PM allowed us to reliably identify the layer borders in these regions in combination with the known thickness of each cortical layer and the spacing of the electrode contacts (Figure 1.2). In PM, layer 4 was typically assigned as the 2-3 channels that were below a superficial layer 2/3 sink and above a deeper layer 5 source (Figure 1.2c-d). In AL, layer 4 was harder to distinguish from the bottom of layer 2/3 due to a vertically large sink that often spanned both layer 2/3 and 4, but the bottommost 2-3 channels of this sink were typically set as layer 4 (Figure 1.2a-b).

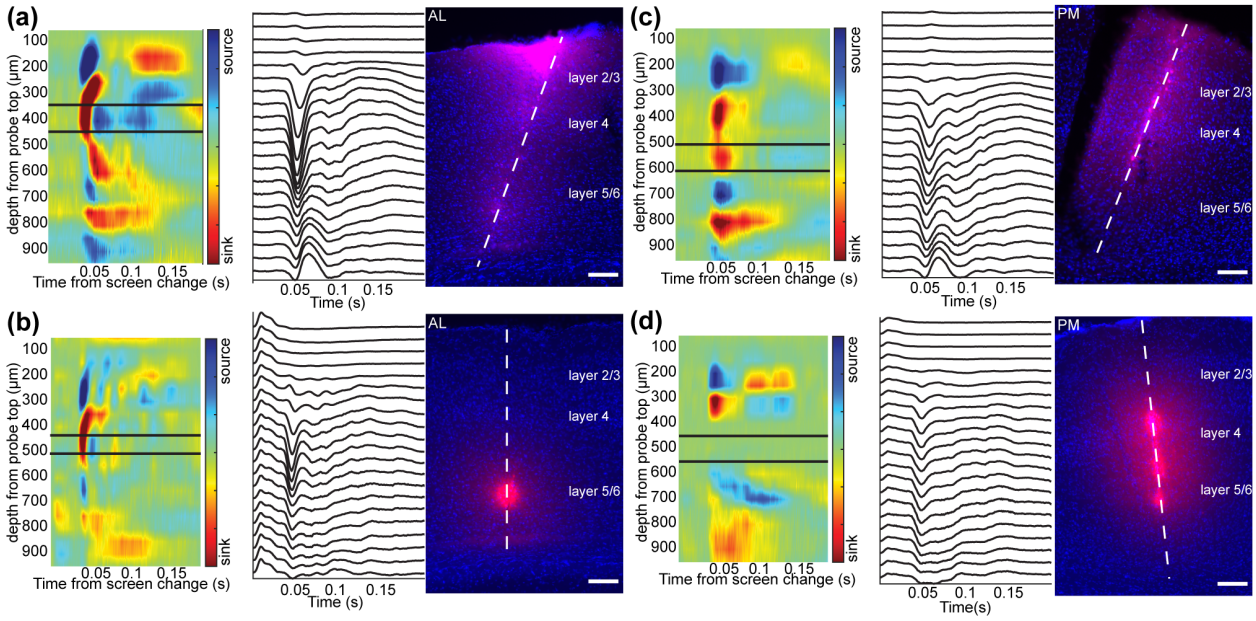

Figure 1.2: Sample current source density (CSD) plots and histology from AL and PM recording penetrations from 2 sample recordings. (a-b) Examples from recordings in AL of 2 different mice. (c-d) Examples from recordings in PM of 2 different mice. For each example, left: CSD with layer borders outlined, middle: LFPs from channels, right: histology reconstruction of probe penetration with DiI or DiD'. Granular layers (layer 4) were defined as the 2-3 channels (~100-150 μm) that lay below a superficial sink (corresponding to the bottom of layer 2/3) and above a deeper layer source and sink (corresponding to layer 5/6) (see Methods). Scale bar on histology images= 100 μm.

Unit classification

Units were included in grouped analysis based on several criteria. Units had to be well isolated (based on refractory period violations and isolation distance), and with receptive fields that overlapped with the part of the screen that the visual stimulus was presented on. Units that were on shanks that were not centered were removed and units that were not in the cortex based on CSDs were also removed. To determine which units were visually responsive, the firing rate for each unit per trial was calculated and averaged to get the mean firing rate for each stimulus presentation. A unit was considered visually responsive if the stimulus presentation that elicited the strongest response was significantly different from the response to "blank" trials (Wilcoxon Rank-Sum, $p<0.05$).

2-photon calcium imaging processing

Pre-processing was done using suite2p (Version 0.9.0), which included motion correction, cell body region-of-interests (ROI) detection, and neuropil estimation (Pachitariu, Stringer, et al., 2016). ROIs were visually inspected to include only cell bodies and cells that could be well visualized in a max-intensity projection image of the registered frames. The fluorescent trace for each ROI and its corresponding neuropil were then extracted for data analysis. To estimate the contribution of the neuropil to the cell body response, the fluorescent traces were corrected using $F_{ROI\_corrected} = F_{ROI}(t) - \alpha F_{neuropil}(t)$ (Kerlin et al., 2010). The correction factor, α, was estimated by taking the average ratio of the fluorescence in the blood vessels of the FOV divided by the neuropil.

ROI classification

For each ROI, the response to each trial was calculated by measuring the change in fluorescence from baseline, divided by baseline (dF/F). The baseline for each trial was taken as the mean fluorescence during the 2 second pre-stimulus period. ROIs that were not reliably responsive were eliminated based on 3 criteria. First, the mean fluorescence for the maximum trial condition had to be less than 6% of the maximum mean fluorescence for ROIs in the FOV. Second, these low fluorescence ROIs had to have a d-prime ($\delta = (\mu_{max} - \mu_{blank})/(\sigma_{max} + \sigma_{blank})$) value less than 0.5, where μ_{max} and σ_{max} are the mean and standard deviation of the response at the preferred stimulus, and μ_{blank} and σ_{blank} are the mean and standard deviation of the response at the blank stimulus (Marshel et al., 2011). Finally, some ROIs with extremely high dF/Fs due to division by a very small baseline were eliminated by removing any ROIs that had a trial dF/F that exceeded the median maximum trial dF/F per ROI + the 95% percentile maximum trial dF/F per ROI. ROIs were determined to be visually responsive for each experiment type (i.e. SF, TF experiments versus orientation tuning experiments) by one-way ANOVA with the blank condition included ($p<0.05$).

Quantification of tuning responses

All data analysis except for the Allen Brain Visual Coding datasets were analyzed in MATLAB R2018b. For Allen Visual Coding datasets, python 3.6.10 was used to extract summary data for each unit that was subsequently analyzed and plotted in MATLAB. For both electrophysiology and 2PCI experiments, averaged responses to each stimulus condition were calculated by averaging the firing rate or dF/F during the stimulus presentation window. Trials were separated into running versus stationary trials based on the amount of movement that was

recorded by the wheel encoder during each trial. For subsequent analysis, only stationary trials (< 0.5 cm/s running) were used to avoid any confounds that running may have on neuronal activity (Niell & Stryker, 2010). On average, approximately 70% of our trials were classified as stationary, and 10% of trials between 0.5-1 cm/s, and the remaining 20% of trials >1 cm/s running speeds.

Estimation of tuning curve properties

To estimate the SF, TF properties of all visually responsive neurons in our datasets, we estimated the preferred SF, TF of each neuron by finding the visual stimulus condition that resulted in the strongest average response. The SF and TF at this stimulus condition were taken to be the preferred SF and TF of this neuron. Tuning curves for SF and TF were then generated by taking the SFs at the preferred TF and the TFs at the preferred SF (Figure 1.3c and d). We also calculated the preferred TF/SF ratio by taking the preferred TF divided by the preferred SF. Orientation and direction selectivity indices (OSI and DSI) were calculated using the SF, TF combination that most optimally drove each neuron to respond. OSI and DSI were computed in the same manner as previous papers (Marshel et al., 2011). Trial responses below zero were rectified to zero prior to computing the OSI and DSI.

The Mahalanobis generalized distance was calculated using all cells in each group (i.e. region, layer, mouse line) to estimate the distance between SF, TF distributions of each group (Murakami et al., 2017; Salinas et al., 2021). First, SF and TF tuning data were Box-Cox transformed to normalize the data, then the Mahalanobis generalized distance was calculated as follows:

$$D^2(w1, w2) = \overline{d_{12}} V^{-1} \overline{d'_{12}}$$

where D^2 is the squared Mahalanobis distance, and $\overline{d_{12}}$ is the vector of the differences between the means of the SF and TF variables of the groups w1 and w2, and V is the pooled within-group dispersion matrix of the two groups (Legendre & Legendre, 1998). V is estimated as follows:

$$V = \frac{1}{n_1 + n_2 - 2}[(n_1 - 1)S_1 + (n_2 - 1)S_2]$$

where S_1 and S_2 are each group's dispersion matrices, and n_1 and n_2 are the number of cells in each group. Each dispersion matrix is computed by multiplying the matrix of centered data with its transpose and then dividing by n-1 (Legendre & Legendre, 1998).

2-D Gaussian fitting for speed tuning

Speed tuning was assessed by fitting the trial firing rate or dF/F of each SF and TF combination to a modified 2-dimensional Gaussian function, below using lsqcurvefit in MATLAB (Priebe et al., 2003).

$$R(sf, tf) = A * exp\left(-\frac{\left((sf) - (sf_0)\right)^2}{2\sigma_{sf}^2}\right) * exp\left(-\frac{\left((tf) - \left(tf_p(sf)\right)\right)^2}{2\sigma_{tf}^2}\right)$$

where $tf_p(sf) = \xi(sf - sf_0) + tf_0$

Here A = amplitude of max firing, sf_0 = preferred SF, tf_o = preferred TF, σ_{sf} = SF tuning width (in octaves), σ_{tf} = TF tuning width (in octaves). The $tf_p(sf)$ variable accounts for the dependence of TF tuning on SF, where ξ is the speed tuning index/slope. When $\xi = 1$, the neuron is perfectly speed tuned as SF and TF vary in proportion. When $\xi = 0$, the cell is considered not speed tuned, as SF and TF tuning occur independently, and the preferred speed depends on the SF and TF. For neurons with high directional selectivity (DSI>0.4), only SF and TF trials in the preferred direction are included. Similarly, for neurons with orientation selectivity (OSI>0.2), only SF and

TF trials at the preferred orientation were included. Trial responses below zero were rectified to zero prior to fitting. For neurons responsive to all directions, all SF and TF trials were included for model fitting. 95% confidence intervals (CI) were generated by sampling with replacement 500 times. Only neurons that could be well-fit by the 2-D Gaussian were included for subsequent analysis. This criterion required that the 95% CI be less than 3 octaves for the SF_0, TF_0, and σ_{SF}, σ_{TF} eliminating approximately 40 - 70% of ROIs and single-units that were not well-fit. Neurons were considered "speed tuned" if the 95% CI for the speed tuning slope included a slope of 1, but not 0. All other cells were classified as "not speed tuned." The median value from the fits was taken as each neuron's speed tuning index and preferred speed (tf_0/sf_0). Example fits from electrophysiology and 2PCI experiments are shown in Figure 1.3a and b.

Effect of fitting on inclusion

We found that many neurons and their responses were "poorly" fit by the speed tuning 2-D Gaussian despite being visually responsive. To investigate if selecting only well-fit neurons biased our population of neurons, we compared the d-prime of neurons that were well-fit by the 2-D Gaussian to the d-prime of neurons that were visually responsive but not well-fit (Figure 1.3e). The d-prime was calculated as described in Methods, ROI Classification. In both our electrophysiology and 2PCI datasets, we found that well-fit neurons exhibited more reliable responses compared to non-fitted neurons. Thus, while fitting to the 2-D Gaussian allowed us to estimate speed tuning from our data, it also resulted in a biased sampling of visually responsive neurons in our data set to only the most reliably responsive neurons. However, when comparing the tuning properties of neurons that were considered "well-fit" versus poorly fit, we did not see significant differences in their preferred SF, TF or TF/SF (data not shown). Because the

"robustness" of cell responses has been shown to influence the TF tuning properties of visual areas (Mesa et al., 2021), we decided to look at population SF, TF, TF/SF tuning preference across all visually responsive neurons, not just well-fit neurons. However, because fitting is necessary to estimate the speed-tuning slope, we analyzed speed tuning properties using only neurons well-fit by the 2-D Gaussian function.

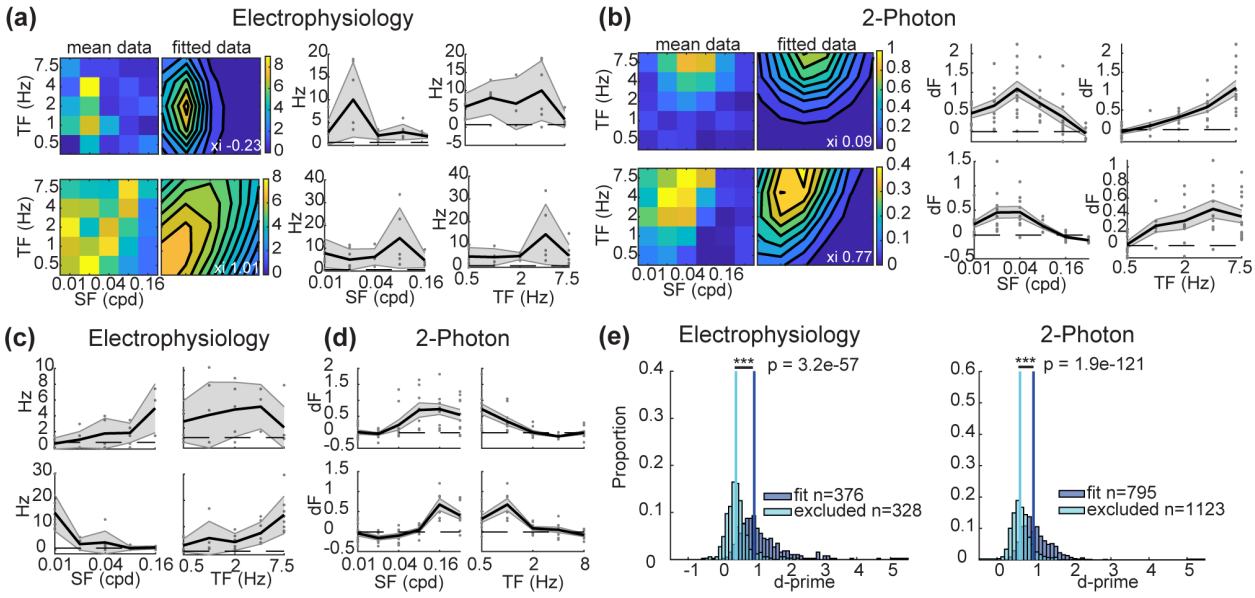

Figure 1.3: Sample 2-D Gaussian fits and non-fit SF, TF tuning curves from electrophysiology and 2PCI. (a) Examples of 2-D Gaussians (left) and non-fit SF, TF turning curves (right) from electrophysiology studies. Tuning curve plots are the mean response for each condition, with the standard error (sem) shaded gray, and individual trial firing rates as dots. Each row corresponds to a single unit example. (b) same as (a), but 2PCI examples. (c) Non-fit SF, TF tuning curves of two example units (each row), from visually responsive units that were considered poorly fit by the 2-D Gaussian. (d) same as (c) except for 2PCI examples. (e) Proportional histograms of d-prime values of neurons that were well-fit versus not well-fit (excluded) by the 2-D Gaussian. Neurons well-fit by 2-D Gaussian respond more reliably in both electrophysiology (left) and 2PCI (right) datasets. ***p<0.001 (Wilcoxon Rank-Sum test). Vertical line indicates the median of each distribution. Abbreviations: cpd = cycles per degree.

Analysis of Allen Institute Visual Coding Neuropixels dataset

To compare the TF tuning properties from our electrophysiology study to other electrophysiology studies of mouse visual cortex, we used the Allen Institute Visual Coding Neuropixels dataset (*Dataset: Allen Institute MindScope Program*, 2019; Siegle, Jia, et al., 2021)

to compare TF tuning properties in AL, PM and V1. The Neuropixels Visual Coding dataset was analyzed using Python 3 and MATLAB. First, all Brain Observatory sessions which contained experiments where TF tuning was measured from regions V1, AL, and PM were identified. For each probe per region, the units that corresponded to cortex were identified using a combination of the CSDs calculated from the Allen Institute, probe depth versus firing rate, and the region that was assigned by the Allen Institute analysis. We only included units that were significantly responsive to both the drifting and static grating experiments (Wilcoxon rank-sum, $p< 0.00125$ (0.05/40) for drifting gratings, and $p< 0.0004$ for static gratings (0.05/120), p-value Bonferroni corrected for multiple comparisons by dividing 0.05 by number of stimulus conditions). After selecting units that were visually responsive and located in the cortex, these units were exported to MATLAB. In MATLAB, units were further filtered based on spike quality metrics pre-computed by the Allen Institute so that only regular-spiking, well-isolated units were included (waveform duration >0.4, waveform peak to trough ratio <1, inter-spike-interval violations <=0.05, amplitude cut off <0.1, and presence ratio >0.9). Preferred TF measured from drifting grating experiments were then used to plot histograms of the preferred TF in each region.

To compare our dataset with the Allen Institute dataset, we subsampled our TF tuning preferences data by recalculating the preferred TF of each unit assuming we had only sampled TF at a SF = 0.04 cpd. This would allow us to match the SF, TF sampling of the Allen Institute TF tuning experiments, where TF tuning was measured at a single SF = 0.04 cpd. We re-calculated if a unit was visually responsive based on if we had only sampled at SF = 0.04 cpd and then calculated the preferred TF at the stimulus condition that drove the strongest responses.

Experimental design and statistical analysis

For most comparisons between groups of regions, layers, or cell classes we used the Kruskal-Wallis test followed by Dunn's post hoc test and Šidàk multiple comparisons. For two-way comparisons, we used the Wilcoxon Rank-Sum test. Statistical significance was typically set at $p<0.05$ unless otherwise specified. To account for potential by-animal effects, we additionally performed a hierarchical bootstrap statistical analysis (Saravanan et al., 2020). Briefly, we first resampled the experiments (or animals) in each group, then resampled the neurons from each experiment, and then averaged across all samples to generate a population of 1000 resampled means. The direct probabilities were then calculated to determine which group comparisons were significant ($p<0.025$). We considered findings to be significant where both the Kruskal-Wallis or Rank-Sum test and the hierarchical bootstraps were significant. For clarity, we list the Kruskal-Wallis or Rank-Sum p-values in our results, but all p-values from both methods can be found in Tables 1.1-1.5. Mahalanobis generalized distances were determined to be significant by transforming the squared Mahalanobis distance to a Hotelling's T2 statistic followed by an F Statistics (Legendre & Legendre, 1998). Distances were considered statistically significant if $p<0.016$ ($p<0.05/3$ with Bonferroni correction for multiple comparisons).

1.4 Results

We characterized the receptive fields of neurons in visual cortical areas V1, AL and PM of awake, stationary mice by measuring responses to drifting sine-wave gratings using both electrophysiology with laminar electrode arrays (Du et al., 2011) and 2PCI targeted to genetically accessed layer 5 excitatory neuron cell classes (Figure 1.1). For comparison to prior studies, electrophysiology experiments used visual stimulus sets focused on obtaining high-

resolution characterizations of SF, TF and their combinations (speed) (Andermann et al., 2011; Glickfeld et al., 2013). This required sampling of many combinations of SF and TF, precluding dense sampling of multiple directions/orientations to yield orientation or direction tuning curves. Because a prior study found differences in orientation and direction tuning for V1 L5ET versus L5IT neurons (E. J. Kim et al., 2015), an additional stimulus set was sampled to assess orientation and direction tuning for 2PCI of layer 5 ET or IT neurons. Although mice were free to run on a wheel, they were stationary on 70% of trials and only trials in which the mice were stationary were used for analysis (speeds <0.5 cm/s) (see Materials and Methods). A summary of the numbers of neurons and animals characterized by each method in each cortical area is shown in Supporting Table S1.1 and Supporting Table S1.2.

Electrophysiology of SF, TF, and TF/SF tuning preferences reveal diverse, but distinct tuning preferences across cortical areas and layers

To compare overall SF, TF and TF/SF (speed) tuning of neurons between V1, AL and PM, we first analyzed at the population level differences in tuning from all visually responsive neurons (see Materials and Methods for selection criteria) regardless of layers (Figure 1.4). While TF/SF can be considered a measure of speed preference, a speed tuned neuron does not prefer a single TF or SF, but instead a particular ratio (Movshon, 1975). Here we focus on the preferred TF/SF ratio separately from whether neurons are truly speed tuned. We will consider speed tuning, which measures how much a neuron prefers a conserved ratio of TF/SF across a range of SFs and TFs separately, with the results from our 2-D Gaussian fitting analysis (see Materials and Methods). Consistent with previous reports, we found significant differences in the preferred TF and TF/SF ratio of AL neurons compared to V1 and PM (Figure 1.4a-c, TF V1

p=1.05e-5, PM p=6.57e-7; TF/SF PM p=6.36e-6) (Andermann et al., 2011; Marshel et al., 2011). AL preferred higher TFs compared to V1 and PM, and faster TF/SF ratios compared to PM. However, in contrast to some previous studies, we did not find significant differences in preferred SF or differences between V1 and PM for TF, SF, or TF/SF.

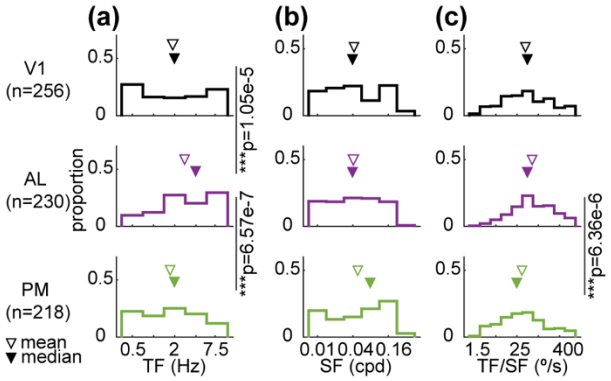

Figure 1.4: Area differences in TF, SF, and TF/SF tuning. (a)-(c) Histograms of preferred tuning preferences for V1, AL and PM (a-temporal frequency, b- spatial frequency, and c- TF/SF). For all plots, *p<0.05; **p<0.01; ***p<0.001 (Kruskal-Wallis followed by Dunn's post hoc test and Šidàk multiple comparisons). P-values listed for values < 0.05. Filled triangles correspond to the median, and open triangles correspond to the mean of each distribution. Abbreviations: cpd = cycles per degree, °/s = degrees per second.

Next, to determine if differences or lack of differences could be attributed to differences between laminar populations, we assigned neurons into 3 different groups based on CSD layer assignment (see Materials and Methods) – layer 2/3, layer 4, or layer 5/6, and plotted each layer and region's preferred SF, TF, and TF/SF ratio (Figure 1.5a-c). Layer 2/3 was undersampled due to a tendency for laminar electrodes to have poor single unit isolation in superficial layers of the mouse cortex (K. D. Harris et al., 2016). We generally found differences between regions, but not between layers. Between regions, no differences were found between V1 and PM for any layers. Between AL and PM, significant differences were found in layer 5/6 for preferred TF (Figure 1.5a p= 1.91e-4,), and in layer 4 for preferred SF and TF/SF ratio (Figure 1.5b p = 0.002, Figure 1.5c p= 4.66e-4). The direction of these differences was consistent with previous studies,

with AL preferring higher TFs and TF/SF ratios, but lower SFs. In superficial layers, low sample sizes may account for differences that did not reach statistical significance. However, consistent with previous studies, we found that superficial (layer 2/3) AL neurons preferred higher TFs compared to V1 (Figure 1.5a $p= 0.018$). When comparing across layers within regions, we largely did not find statistically significant differences in preferred SF, TF, or TF/SF, except for PM, where layer 4 neurons preferred higher SFs compared to layers 5/6 (Figure 1.5b $p=0.042$). When plotting the z-scored responses of all neurons by layer and region, neurons in layer 2/3 and layer 4 appear to be more specialized/biased in their responses to specific SF, TF combinations compared to layer 5/6, where the mean z-scored responses appear to be "flatter" suggesting less tuning or more varied tuning preferences (Figure 1.5d).

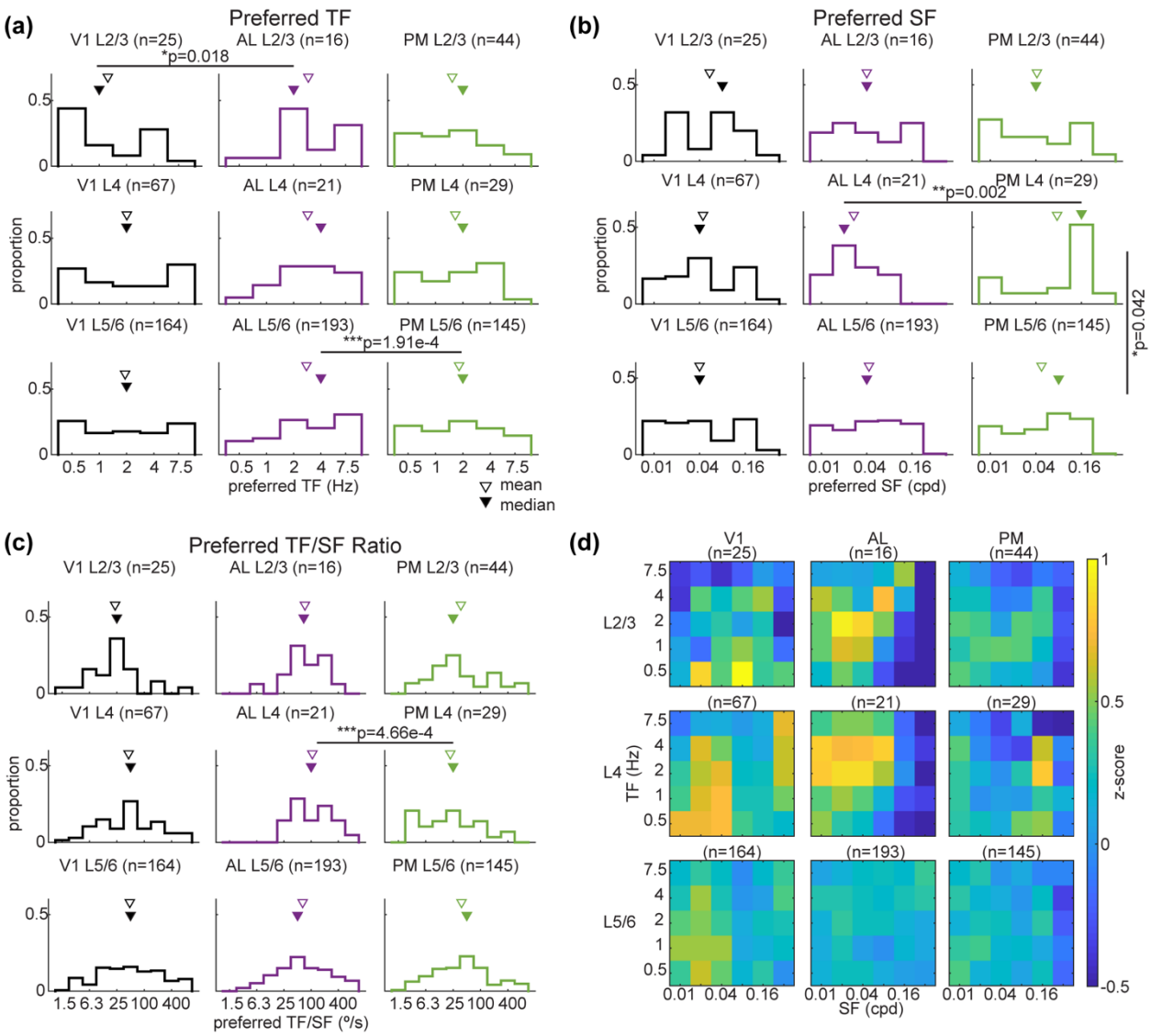

Figure 1.5: Spatiotemporal frequency tuning preferences across visual areas and layers. (a)-(c) Histograms of tuning preferences (a- spatial frequency, b- temporal frequency, c- TF/SF ratio). Each column corresponds to a visual area (V1, AL, PM), and each row corresponds to a layer (layer 2/3, layer 4, layer 5/6). *p<0.05; **p<0.01; ***p<0.001 (Kruskal-Wallis followed by Dunn's post hoc test and Šidàk multiple comparisons). Comparisons were considered significant and their p-values listed if p<0.05. Filled triangles correspond to the median, and open triangles correspond to the mean of each distribution. (d) z-scored mean responses to sampled SF and TF combinations at each neuron's preferred direction. Abbreviations: cpd = cycles per degree, °/s = degrees per second.

Because the preferred SF can depend on the TF of the grating presented, and vice-versa, we also performed multivariate statistical analysis to determine how areas and layers differ in their preferred SF and TF. We calculated the Mahalanobis generalized distances (Legendre &

Legendre, 1998; Murakami et al., 2017; Salinas et al., 2021) between neurons and their preferred SF, TF based on their layer and region assignment (Figure 1.6). Neurons in superficial layers seemed to prefer fewer unique SF, TF combinations whereas in deeper layers, a broader distribution could be found (Figure 1.6a). We found there to be significant differences in the Mahalanobis generalized distance between regions across multiple layers (Figure 1.6b). These significant differences were largely consistent with our analysis of SF or TF tuning separately, with significant differences found between AL-PM in deep layers (p=4e-4) , and in layer 4 (p=0.002). Multivariate analysis also revealed differences in deeper layers between AL-V1 (p=4e-4) and in superficial layers between AL-V1, though this was not statistically significant after correction for multiple comparisons (p = 0.02). Interestingly, the magnitude of the Mahalanobis distance in superficial layers was greater than in deeper layers, suggesting greater functional specialization or less varied tuning preferences in superficial layers (Figure 1.6b, upper right triangles of comparisons). However, these distances did not reach significance, potentially due to low sampling in superficial layers. Additionally, when looking at the Mahalanobis distances between layers in different regions, we did not detect any significant differences across layers (Figure 1.6c). Overall we found few differences in SF, TF tuning between V1, AL, and PM in our electrophysiology dataset biased towards deep layer neurons. Where differences between regions were significant, they were in directions consistent with previous studies. Neurons from the same visual area largely did not significantly differ in their preferred tuning preferences across layers.

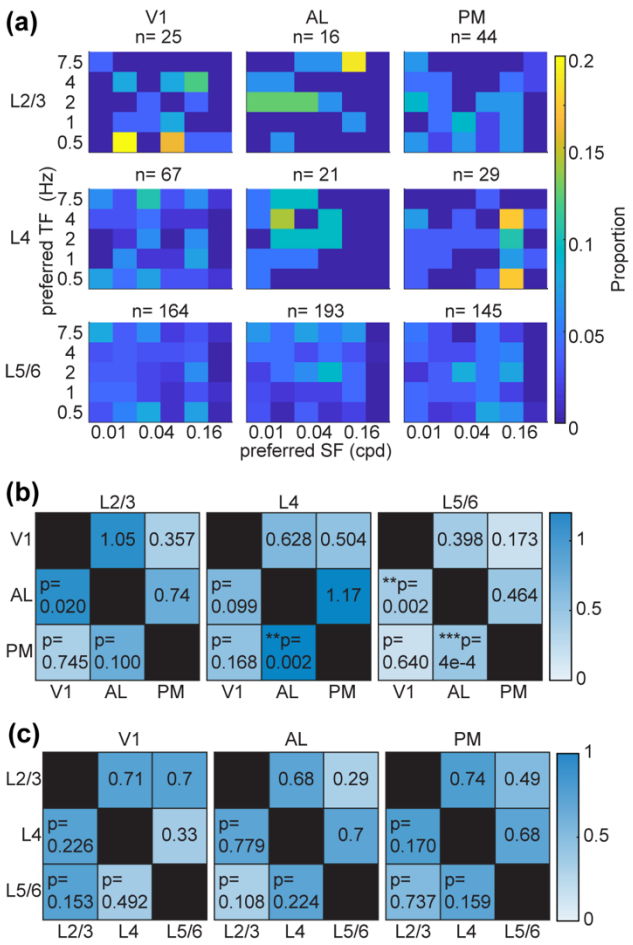

Figure 1.6: Multivariate analysis of spatiotemporal frequency tuning across areas and layers. (a) 2-D histogram of preferred SF and TFs across layers and areas. (b) Mahalanobis generalized distances between visual areas by layer assignment. Upper triangle numbers indicate distances. Lower triangle stars and numbers indicate p-values. *p<0.016, **p<0.01, and ***p<0.001 (F-statistic with Bonferroni correction for multiple comparisons (p<0.05/3)). (c) Same as (b), but the Mahalanobis generalized distance between layers by visual areas. Abbreviations: cpd = cycles per degree.

Estimation of speed tuning by 2-D Gaussian fitting reveals few speed tuned neurons

Neurons that are speed tuned do not prefer a single SF or TF, but instead prefer a ratio of TF/SF (speed) across different SFs and TFs. When plotted in log2 scale, this results in a "ridge" of preferred responses that falls along a line with a slope approximately equal to 1 (Priebe et al., 2003, 2006). Thus, neurons that are speed tuned are more likely to have a speed tuning slope near 1, whereas neurons that are not speed tuned will not. Previous studies in mice have found

few speed tuned neurons in V1, but more speed tuned neurons in higher visual area PM (Andermann et al., 2011; Ledue et al., 2012; Salinas et al., 2021). To estimate speed tuning and preferred speed of speed tuned neurons we fitted the responses of each neuron to different SFs and TFs to a modified 2-D Gaussian (Figure 1.7a,b) (see Materials and Methods). We found AL to be significantly more speed tuned compared to V1 and PM (Figure 1.7a, V1 p =1.07e-5 and PM p= 0.008) and AL to have a higher proportion of speed tuned neurons (Figure 1.7c).

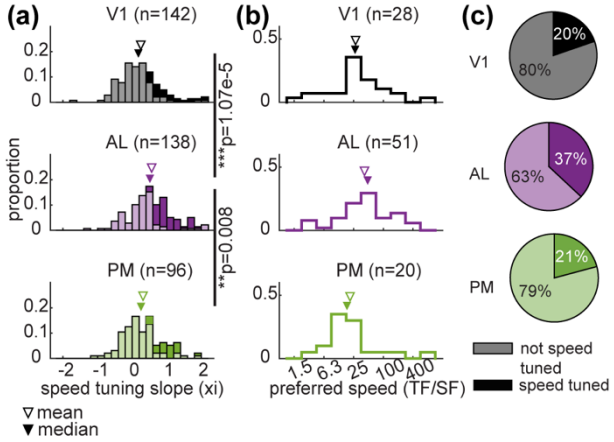

Figure 1.7: Speed tuning of V1, AL, and PM neurons. (a) Histograms of speed tuning slopes for neurons significantly speed tuned versus not speed tuned. Lighter color corresponds to non-speed tuned neurons, and darker color corresponds to speed tuned neurons. Statistical comparisons are for differences in the distribution of speed tuning slopes. (b) Preferred speed of speed tuned neurons. For both (a) and (b), *p<0.05; **p<0.01; ***p<0.001 (Kruskal-Wallis followed by Dunn's post hoc test and Šidàk multiple comparisons). P-values are listed for values <0.05. Filled triangles correspond to the median, and open triangles correspond to the mean of each distribution. (c) Proportion of neurons across all layers that were speed tuned versus not speed tuned.

Range of visual stimulus sampling space can shift area tuning preferences

Recently, the Allen Brain Observatory published a large extracellular electrophysiology data set which includes tuning responses to visual stimuli for neurons across several mouse cortical and subcortical visual areas (*Dataset: Allen Institute MindScope Program*, 2019; Siegle, Jia, et al., 2021). While SF and TF tuning preferences were also examined in this study, their stimulus set differed from ours in that more directions were sampled (8 versus 2-4), SF tuning

was measured using whole field static gratings, and TF tuning preferences were measured at a single SF (SF = 0.04 cpd). Because the preferred TF can depend on the SF of the grating and vice-versa (Priebe et al., 2006), we compared the distribution of preferred TF that we found in our study to the preferred TF found in the Allen Visual Coding dataset. We found that when we subsampled our TF tuning data to match the Allen TF tuning stimulus set and only include trials with SF= 0.04 cpd, the preferred TF shifted towards lower TFs (Figure 1.8a-b) and closer to the distribution of preferred tuning from the Visual Coding dataset (Figure 1.8c p = 0.044). No significant differences between our TF tuning distributions or our subsampled TF tuning distributions were found compared to the Visual Coding TF tuning distributions.

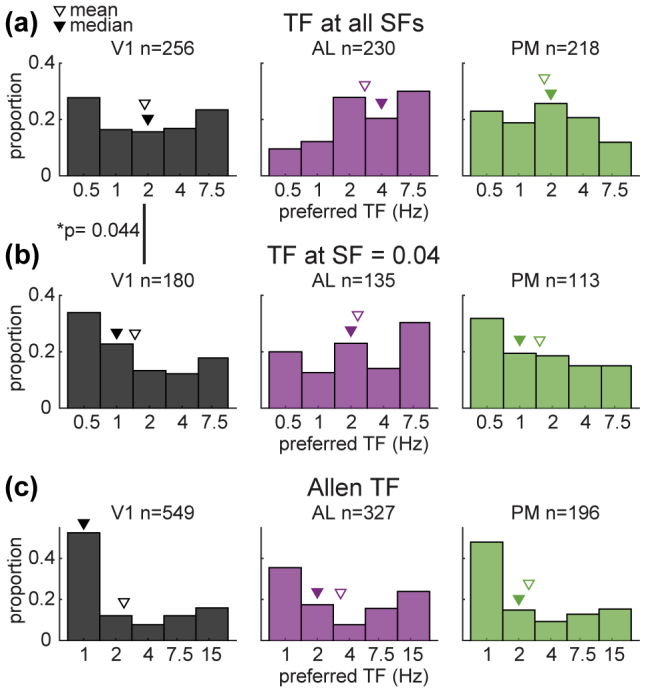

Figure 1.8: Effect of spatial frequency sampling on preferred temporal frequency tuning. (a)-(c) Preferred TF for V1, AL, and PM, where (a) the preferred TF is taken from all visually responsive neurons sampled at the preferred SF. (b) Preferred TF taken from all visually responsive neurons sampled with SF = 0.04 cpd only. (c) Preferred TF from visually responsive units from Allen Visual Coding, temporal frequency tuning experiments. (In those experiments only SF=0.04 was sampled). Note that our TF sampling range differed by one octave compared to the Allen Visual Coding dataset. *p<0.05; **p<0.01; ***p<0.001 (Kruskal-Wallis followed by Dunn's post hoc test and Šidàk multiple comparisons). Statistical comparisons were done after rebinning both data sets to have matching TF sampling ranges (1-7.5 Hz). Filled triangles correspond to the median, and open triangles correspond to the mean of each distribution.

2PCI of two layer 5 neuronal classes reveals area and cell-class differences in SF, TF tuning preferences

Because there are multiple excitatory cell types in different cortical layers that cannot be distinguished by extracellular electrophysiology, we also used transgenic mouse lines with 2PCI to selectively characterize different, identified cell classes in layer 5. We used two mouse lines that label either ET (Npr3-Cre-NEO-IRES) or IT (Tlx3-Cre) projecting layer 5 excitatory neurons (Daigle et al., 2018; Gerfen et al., 2013). The selectivity of these mouse lines for labeling layer 5 ET or IT neurons has been well characterized by previous studies from our lab (E. J. Kim et al., 2015; Kirchgessner et al., 2021). Although we did not note differences in tuning preferences between L5ET versus L5IT neurons in any areas for SF, TF or TF/SF, differences between areas were present for each cell class. Between regions, we found that both L5IT and L5ET neurons were tuned differently for SF and TF/SF. These differences were primarily between AL-PM (Figure 1.9a, SF L5IT p= 2.04e-4, and L5ET p=0.002; TF/SF L5ET p= 6.70e-5) and AL-V1 (Figure 1.9a, SF L5IT p=5.83e-4 and L5ET p=7.89e-6; TF/SF L5IT p=5.53e-13, and L5ET p=1.98e-7). In agreement with past studies, AL neurons preferred lower SFs, and faster TF/SF ratios compared to V1 and PM (Figure 1.9a). While L5IT neurons in AL preferred higher TFs compared to V1 and PM (Figure 1.9a, AL-V1 p=1.23e-10 and AL-PM p= 0.001), no differences in TF preferences were found for L5ET neurons. We also did not find significant differences in tuning between V1-PM for either cell class. While we did not observe any statistically significant differences in SF, TF tuning between the layer 5 cell classes, there was a trend in V1 for L5ET neurons to prefer higher TFs and lower SFs than L5IT neurons (TF p = 0.035, SF p=0.013, Table 1.5).

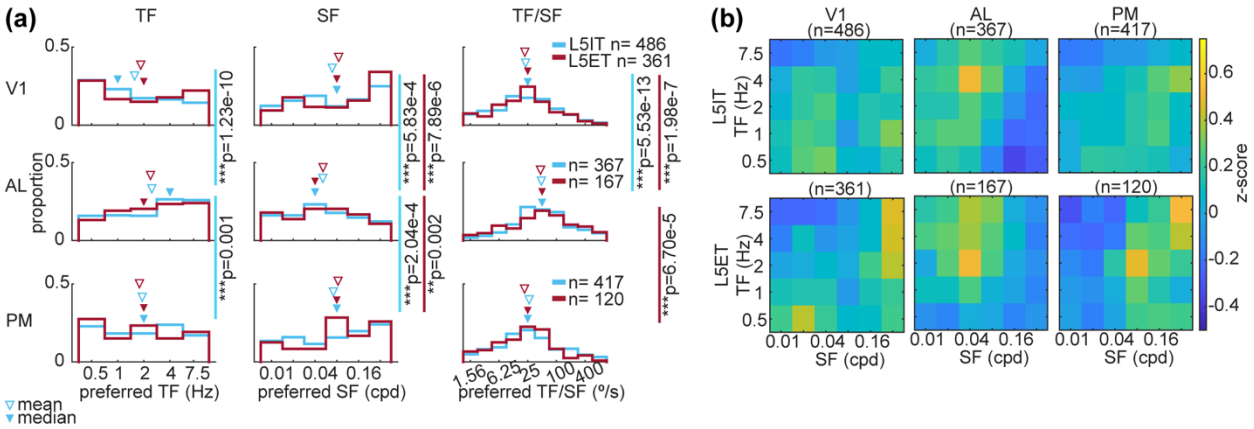

Figure 1.9: Differences in spatiotemporal frequency tuning preferences between L5ET and L5IT populations and across V1, AL and PM. (a) L5IT (Tlx3) versus L5ET (Npr3) SF, TF, and TF/SF histograms (left to right). *p<0.05; **p<0.01; ***p<0.001 (for across area comparisons-Kruskal-Wallis followed by Dunn's post hoc test and Šidàk multiple comparisons, for between mouse line comparisons-Wilcoxon Rank-Sum test). P-values listed for values < 0.05. Filled triangles correspond to the median, and open triangles correspond to the mean of each distribution. (b) Averaged z-scored responses of responsive neurons in V1, AL, and PM to SFs and TFs sampled at each neuron's preferred direction. Top row corresponds to L5IT, bottom row corresponds to L5ET. Abbreviations: cpd = cycles per degree, °/s = degrees per second.

When plotting the average z-scored responses (Figure 1.9b) and distribution of preferred SF and TF together in 2-D histograms (Figure 1.10a), we found that for L5IT and L5ET neurons, there was a wide range of combinations of SFs and TFs that neurons could prefer, similar to our histograms from electrophysiology recordings of deep layer neurons (Figure 1.6a). However, certain combinations were more strongly preferred in different regions and mouse lines, so we again calculated the Mahalanobis generalized distances between cells for each region and mouse's distributions. We found differences largely consistent with our analysis of SF, TF, and TF/SF alone, with differences found between V1-AL (L5IT p=7.9e-14 and L5ET p=3.7e-7) and AL-PM (L5IT p= 5.6e-7 and L5ET p=2.4e-4) for both L5IT and L5ET neurons (Figure 1.10b).

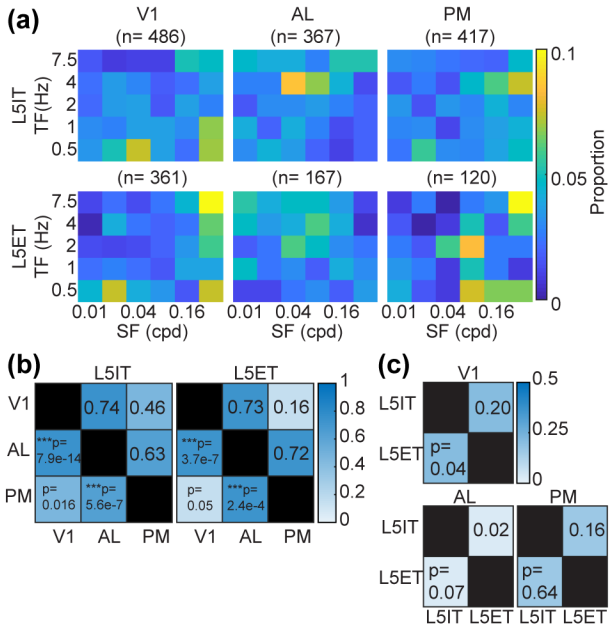

Figure 1.10: Multivariate analysis of SF, TF responses. (a) 2D histogram of preferred SFs and TFs for each mouse line and region. (b) Mahalanobis generalized distances between regions per mouse line. Upper triangle numbers indicate distances. Lower triangle stars and numbers p-values. *p<0.016, **p<0.01, and ***p<0.001 (F-statistic with Bonferroni correction for multiple comparisons (p<0.05/3)). (c) Same as (b) but the Mahalanobis generalized distances between each mouse line per region. Abbreviations: cpd = cycles per degree.

Layer 5 neurons are more speed tuned in higher visual areas, but speed tuning does not differ between layer 5 cell classes

We also used our fitted data set to compare speed tuning index and preferred speed of speed tuned neurons across AL, PM, and V1 and between L5IT and L5ET neurons. Between regions, we found that both IT and ET neurons in PM were more speed tuned compared to V1 (Figure 1.11a, L5IT p = 1.91e-4; L5ET p = 4.74e-6). PM L5ET neurons were also more speed tuned than their counterparts in AL (Figure 1.11a, p=0.017). Between L5IT and L5ET neurons, PM L5ET neurons were more speed tuned compared to PM L5IT neurons (Figure 1.11a, p= 0.004). Preferred speed did not differ between cell classes and only differed across regions for IT neurons, with AL speed tuned neurons preferring faster speeds compared to V1 and PM (Figure

1.11b, V1 p= 0.002 and PM p = 2.96e-4). The proportion of neurons that were classified as speed tuned was similar between ET and IT neurons, but differed across areas, with AL and PM both having a higher proportion of speed tuned neurons compared to V1 (Figure 1.11c). Taken together, higher visual areas tended to be more speed tuned compared to V1. L5ET PM neurons were especially speed tuned compared to other L5ET neurons in AL, as well as compared to L5IT neurons in PM.

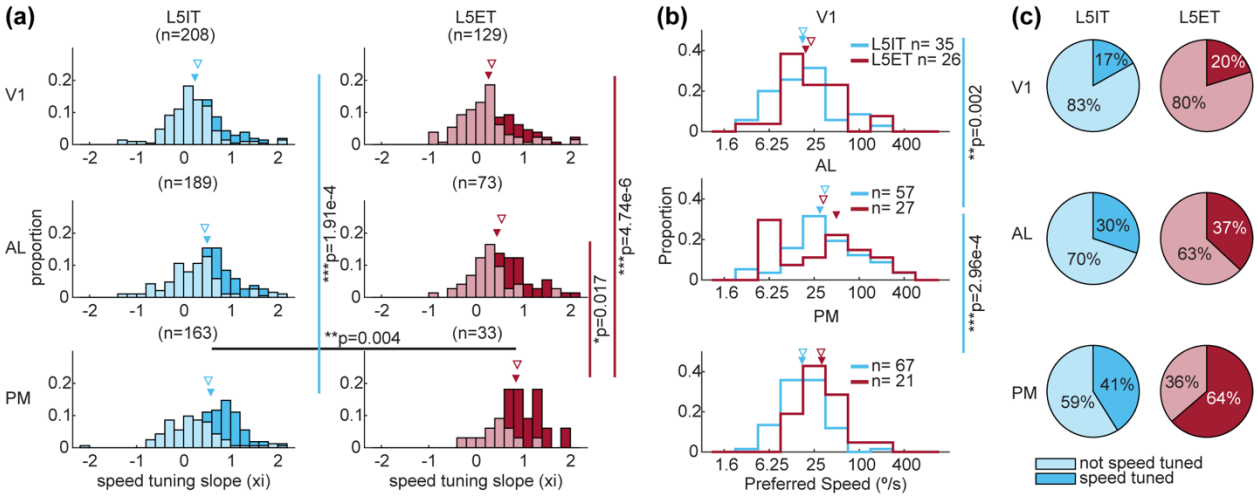

Figure 1.11: Speed tuning properties of layer 5 ET versus IT cell classes across V1, AL and PM. (a) Speed tuning slope distribution across regions and layer 5 cell classes. (b) Preferred speed distribution across regions and layer 5 cell classes. For both (a) and (b), *p<0.05; **p<0.01; ***p<0.001 (for across area comparisons-Kruskal-Wallis followed by Dunn's post hoc test and Šidàk multiple comparisons, for between mouse line comparisons- Wilcoxon Rank-Sum test). P-values listed for values <0.05. Filled triangles correspond to the median, and open triangles correspond to the mean of each distribution. (c) Proportion of neurons that were speed tuned versus not speed tuned across areas for each mouse line.

Layer 5 cell classes differ in their direction selectivity in V1, AL, and PM

We also compared orientation and direction tuning between L5IT and L5ET cells since previous studies found differences in orientation and direction selectivity between different layer 5 cell classes in V1 (E. J. Kim et al., 2015). Because it would not have been possible to reasonably sample the full SF, TF, and direction space all at once, we measured direction and orientation tuning with a separate set of gratings that drifted in 8 directions at either 1 or 2

different SF and TF combinations (Figure 1.12a). We found that most differences were between cell classes and their direction selectivity. L5ET neurons were more direction selective than L5IT neurons not only in V1, but also in higher visual areas AL and PM (Figure 1.12b, V1 p = 4.77e-6, AL p = 9.90e-5, and PM p = 4.25e-6).

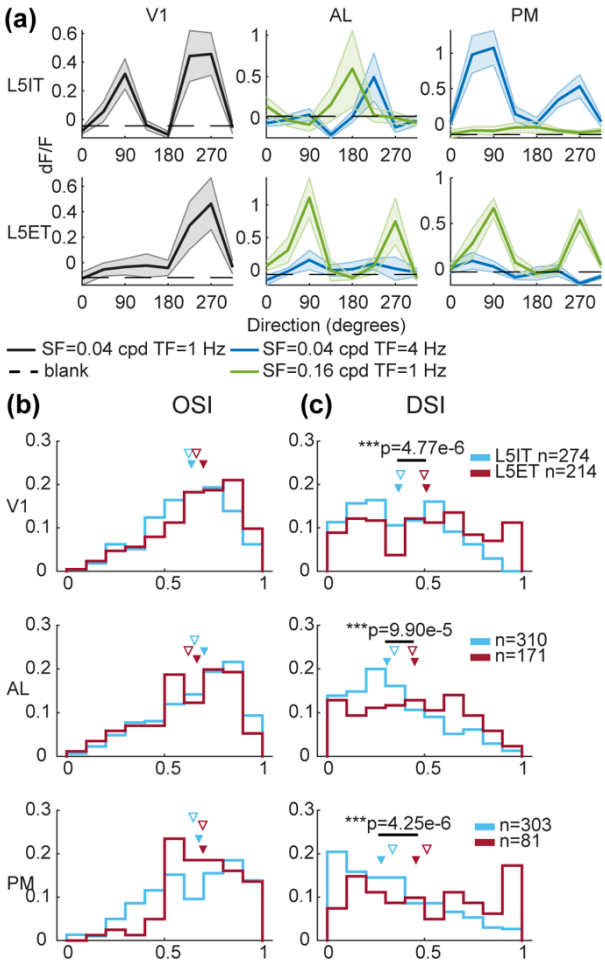

Figure 1.12: Orientation and direction selectivity differences between regions and layer 5 cell types. (a) Sample direction tuning curves from V1, AL, and PM for L5IT and L5ET neurons (top and bottom). For AL and PM, different colored tuning curves correspond to two different SF, TF combinations presented. Thicker line corresponds to mean response at each direction, and shading corresponds to the standard error (sem). (b) Orientation selectivity index (OSI) and (c) Direction selectivity index (DSI). *p<0.05; **p<0.01; ***p<0.001 (for across area comparisons- Kruskal-Wallis followed by Dunn's post hoc test and Šidàk multiple comparisons, for between mouse line comparisons- Wilcoxon Rank-Sum test). P-values listed for values <0.05. Filled triangles correspond to the median, and open triangles correspond to the mean of each distribution.

1.5 Discussion

We used two common methods for recording neural activity, extracellular electrophysiology and 2PCI to create an extensive dataset examining the specialization of V1, AL, and PM in the mouse visual system to SF and TF tuning. In contrast to previous studies, we used laminar probes and imaging to focus our attention to deeper layer cortical neurons, whose tuning have not been as well characterized as superficial cortical neurons in the past. We found that deep versus superficial neurons are largely specialized in similar ways in different cortical areas, consistent with past studies that have focused on superficial layers. We were surprised, however, at the variety of overlapping tuning preferences for SF and TF that we found in our experiments comparing AL and PM. Additionally, we characterized the orientation and direction tuning properties of layer 5 ET and IT projecting neurons in AL and PM and revealed differences between layer 5 ET and IT neurons in these higher visual areas for these visual features.

Functional specialization of mouse higher visual areas

Since early studies characterizing the visual response properties of mouse V1 and HVAs (Andermann et al., 2011; Marshel et al., 2011), AL and PM have often been studied as opposing areas with “fast” versus “slow” visual stimuli preferences. These differences in tuning have been used to understand how specialization may emerge from targeted V1 projections versus other sources, such as de-novo computations or non-V1 inputs (Blot et al., 2021; Glickfeld et al., 2013; E. J. Kim et al., 2020). In agreement with these functional biases, it has been demonstrated that AL versus PM projecting V1 neurons rarely connect with each other in V1, differ in gene expression, and usually project to one or the other and rarely to both areas (E. J. Kim et al., 2020; M. H. Kim et al., 2018). However, the results from our study suggest that, while biases in AL

and PM tuning exist for different SFs and TFs, there is also extensive overlap in range of SFs and TFs that neurons in these areas prefer, suggesting less functional specialization than previous studies (Figure 1.5, Figure 1.9).

The exact role each HVA plays in processing visual information remains to be elucidated, and likely is not as simple as a segregation of fast versus slow moving stimuli or tasks. Recent studies have demonstrated different roles for some of these areas in visually guided behavioral tasks (Jin & Glickfeld, 2020). Yet, these differences have not always come down to simply differences in visual perception. In Jin and Glickfeld 2020, PM was found to affect false alarm rates during a contrast change detection task and speed increment detection task, but suppression of PM did not affect sensory perception itself (Jin & Glickfeld, 2020). Additional types of visual stimuli or visually guided tasks may be necessary to tease apart how HVAs and their responses relate to their role in mouse visual processing.

Speed tuning in primates is thought to emerge either in V1 or MT (Priebe et al., 2003, 2006). To create speed tuning, spatiotemporal energy models propose that speed tuned units combine inputs from non-speed tuned neurons that prefer different SFs, and TFs, but have the same TF/SF ratio, or speed (Adelson & Bergen, 1985). In mice, few neurons were speed tuned, but we found that HVAs were more speed tuned than V1. In contrast with previous mouse studies finding more speed tuning only in PM (Andermann et al., 2011), we found that AL was also more speed tuned compared to V1 (Andermann et al., 2011). This difference might be due to preferential sampling of superficial layers (Andermann et al., 2011) versus deep layers (our study). But the difference is unlikely to arise from differential sampling using electrophysiology versus 2PCI since we found AL to be more speed tuned with both methods.

Unlike past studies, our study was biased towards sampling deeper layer cortical neurons in awake mice using stationary trials. While decreased sampling of superficial layers made it difficult to draw statistically significant conclusions, we noticed a trend where superficial units seemed more specialized for distinct SF and TF combinations compared to the deeper layers (Figure 1.6a). Thus, some of the overlap we found between AL and PM tuning preferences for SF and TF may be due to differences in layer 2/3 versus layer 5/6 cells. Layer 2/3 and layer 5/6 neurons play distinct roles in the canonical cortical microcircuit, and thus may differ in their visual responses based on their specific feedforward or feedback roles. Some HVAs receive more V1 input from superficial layer neurons, whereas others receive more input from deeper layer inputs (E. J. Kim et al., 2020; M. H. Kim et al., 2018). While neurons across cortical depths project to both superficial and deep layers of their cortical targets, different laminar cell types can differ in the laminar pattern of their corticocortical projections (J. A. Harris et al., 2019). In addition to different roles in cortico-cortical circuits, some layer 5/6 cell types project extratelencephalically and may play different subcortical roles in visual circuits.

While rodent V1 is traditionally thought to have a “salt and pepper” map of visual tuning preferences (Ohki et al., 2005), studies have suggested that there is a fine-scale modular organization in V1 for some cell types and tuning properties (D’Souza et al., 2019; Ji et al., 2015; Maruoka et al., 2017). In particular, it has been demonstrated in V1 that regions of layer 2/3 that prefer high SFs and low TFs are aligned with “patches” that receive strong cortical feedback and geniculocortical inputs in layer 1 (Ji et al., 2015). In contrast, cells in “interpatches” preferred low SFs, high TFs (Ji et al., 2015). Thus, in addition to cell class and areal differences in SF, TF tuning, there may be within-area tuning differences in sub-domains that are specialized for processing different streams of visual information. It would be interesting

in future functional studies to determine if a similar modular pattern for SF, TF tuning is present in other visual areas, and if such an organization is related to specific cell classes.

Stimulus sampling and tuning differences

The extent to which different studies have found differences between V1, AL and PM have varied. While our study primarily differed from previous studies in sampling methodology (extracellular electrophysiology) and depth (deep layer neurons), differences in the behavioral state of the mice between studies may also account for some of the differences observed. For example, in some studies mice were anesthetized with different agents (Marshel et al., 2011 - isofluorane; Roth et al., 2012 -urethane), while others used awake mice and incorporated both running and stationary trials in their calculations of tuning curves (Andermann et al., 2011). More recently, a study has demonstrated that the selection criteria used to include neurons as "responsive" or not, can also impact the population tuning preferences (Mesa et al., 2021). Differences in visual stimuli, such as whole field versus presentation within a defined aperture, and range of SF, TF sampled may also impact the calculated tuning preferences. This may be especially important for speed tuned neurons where the preferred SF and TF vary depending on each other. In this study, we found that if we subsampled our data to a limited range of SFs, the measured preferred TF shifted to lower TF preferences. Thus, sampling at a non-preferred SF or TF may impact the tuning preferences found in each study.

2PCI versus extracellular electrophysiology

2PCI and extracellular electrophysiology using laminar probes are both powerful tools for recording activity from large ensembles of neurons. However, inherent limitations with each

technique can limit or bias the types of neurons recorded (Siegle, Ledochowitsch, et al., 2021). While laminar electrophysiological probes in theory allow for unbiased sampling across all cortical depths, we found that superficial single units were often more difficult to isolate and resulted in fewer single-units being sampled. A similar dataset from the Allen Visual Coding dataset using Neuropixel probes also has far fewer superficial cortical units compared to deeper units (Siegle, Ledochowitsch, et al., 2021). Superficial units may be more difficult to sample and isolate with extracellular electrophysiology due to their lower firing rates compared to deep-layer cells (K. D. Harris et al., 2016). Despite differences in recording technique and cell types sampled, we found that AL consistently differed from V1 and PM, but V1 and PM did not significantly differ for most tuning properties. However, we did find that, while TF differences were the main driver of differences between AL and other regions in our electrophysiology dataset, the 2PCI data set was more separated by SF differences. While both datasets were biased to deep layers, our electrophysiology data set includes all regular-spiking (putative excitatory) neurons and grouped layer 5 and 6 neurons together as "deep layer" neurons since CSD landmarks cannot reliably separate layers 5 and 6 in HVAs. Since we were unable to exactly match our deep layer electrophysiology and 2PCI populations, the difference in tuning preferences may reflect differences in the deep layer neurons that were sampled with each method.

Layer 5 ET versus IT populations

In this study, we extended upon previous work examining visual tuning differences between L5ET and L5IT neurons in V1 by also finding differences between L5ET and L5IT populations in HVAs. We find that like superficial neurons, L5ET and L5IT neurons both exhibit

functional specializations in AL and PM, with biases towards high versus low TF/SF ratios respectively (Figure 1.9). However, in contrast with previous papers that recorded superficial V1 and PM neurons and found PM neurons to prefer slower, or similar TFs to V1 and slower TF/SF ratios (Andermann et al., 2011; Roth et al., 2012), we did not observe any significant differences in SF, TF tuning between V1 and PM. This may be potentially attributed to different selection criteria (Mesa et al., 2021), or layer 5 versus layer 2/3 differences.

Overall, we did not find many differences in SF, TF tuning between L5ET versus L5IT neurons. A previous study in V1 found L5ET neurons preferred higher TFs than L5IT neurons (E. J. Kim et al., 2015). In our study, we saw a similar trend, but it did not reach statistical significance. However, this could potentially be due to differences in mouse lines used to measure L5IT neurons (Glt25d2-Cre versus Npr3-Cre-NEO) or behavioral state (movement restricted versus freely running on wheel). Expression is much sparser in the Glt25d2-Cre mouse line than Npr3-Cre-NEO. We also characterized speed tuning properties of L5ET and IT neurons and found that PM L5ET neurons were not only more speed tuned than L5ET neurons in other regions, but also more speed tuned compared to their L5IT counterparts. A past study characterizing layer 5 neurons in V1 also noted more direction selectivity in V1 L5ET neurons than V1 L5IT neurons, and we were intrigued to see that this difference persists in HVAs (E. J. Kim et al., 2015).

While we did not find differences in SF, TF or orientation tuning between L5ET and L5IT neurons, there may be additional cell types that we did not discriminate between. For example, feedback IT neurons may be more specialized in HVAs compared to non-feedback IT neurons (Huh et al., 2018). Additionally, L5ET neurons project to several target regions, including superior colliculus, thalamus, striatum, and pons, and a single ET neuron may project

to more than one of these targets (Kirchgessner et al., 2021; Zhang et al., 2021). In V1, corticotectal and corticostriatal neurons have been demonstrated to exhibit differences in contrast sensitivity and tuning selectivity for orientation and SF (Lur et al., 2016). V1 ET neurons that project to striatum versus pons have also been demonstrated to play different roles in an eyeblink conditioning task (Tang & Higley, 2020). However, corticostriatal neurons consist of both ET and IT neurons, so differences in these studies between corticostriatal versus other projection targets may also be related to ET versus IT differences (Baker et al., 2018).

Overall, we have conducted an extensive overview of SF, TF, orientation and direction tuning properties of mouse deep layer visual cortical neurons that adds valuable data to the rich literature that currently exists for superficial mouse visual cortical neurons. While our data show many consistencies across superficial and deep layers, we also revealed key cell class differences between different projection populations in higher visual areas, particularly for direction selectivity and speed tuning. Additional studies that more clearly separate cell classes or probe functional specialization using novel stimulus sets or visually-guided behaviors may provide useful further clarification on how cell types across the visual cortex differentially process and use visual information.

1.6 Tables

Table 1.1: Electrophysiology comparisons across regions per layer. Bolded black p-values are comparisons significant both with the by cell analysis and the hierarchical bootstrap. Non-bold red p-values are comparisons that are significant by cell, but not by hierarchical bootstrap. Bold red p-values are comparisons that are significant by hierarchical bootstrap, but not by cell. Non-bold black p-values are comparisons that did not reach significance for both methods. For Kruskal-Wallis followed by Dunn's post hoc test and Šidàk multiple comparisons, significance set at $p<0.05$. For Hierarchical bootstrap, significance set at $p<0.025$.

		Multiple Comparisons			Hierarchical Bootstrap		
	Kruskal -Wallis	V1 vs. AL	AL vs. PM	V1 vs. PM	AL vs. V1	AL vs. PM	PM vs. V1
L2/3 TF	0.020	**0.018**	0.073	0.748	**0.015**	0.025	0.358
L2/3 SF	0.550	-	-	-	0.262	0.298	0.434
L2/3 TF/SF	0.025	0.020	0.139	0.567	0.194	0.529	0.190
L4 TF	0.151	-	-	-	0.338	0.027	0.048
L4 SF	0.003	**0.156**	**0.002**	0.071	**0.016**	**0.001**	0.036
L4 TF/SF	0.001	0.036	**4.66E-04**	0.114	0.206	**0.025**	0.084
L5/6 TF	3.57E-05	0.001	**1.91E-04**	0.963	0.059	**0.008**	0.195
L5/6 SF	0.310	-	-	-	0.350	0.231	0.423
L5/6 TF/SF	0.006	0.163	0.005	0.494	0.425	0.072	0.165

Table 1.2: Electrophysiology comparisons, across layers per region. Bolded black p-values are comparisons significant both with the by cell analysis and the hierarchical bootstrap. Non-bold red p-values are comparisons that are significant by cell, but not by hierarchical bootstrap. Bold red p-values are comparisons that are significant by hierarchical bootstrap, but not by cell. Non-bold black p-values are comparisons that did not reach significance for both methods. For Kruskal-Wallis followed by Dunn's post hoc test and Šidàk multiple comparisons, significance set at $p<0.05$. For Hierarchical bootstrap, significance set at $p<0.025$.

		Multiple Comparisons			Hierarchical Bootstrap		
Test Variable	Kruskal -Wallis	L2/3 vs L4	L2/3 vs L5/6	L4 vs L5/6	L2/3 vs L4	L2/3 vs L5/6	L4 vs L5/6
V1 TF	0.097	-	-	-	0.030	0.034	0.359
V1 SF	0.349	-	-	-	0.387	0.338	0.462
V1 TF/SF	0.071	-	-	-	0.142	0.082	0.307
AL TF	0.992	-	-	-	0.434	0.498	0.405
AL SF	0.107	-	-	-	0.086	0.449	**0.003**
AL TF/SF	0.215	-	-	-	0.173	0.195	0.383
PM TF	0.541	-	-	-	0.425	0.180	0.197
PM SF	0.027	0.035	0.907	**0.042**	0.059	0.431	**0.016**
PM TF/SF	0.179	-	-	-	0.139	0.441	0.103

Table 1.3: Electrophysiology comparisons, no layers. Bolded black p-values are comparisons significant both with the by cell analysis and the hierarchical bootstrap. Non-bold red p-values are comparisons that are significant by cell, but not by hierarchical bootstrap. Bold red p-values are comparisons that are significant by hierarchical bootstrap, but not by cell. Non-bold black p-values are comparisons that did not reach significance for both methods. For Kruskal-Wallis followed by Dunn's post hoc test and Šidàk multiple comparisons, significance set at $p<0.05$. For Hierarchical bootstrap, significance set at $p<0.025$

		Multiple Comparisons			Hierarchical Bootstrap		
	Kruskal-Wallis	V1 vs. AL	AL vs. PM	V1 vs. PM	AL vs. V1	AL vs. PM	PM vs. V1
TF	9.58E-08	**1.05E-05**	**6.57E-07**	0.841	**0.018**	**0.001**	0.102
SF	0.126	-	-	-	0.235	0.041	0.270
TF/SF	6.70E-06	0.002	**6.36E-06**	0.344	0.227	**0.023**	0.176
xi	1.30E-05	**1.07E-05**	**0.008**	0.571	**0.003**	**0.019**	0.322
speed	0.035	0.442	0.034	0.549	0.356	0.349	0.417

Table 1.4: 2PCI comparisons between regions per L5 cell type. Bolded black p-values are comparisons significant both with the by cell analysis and the hierarchical bootstrap. Non-bold red p-values are comparisons that are significant by cell, but not by hierarchical bootstrap. Bold red p-values are comparisons that are significant by hierarchical bootstrap, but not by cell. Non-bold black p-values are comparisons that did not reach significance for both methods. For Kruskal-Wallis followed by Dunn's post hoc test and Šidàk multiple comparisons, significance set at $p<0.05$. For Hierarchical bootstrap, significance set at $p<0.025$.

		Multiple Comparisons			Hierarchical Bootstrap		
Test Variable	Kruskal-Wallis	AL vs. V1	AL vs. PM	PM vs. V1	AL vs. V1	AL vs. PM	PM vs. V1
L5IT TF	3.44E-10	**1.23E-10**	**0.001**	0.007	**1.40E-04**	**0.013**	0.068
L5IT SF	6.64E-05	**5.83E-04**	**2.04E-04**	0.968	**0.002**	**0.002**	0.422
L5IT TF/SF	1.73E-13	**5.53E-13**	1.54E-08	0.436	**0.005**	0.052	0.122
L5ET TF	0.014	0.021	0.049	0.983	0.130	0.042	0.279
L5ET SF	9.72E-06	**7.89E-06**	**0.002**	0.979	**5.00E-06**	**0.007**	0.222
L5ET TF/SF	1.28E-07	**1.98E-07**	**6.70E-05**	1.000	**1.00E-05**	**7.29E-04**	0.393
L5IT xi	1.73E-04	0.013	0.524	**1.91E-04**	0.105	0.286	**0.037**
L5ET xi	4.91E-06	0.043	**0.017**	**4.74E-06**	0.059	**0.014**	**3.18E-04**
L5IT speed	9.93E-05	**0.002**	**2.96E-04**	0.999	**0.021**	**0.005**	0.281
L5ET speed	0.324	-	-	-	0.051	0.112	0.367
L5IT OSI	0.087	-	-	-	0.279	0.485	0.306
L5ET OSI	0.053	-	-	-	0.246	0.048	0.287
L5IT DSI	0.028	0.203	0.762	0.025	0.175	0.400	0.086
L5ET DSI	0.089	-	-	-	0.136	0.223	0.490

Table 1.5: 2PCI comparisons between L5 cell types Bolded black p-values are comparisons significant both with the by cell analysis and the hierarchical bootstrap. Non-bold red p-values are comparisons that are significant by cell, but not by hierarchical bootstrap. Bold red p-values are comparisons that are significant by hierarchical bootstrap, but not by cell. Non-bold black p-values are comparisons that did not reach significance for both methods. For Wilcoxon Rank-Sum, significance set at $p<0.05$. For Hierarchical bootstrap, significance set at $p<0.025$.

	Rank-Sum	Hierarchical Bootstrap
Test Variable	L5IT vs. L5ET	L5ET vs. L5IT
V1 TF	0.035	0.048
V1 SF	0.013	0.041
V1 TF/SF	0.716	0.251
AL TF	0.644	0.298
AL SF	0.902	0.460
AL TF/SF	0.965	0.288
PM TF	0.455	0.381
PM SF	0.298	0.386
PM TF/SF	0.264	0.058
V1 xi	0.718	0.384
AL xi	0.513	0.264
PM xi	**0.004**	**0.021**
V1 speed	0.246	0.305
AL speed	0.931	0.358
PM speed	0.001	0.044
V1 OSI	0.016	0.272
AL OSI	0.120	0.759
PM OSI	0.111	0.135
V1 DSI	**4.77E-06**	**0.015**
AL DSI	**9.90E-05**	**0.006**
PM DSI	**4.25E-06**	**0.012**

1.7 Appendix

Supporting Table S1.1: Summary of electrophysiology experiments. Columns are by mouse per recorded region with each mouse's I.D., sex, age, and whether viral vectors were injected (see Materials and Methods). Units resp are the total number of visually responsive units per mouse. Units fit are the total number of units well-fit by the 2-D Gaussian function for estimating speed tuning. The percentage at the bottom of each region represents the total percentage of neurons per region that were well-fit by the 2-D Gaussian function.

Mouse	Sex	Age	Injected?	Units Resp	Units Fit
V1					
HRV108	M	106	Y	18	7
HRv109	M	125	Y	44	25
HRV114	M	132	Y	15	7
HRV115	F	140	Y	38	26
HRV119	M	124	Y	18	13
HRV123	F	139	Y	56	22
HRV124	M	127	Y	27	19
HV115	F	71	N	40	23
Total				256	142
%					55%
AL					
HR20	F	106	Y	34	25
HR23	F	138	Y	22	5
HR24	M	126	Y	24	22
PV01	F	119	Y	25	14
H15	F	70	N	29	14
H16	F	70	N	20	16
H17	M	79	N	15	9
H18	M	78	N	37	24
H19	M	79	N	24	9
Total				230	138
%					60%
PM					
HR20	F	106	Y	39	16
HR23	F	138	Y	30	18
PV01	F	119	Y	28	15
H15	F	70	N	57	22
H16	F	70	N	7	3
PV07	M	72	Y	7	2
h18	M	78	N	27	18
h17	M	79	N	23	2
Total				218	96
%					44%

Supporting Table S1.2: Summary of 2-photon calcium imaging experiments. Top corresponds to animals used for SF, TF tuning experiments (STF). Bottom corresponds to animals used for orientation tuning experiments (ORI). Columns correspond to the mouse I.D., sex, and age of animals used. AL/PM/V1 total are the total number of cell body regions of interest (ROIs) in each animal. AL/PM/V1 resp are the number of visually responsive ROIs. Percentage at the bottom of each "resp" column is the total percentage of ROIs that were visually responsive across all animals per region per experiment. AL/PM/V1 fit are the number of well-fit neurons by the 2-D Gaussian function for speed tuning. Percentages at the bottom of each "fit" column is the total percentage of responsive ROIs that were well-fit.

STF Experiments										
L5IT	**Age**	**AL total**	**AL resp**	**AL fit**	**PM total**	**PM resp**	**PM fit**	**V1 total**	**V1 resp**	**V1 fit**
ES02	69	69	35	11	85	34	6	145	119	49
ES05	99	474	117	43	384	151	42	236	65	18
ES09	108	399	59	35	391	50	17	146	22	8
ES13	75	171	8	3	427	19	8	354	57	25
ES19	85	296	92	69	405	94	60	383	93	48
ES21	93	NA	NA	NA	281	39	19	153	42	12
ES23	95	500	56	28	244	30	11	287	88	48
Total		1909	367	189	2217	417	163	1704	486	208
Percent			19%	51%		19%	39%		29%	43%
L5ET	**Age**	**AL total**	**AL resp**	**AL fit**	**PM total**	**PM resp**	**PM fit**	**V1 total**	**V1 resp**	**V1 fit**
ES10	101	234	12	5	314	45	9	219	25	8
ES12	106	249	47	23	256	41	11	266	102	25
ES14	109	169	31	14	340	21	7	190	97	32
ES16	119	200	23	12	181	13	6	314	54	29
ES20	80	280	54	19	NA	NA	NA	467	83	35
Total		1132	167	73	1091	120	33	1456	361	129
Percent			15%	44%		11%	28%		25%	36%

ORI Experiments							
L5IT	**Age**	**AL total**	**AL resp**	**PM total**	**PM resp**	**V1 total**	**V1 resp**
ES05	99	474	103	384	81	236	52
ES09	108	399	59	391	46	146	19
ES13	75	171	16	427	31	354	81
ES19	85	296	70	405	104	383	52
ES21	93	NA	NA	281	27	153	25
ES23	95	500	62	244	14	287	45
Total		1840	310	2132	303	1559	274
Percent			17%		14%		18%
L5ET	**Age**	**AL total**	**AL resp**	**PM total**	**PM resp**	**V1 total**	**V1 resp**
ES10	101	234	12	314	17	219	26
ES12	106	249	46	256	18	266	30
ES14	109	169	51	340	19	190	43
ES16	119	200	38	NA	NA	314	54
ES20	80	280	24	453	27	467	61
Total		1132	171	1363	81	1456	214
Percent			15%		6%		15%

1.8 Acknowledgements

We would like to thank members of the Callaway lab for helpful discussion, in particular P. Li and K. Salinas for comments on the manuscript. This work was supported by the NIH grants EY022577(EMC) and EY029932 (HW). Chapter 1, in full, is currently being prepared for submission for publication and will include Oyshi Dey and Willian N Lagos as co-authors and Professor Edward Callaway as the senior author. The dissertation author was the primary investigator and author of this material.

1.9 References

Adelson, E. H., & Bergen, J. R. (1985). Spatiotemporal energy models for the perception of motion. *J. Opt. Soc. Am. A*, *2*(2).

Andermann, M. L., Kerlin, A. M., Roumis, D. K., Glickfeld, L. L., & Reid, R. C. (2011). Functional specialization of mouse higher visual cortical areas. *Neuron*, *72*(6), 1025–1039. https://doi.org/10.1016/j.neuron.2011.11.013

Baker, A., Kalmbach, B., Morishima, M., Kim, J., Juavinett, A., Li, N., & Dembrow, N. (2018). Specialized subpopulations of deep-layer pyramidal neurons in the neocortex: Bridging cellular properties to functional consequences. *Journal of Neuroscience*, *38*(24), 5441–5455. https://doi.org/10.1523/JNEUROSCI.0150-18.2018

Blot, A., Roth, M. M., Gasler, I., Javadzadeh, M., Imhof, F., & Hofer, S. B. (2021). Visual intracortical and transthalamic pathways carry distinct information to cortical areas. *Neuron*, *109*(12), 1996-2008.e6. https://doi.org/10.1016/j.neuron.2021.04.017

Daigle, T. L., Madisen, L., Hage, T. A., Valley, M. T., Knoblich, U., Larsen, R. S., Takeno, M. M., Huang, L., Gu, H., Larsen, R., Mills, M., Bosma-Moody, A., Siverts, L. A., Walker, M., Graybuck, L. T., Yao, Z., Fong, O., Nguyen, T. N., Garren, E., Lenz, G. H., Chavarha, M., Pendergraft, J., Harrington, J., Hirokawa, K. E., Harris, J. A., Nicovich, P. R., McGraw, M. J., Ollerenshaw, D. R., Smith, K. A., Baker, C. A., Ting, J. T., Sunkin, S. M., Lecoq, J., Lin, M. Z., Boyden, E. S., Murphy, G. J., da Costa, N. M., Waters, J., Li, L., Tasic, B., & Zeng, H. (2018). A Suite of Transgenic Driver and Reporter Mouse Lines with Enhanced Brain-Cell-Type Targeting and Functionality. *Cell*, *174*(2), 465-480.e22. https://doi.org/10.1016/J.CELL.2018.06.035

Dataset: Allen Institute MindScope Program. (2019). Allen Brain Observatory -- Neuropixels Visual Coding [dataset]. brain-map.org/explore/circuits

DeNardo, L. A., Berns, D. S., DeLoach, K., & Luo, L. (2015). Connectivity of mouse somatosensory and prefrontal cortex examined with trans-synaptic tracing. *Nature Neuroscience*, *18*(11), 1687–1697. https://doi.org/10.1038/nn.4131

D'Souza, R. D., Bista, P., Meier, A. M., Ji, W., & Burkhalter, A. (2019). Spatial Clustering of Inhibition in Mouse Primary Visual Cortex. *Neuron*, *104*(3), 588-600.e5. https://doi.org/10.1016/j.neuron.2019.09.020

Du, J., Blanche, T. J., Harrison, R. R., Lester, H. A., & Masmanidis, S. C. (2011). Multiplexed, High Density Electrophysiology with Nanofabricated Neural Probes. *PLoS ONE*, *6*(10), e26204. https://doi.org/10.1371/journal.pone.0026204

Garrett, M. E., Nauhaus, I., Marshel, J. H., & Callaway, E. M. (2014). Topography and Areal Organization of Mouse Visual Cortex. *Journal of Neuroscience*, *34*(37), 12587–12600. https://doi.org/10.1523/JNEUROSCI.1124-14.2014

Gerfen, C. R., Paletzki, R., & Heintz, N. (2013). GENSAT BAC Cre-Recombinase Driver Lines to Study the Functional Organization of Cerebral Cortical and Basal Ganglia Circuits. *Neuron*, *80*(6), 1368–1383. https://doi.org/10.1016/j.neuron.2013.10.016

Glickfeld, L. L., Andermann, M. L., Bonin, V., & Reid, R. C. (2013). Cortico-cortical projections in mouse visual cortex are functionally target specific. *Nature Neuroscience*, *16*(2), 219–226. https://doi.org/10.1038/nn.3300

Glickfeld, L. L., & Olsen, S. R. (2017). Higher-Order Areas of the Mouse Visual Cortex. *Annu. Rev. Vis. Sci*, *3*, 251–273. https://doi.org/10.1146/annurev-vision-102016

Harris, J. A., Mihalas, S., Hirokawa, K. E., Whitesell, J. D., Choi, H., Bernard, A., Bohn, P., Caldejon, S., Casal, L., Cho, A., Feiner, A., Feng, D., Gaudreault, N., Gerfen, C. R., Graddis, N., Groblewski, P. A., Henry, A. M., Ho, A., Howard, R., Knox, J. E., Kuan, L., Kuang, X., Lecoq, J., Lesnar, P., Li, Y., Luviano, J., Mcconoughey, S., Mortrud, M. T., Naeemi, M., Ng, L., Oh, S. W., Ouellette, B., Shen, E., Sorensen, S. A., Wakeman, W., Wang, Q., Wang, Y., Williford, A., Phillips, J. W., Jones, A. R., Koch, C., & Zeng, H. (2019). Hierarchical organization of cortical and thalamic connectivity. *Nature*, *575*(7781), 195–202. https://doi.org/10.1038/s41586-019-1716-z

Harris, K. D., Quiroga, R. Q., Freeman, J., & Smith, S. L. (2016). Improving data quality in neuronal population recordings. *Nature Neuroscience*, *19*(9), 1165–1174. https://doi.org/10.1038/nn.4365

Huh, C. Y., Peach, J. P., Bennett, C., Vega, R. M., & Hestrin, S. (2018). Feature-Specific Organization of Feedback Pathways in Mouse Visual Cortex. *Current Biology*, *28*, 114-120.e5. https://doi.org/10.1016/j.cub.2017.11.056

Ji, W., Gămănuţ, R., Bista, P., D'Souza, R. D., Wang, Q., & Burkhalter, A. (2015). Modularity in the Organization of Mouse Primary Visual Cortex. *Neuron*, *87*(3), 632–643. https://doi.org/10.1016/j.neuron.2015.07.004

Jin, M., & Glickfeld, L. L. (2020). Mouse Higher Visual Areas Provide Both Distributed and Specialized Contributions to Visually Guided Behaviors. *Current Biology*, *30*(23), 4682-4692.e7. https://doi.org/10.1016/j.cub.2020.09.015

Juavinett, A. L., Nauhaus, I., Garrett, M. E., Zhuang, J., & Callaway, E. M. (2016). Automated identification of mouse visual areas with intrinsic signal imaging. *Nature Protocols*, *12*(1), 32–43. https://doi.org/10.1038/nprot.2016.158

Kerlin, A. M., Andermann, M. L., Berezovskii, V. K., & Reid, R. C. (2010). Broadly Tuned Response Properties of Diverse Inhibitory Neuron Subtypes in Mouse Visual Cortex. *Neuron*, *67*(5), 858–871. https://doi.org/10.1016/j.neuron.2010.08.002

Kim, E. J., Juavinett, A. L., Kyubwa, E. M., Jacobs, M. W., & Callaway, E. M. (2015). Three Types of Cortical Layer 5 Neurons That Differ in Brain-wide Connectivity and Function. *Neuron*, *88*(6), 1253–1267. https://doi.org/10.1016/j.neuron.2015.11.002

Kim, E. J., Zhang, Z., Huang, L., Ito-Cole, T., Jacobs, M. W., Juavinett, A. L., Senturk, G., Hu, M., Ku, M., Ecker, J. R., & Callaway, E. M. (2020). Extraction of Distinct Neuronal Cell Types from within a Genetically Continuous Population. *Neuron*, *107*(2), 274-282.e6. https://doi.org/10.1016/j.neuron.2020.04.018

Kim, M. H., Znamenskiy, P., Iacaruso, M. F., & Mrsic-Flogel, T. D. (2018). Segregated Subnetworks of Intracortical Projection Neurons in Primary Visual Cortex. *Neuron*, *100*(6), 1313-1321.e6. https://doi.org/10.1016/j.neuron.2018.10.023

Kirchgessner, M. A., Franklin, A. D., & Callaway, E. M. (2021). Distinct "driving" versus "modulatory" influences of different visual corticothalamic pathways. *Current Biology*, S0960982221012653. https://doi.org/10.1016/j.cub.2021.09.025

Ledue, E. E., Zou, M. Y., & Crowder, N. A. (2012). Spatiotemporal tuning in mouse primary visual cortex. *Neuroscience Letters*, *528*, 165–169. https://doi.org/10.1016/j.neulet.2012.09.006

Legendre, P., & Legendre, L. (1998). Ecological resemblance. In *Numerical Ecology* (Vol. 20, pp. 247–302). Elsevier. https://doi.org/10.1016/S0167-8892(98)80059-6

Li, J. Y., Hass, C. A., Matthews, I., Kristl, A. C., & Glickfeld, L. L. (2020). *Distinct recruitment of feed-forward and recurrent pathways across higher-order areas of mouse visual cortex* [Preprint]. Neuroscience. https://doi.org/10.1101/2020.09.24.312140

Lur, G., Vinck, M. A., Tang, L., Cardin, J. A., & Higley, M. J. (2016). Projection-Specific Visual Feature Encoding by Layer 5 Cortical Subnetworks. *Cell Reports*, *14*(11), 2538–2545. https://doi.org/10.1016/j.celrep.2016.02.050

Lyon, D. C., Nassi, J. J., & Callaway, E. M. (2010). A Disynaptic Relay from Superior Colliculus to Dorsal Stream Visual Cortex in Macaque Monkey. *Neuron*, *65*(2), 270–279. https://doi.org/10.1016/j.neuron.2010.01.003

Marshel, J. H., Garrett, M. E., Nauhaus, I., & Callaway, E. M. (2011). Functional specialization of seven mouse visual cortical areas. *Neuron*, *72*(6), 1040–1054. https://doi.org/10.1016/j.neuron.2011.12.004

Maruoka, H., Nakagawa, N., Tsuruno, S., Sakai, S., Yoneda, T., & Hosoya, T. (2017). Lattice system of functionally distinct cell types in the neocortex. *Science*, *358*(6363), 610–615. https://doi.org/10.1126/science.aam6125

Mesa, N., Waters, J., & de Vries, S. E. J. (2021). The effect of inclusion criteria on the functional properties reported in mouse visual cortex. *ENeuro*, *8*(1), 1–9. https://doi.org/10.1523/ENEURO.0188-20.2021

Mishkin, M., Ungerleider, L. G., & Macko, K. A. (1983). Object vision and spatial vision: Two cortical pathways. *Trends in Neurosciences*, *6*, 414–417. https://doi.org/10.1016/0166-2236(83)90190-X

Movshon, J. A. (1975). The velocity tuning of single units in cat striate cortex. *The Journal of Physiology*, *249*(3), 445–468. https://doi.org/10.1113/jphysiol.1975.sp011025

Murakami, T., Matsui, T., & Ohki, K. (2017). Functional segregation and development of mouse higher visual areas. *Journal of Neuroscience*, *37*(39), 9424–9437. https://doi.org/10.1523/JNEUROSCI.0731-17.2017

Nassi, J. J., & Callaway, E. M. (2009). Parallel processing strategies of the primate visual system. *Nature Reviews Neuroscience*, *10*(5), 360–372. https://doi.org/10.1038/nrn2619

Niell, C. M., & Stryker, M. P. (2010). Modulation of Visual Responses by Behavioral State in Mouse Visual Cortex. *Neuron*, *65*(4), 472–479. https://doi.org/10.1016/j.neuron.2010.01.033

Ohki, K., Chung, S., Ch'ng, Y. H., Kara, P., & Reid, R. C. (2005). Functional imaging with cellular resolution reveals precise micro-architecture in visual cortex. *Nature*, *433*(7026), 597–603. https://doi.org/10.1038/nature03274

Pachitariu, M., Steinmetz, N., Kadir, S., Carandini, M., & Harris, K. D. (2016). Kilosort: Realtime spike-sorting for extracellular electrophysiology with hundreds of channels. *BioRxiv*, 061481. https://doi.org/10.1101/061481

Pachitariu, M., Stringer, C., Schröder, S., Dipoppa, M., Rossi, L. F., Carandini, M., & Harris, K. D. (2016). Suite2p: Beyond 10,000 neurons with standard two-photon microscopy. *BioRxiv*, 061507. https://doi.org/10.1101/061507

Pettersen, K. H., Devor, A., Ulbert, I., Dale, A. M., & Einevoll, G. T. (2006). Current-source density estimation based on inversion of electrostatic forward solution: Effects of finite extent of neuronal activity and conductivity discontinuities. *Journal of Neuroscience Methods*, *154*(1–2), 116–133. https://doi.org/10.1016/j.jneumeth.2005.12.005

Priebe, N. J., Cassanello, C. R., & Lisberger, S. G. (2003). The neural representation of speed in macaque area MT/V5. *The Journal of Neuroscience*, *23*(13), 5650–5661. https://doi.org/23/13/5650 [pii]

Priebe, N. J., Lisberger, S. G., & Movshon, J. A. (2006). Tuning for Spatiotemporal Frequency and Speed in Directionally Selective Neurons of Macaque Striate Cortex. *Journal of Neuroscience*, *26*(11), 2941–2950. https://doi.org/10.1523/JNEUROSCI.3936-05.2006

Roth, M. M., Helmchen, F., & Kampa, B. M. (2012). Distinct Functional Properties of Primary and Posteromedial Visual Area of Mouse Neocortex. *Journal of Neuroscience*, *32*(28), 9716–9726. https://doi.org/10.1523/JNEUROSCI.0110-12.2012

Salinas, K. J., Huh, C. Y. L., Zeitoun, J. H., & Gandhi, S. P. (2021). Functional Differentiation of Mouse Visual Cortical Areas Depends upon Early Binocular Experience. *The Journal of Neuroscience*, *41*(7), 1470–1488. https://doi.org/10.1523/JNEUROSCI.0548-20.2020

Saravanan, V., Berman, G. J., & Sober, S. J. (2020). Application of the hierarchical bootstrap to multi-level data in neuroscience. *Neurons, Behavior, Data Analysis and Theory*, *3*(5),

https://nbdt.scholasticahq.com/article/13927-application-of-the-hierarchical-bootstrap-to-multi-level-data-in-neuroscience. https://www.ncbi.nlm.nih.gov/pmc/articles/PMC7906290/

Schmitzer-Torbert, N., Jackson, J., Henze, D., Harris, K., & Redish, A. D. (2005). Quantitative measures of cluster quality for use in extracellular recordings. *Neuroscience*, *131*(1), 1–11. https://doi.org/10.1016/j.neuroscience.2004.09.066

Shobe, J. L., Claar, L. D., Parhami, S., Bakhurin, K. I., & Masmanidis, S. C. (2015). Brain activity mapping at multiple scales with silicon microprobes containing 1,024 electrodes. *Journal of Neurophysiology*, *114*(3), 2043–2052. https://doi.org/10.1152/jn.00464.2015

Siegle, J. H., Jia, X., Durand, S., Gale, S., Bennett, C., Graddis, N., Heller, G., Ramirez, T. K., Choi, H., Luviano, J. A., Groblewski, P. A., Ahmed, R., Arkhipov, A., Bernard, A., Billeh, Y. N., Brown, D., Buice, M. A., Cain, N., Caldejon, S., Casal, L., Cho, A., Chvilicek, M., Cox, T. C., Dai, K., Denman, D. J., de Vries, S. E. J., Dietzman, R., Esposito, L., Farrell, C., Feng, D., Galbraith, J., Garrett, M., Gelfand, E. C., Hancock, N., Harris, J. A., Howard, R., Hu, B., Hytnen, R., Iyer, R., Jessett, E., Johnson, K., Kato, I., Kiggins, J., Lambert, S., Lecoq, J., Ledochowitsch, P., Lee, J. H., Leon, A., Li, Y., Liang, E., Long, F., Mace, K., Melchior, J., Millman, D., Mollenkopf, T., Nayan, C., Ng, L., Ngo, K., Nguyen, T., Nicovich, P. R., North, K., Ocker, G. K., Ollerenshaw, D., Oliver, M., Pachitariu, M., Perkins, J., Reding, M., Reid, D., Robertson, M., Ronellenfitch, K., Seid, S., Slaughterbeck, C., Stoecklin, M., Sullivan, D., Sutton, B., Swapp, J., Thompson, C., Turner, K., Wakeman, W., Whitesell, J. D., Williams, D., Williford, A., Young, R., Zeng, H., Naylor, S., Phillips, J. W., Reid, R. C., Mihalas, S., Olsen, S. R., & Koch, C. (2021). Survey of spiking in the mouse visual system reveals functional hierarchy. *Nature*, *592*(7852), 86–92. https://doi.org/10.1038/s41586-020-03171-x

Siegle, J. H., Ledochowitsch, P., Jia, X., Millman, D. J., Ocker, G. K., Caldejon, S., Casal, L., Cho, A., Denman, D. J., Durand, S., Groblewski, P. A., Heller, G., Kato, I., Kivikas, S., Lecoq, J., Nayan, C., Ngo, K., Nicovich, P. R., North, K., Ramirez, T. K., Swapp, J., Waughman, X., Williford, A., Olsen, S. R., Koch, C., Buice, M. A., & de Vries, S. E. (2021). Reconciling functional differences in populations of neurons recorded with two-photon imaging and electrophysiology. *ELife*, *10*, e69068. https://doi.org/10.7554/eLife.69068

Siegle, J. H., López, A. C., Patel, Y. A., Abramov, K., Ohayon, S., & Voigts, J. (2017). Open Ephys: An open-source, plugin-based platform for multichannel electrophysiology. *Journal of Neural Engineering*, *14*(4), 045003. https://doi.org/10.1088/1741-2552/aa5eea

Tang, L., & Higley, M. J. (2020). Layer 5 Circuits in V1 Differentially Control Visuomotor Behavior. *Neuron*, *105*(2), 346-354.e5. https://doi.org/10.1016/j.neuron.2019.10.014

Wang, Q., & Burkhalter, A. (2007). Area map of mouse visual cortex. *Journal of Comparative Neurology*, *502*(3), 339–357. https://doi.org/10.1002/cne.21286

Zhang, Z., Zhou, J., Tan, P., Pang, Y., Rivkin, A. C., Kirchgessner, M. A., Williams, E., Lee, C.-T., Liu, H., Franklin, A. D., Miyazaki, P. A., Bartlett, A., Aldridge, A. I., Vu, M., Boggeman, L., Fitzpatrick, C., Nery, J. R., Castanon, R. G., Rashid, M., Jacobs, M. W., Ito-Cole, T., O'Connor, C., Pinto-Duartec, A., Dominguez, B., Smith, J. B., Niu, S.-Y., Lee, K.-F., Jin, X., Mukamel, E. A., Behrens, M. M., Ecker, J. R., & Callaway, E. M. (2021). Epigenomic diversity of cortical

projection neurons in the mouse brain. *Nature*, *598*(7879), 167–173. https://doi.org/10.1038/s41586-021-03223-w

Chapter 2. Functional and anatomical differences in layer 4 of mouse visual cortex.

2.1 Abstract

In primates, layer 4 of the primary visual cortex (V1) receives separated, parallel inputs from the magnocellular and parvocellular pathways. These pathways are biased to prefer fast/coarse versus fine/slow visual features. Due to the lack of strong anatomical organization for visual tuning in the mouse primary visual cortex, it is not known if layer 4 of mouse V1 also has neurons that are similarly organized for fast/coarse versus fine/slow visual information. Here, we characterize two layer 4 transgenic mouse lines (Nr5a1-Cre and Scnn1a-Tg3-Cre) using cell counting and 2-photon calcium imaging functional studies. We find that the layer 4 neurons labeled by these two mouse lines differ in their laminar distribution, with Nr5a1 neurons in more superficial depths of layer 4. Analysis of morphological reconstructions from the Allen Cell Types database also reveal differences in apical dendrite length between these two mouse lines. Functionally, we find that Nr5a1 neurons prefer fast speeds, low spatial frequencies, and high temporal frequencies, while Scnn1a-Tg3 neurons prefer the opposite. We also find that Nr5a1 neurons are more direction selective than Scnn1a-Tg3 neurons. This suggests that these two mouse lines express Cre recombinase in populations that are biased toward layer 4 neurons with distinct functional properties. Whether these differences are due to different inputs from the retina and/or the dorsal lateral geniculate nucleus will be of interest in future studies.

2.2 Introduction

The mammalian neocortex is organized into distinct layers that play different roles in cortical circuits. In many primary sensory cortical areas, layer 4 (L4) is thought to receive feed-forward input from a primary thalamic nucleus that is subsequently relayed to other layers of

cortex. In the primary visual cortex (V1), the dorsal lateral geniculate nucleus (dLGN) provides thalamic input to layer 4. In primates, different layer 4 cell types can be separated based on their dLGN input, morphology, laminar location, and functional properties (Nassi & Callaway, 2009). For example, parallel streams of coarse versus fine visual information from the dLGN enter layer 4Cα and layer 4Cβ respectively. These parallel channels originate from distinct retinal ganglion cell types (RGCs) (parasol versus midget), that are biased for high temporal frequency (TF), low spatial frequency (SF) and low TF, high SF information respectively and remain segregated in the dLGN through the magnocellular (M) and parvocellular (P) pathways (Nassi & Callaway, 2009).

Due to the prevalence of many genetic and viral tools in mice, the mouse visual system has become a popular model for understanding how specific cell types and circuits are organized to process visual information. Many functional and anatomical studies in mice have revealed conserved visual features, such as neuronal tuning for orientation, spatial frequency, and temporal frequency, and a hierarchical organization of visual areas (Niell & Stryker, 2008; Siegle et al., 2021). However, it is also clear that there are stark differences in the organization and wiring of the mouse visual system compared to primates, such as a salt and pepper organization of tuning features rather than columnar orientation pinwheels (Ohki et al., 2005; Ohki & Reid, 2007).

Evidence of a parallel input organization like the M and P pathways in layer 4 of mouse V1 is weak, with no evidence of laminar segregation of neurons tuned for different SFs and TFs or different inputs to neurons tuned for different SFs and TFs in V1. While it has been demonstrated that a potential “parallel” channel of direction selective information in mice is present from the retina to V1, this pathway arises from direction selective RGCs to the shell of

the dLGN and terminates primarily in layer 1 of V1 (Cruz-Martín et al., 2014). It is not known if inputs to mouse V1 layer 4 from the dLGN core are biased to neurons with different functional properties. A previous study that recorded single units across the full depth of V1 found a correlation between response latencies and tuning preferences for SF and TF that were similar to the patterns seen in the M and P channels of primates, but this study was not restricted to layer 4 (Gao et al., 2010). A recent functional study characterizing multiple transgenic mouse lines targeted to different layers and cell types includes two layer 4 mouse lines (Nr5a1-Cre and Scnn1a-Tg3-Cre), but found only modest differences in their tuning (de Vries et al., 2020). But this could potentially be due to a limited range of SFs and TFs sampled in this study since SF was sampled using static gratings, and TF was sampled at a single fixed SF.

Here we characterize two layer 4 transgenic mouse lines (Nr5a1-Cre and Scnn1a-Tg3-Cre) and find that their Cre expression is biased toward two different groups of functionally distinct layer 4 cells. Using cell-counting, we also find that these two mouse lines label layer 4 neurons that differ in their V1 depth. Analysis of these cells' apical dendrite morphologies using reconstructions from the Allen Brain Institute also demonstrates differences in apical dendrite length. Using 2-photon calcium imaging (2PCI) we find functional biases in these neurons and their preferred SF, TF, and speed using both drifting sine wave gratings and coherent dot motion stimuli. Additionally, these layer 4 mouse lines exhibit differences in orientation and direction selectivity. How these two groups of layer 4 neurons inherit and/or generate their tuning properties will be an important question to address and will potentially reveal if parallel spatiotemporal frequency channels in the retinogeniculocortical pathway are a conserved principle of visual organization in mammalian vision.

2.3 Methods

Animals

All experiments and procedures followed procedures approved by the Salk Animal Care and Use Committee. Male and female mice were used for all experiments. For 2PCI experiments, we used Nr5a1-Cre (n= 4) (JAX Stock No: 006364), Ai14/Nr5a1-Cre (n=1), Scnn1a-Tg3-Cre (JAX Stock No: 009613) (n=6), and Ai14/Scnn1a-Tg3-Cre (n=1) transgenic mice ranging in age from 84-115 days. For quantification of L4 neurons labeled by each line, we used Ai14/Nr5a1-Cre (n=3), Ai14/Scnn1a-Tg3-Cre (n=3), and Ai14/Nr5a1/Scnn1a-Tg3-Cre (n=3) mice ranging in age from 73-193 days.

Surgeries and viral injections

For all surgical procedures, mice were anesthetized with either isoflurane (0.5%-2%) or a ketamine/xylazine cocktail (100 mg/kg ketamine, 10 mg/kg xylazine) and secured in a stereotaxic frame. For all surgeries, animals were given analgesics (buprenorphine SR, 0.5-1.0 mg/kg, SQ) at the end of the procedure and provided ibuprofen medicated water (0.11 mg/mL). Intracranial injections were guided by stereotaxic coordinates relative to bregma, anterior-posterior (AP), medial-lateral (ML), and dorsal-ventral (DV).

For 2PCI experiments, mice were implanted with a custom-built circular headframe centered over the left hemisphere. Carprofen (5 mg/kg) and dexamethasone (2 mg/kg) were administered prior to craniotomy surgery. A large 3-5 mm craniotomy was drilled centered over V1 in the left hemisphere and AAV1-Syn-Flex-GCaMP6s-WPRE-SV40 (Addgene #100845) (200-250 nL, 9.25E12 GC/mL, UPenn or 150-200 nL, 7.5E12-1.5E13 GC/mL, Addgene) was injected into the middle of V1 (AP =-3.5 mm, ML=-2.65 mm, DV = -0.35 mm). Following

injections, the craniotomy was covered with a glass coverslip (Warner Instruments) mounted on a custom-built ring and sealed to the rest of the headframe with dental cement. Animals were allowed to recover while the virus was expressed over ~2-3 weeks.

For a subset of Ai14-crossed mice used in cell counting analysis, we labeled inhibitory neurons by retro-orbitally injecting AAVPHP.eB-mDlx-GFP-Fishell-1 (Addgene #83900) (50 uL, 6E12 GC/mL, Salk Vector Core) into the right eye.

In-vivo 2-photon calcium imaging

2PCI was performed on a custom microscope setup which includes a Sutter movable objective microscope (Sutter Instruments, Novato, CA) with a resonant scanner (Cambridge Instruments, Bedform, MA). Data acquisition was controlled by a customized version of Scanbox (Neurolabware, Los Angeles, CA). GCaMP6s was excited by a Ti:sapphire laser (Chameleon Ultra II, Coherent, Santa Clara, CA) at 920 nm. Imaging was collected at 1 or 3 planes. For uniplanar experiments, continuous unidirectional scanning was done at 15.49 Hz. For multi-planar experiments, an optotune lens was used to alternate between depths and a scanning rate of 5.16 Hz per plane. Planes were set ~20-30 μm apart. An area of approximately 500x720 μm (some experiments 800x1230 μm or 570x870 μm) was imaged using a 16x, 0.8 NA objective lens (Nikon Corporation, Tokyo, Japan) through the headframe filled with Immersol-W (Carl Zeiss Microscopy). Prior to imaging, mice were acclimated to the running wheel and visual stimulus setup over 3 days of training sessions. Running speed was recorded using a rotary encoder. During at least one of these training sessions, GCaMP6s expression was checked in V1. If the imaging field of view (FOV) over the area of expression was obscured due to tissue growth

or had poor expression of GCaMP6s, that region was not imaged. For each mouse, we imaged 1 FOV per session, per day.

Visual stimulation

Visual stimuli were generated using custom MATLAB code and Psychtoolbox-3 and presented on a gamma corrected monitor (Toshiba 40L5200U, 40'' or Asus PG279Q, 27'', both 60 Hz refresh rate) positioned ~13-23 cm away from the mouse's right eye. Prior to SF and TF tuning preferences characterization, receptive field locations were mapped by using flashed vertical and horizontal bars, or by manually moving a small drifting stimulus across the monitor until the location that elicited the strongest fluorescent response was identified. The bar receptive field stimuli consisted of vertical or horizontal bars that were 20-21° wide that tiled the entire screen and flashed from black to white over 2 seconds with a TF = 1 Hz and a gray pre/post-stimulus screen and was repeated 10-12 times. Responses to different bar locations were averaged across the entire field of view and the combination of vertical and horizontal bar positions that elicited the strongest response was set as the receptive field center.

SF, TF, and speed tuning were measured using a series of drifting sine wave gratings that varied in 5-6 SFs (0.01-0.32 cycles per degree (cpd) in octave increments), 5 TFs (0.5-7.5 Hz in octave increments), and 2-4 directions (0, 90, 180, 270° or 90, 180°) and were presented in a 40° diameter circular aperture. Each stimulus was repeated 12-15 times. For coherent dot motion experiments, black and white dots 2° in diameter drifted in two directions (90, 180°) within a 40° diameter circular aperture at varying speeds (0, 3.125-800 °/s in octave increments). Dot lifetime was to set 1 second, dot coherent 100%, and dot density 0.2 dots/deg. For orientation tuning experiments, drifting sine wave gratings varied across 8 directions (0-315° in 45° increments) at

a fixed SF and TF for each mouse line (Nr5a1 SF = 0.04 cpd, TF = 2 Hz; Scnn1a-Tg3 SF = 0.04 cpd, TF= 1 Hz) within a 40° diameter circular aperture. Each stimulus was repeated 15-20 times. For all experiments, stimulus conditions were presented randomly. For SF, TF, and orientation tuning experiments, a 2 second gray screen preceded and followed each 2 second stimulus presentation. For coherent dot motion experiments, the 2 seconds preceding and following the moving stimulus presentation consisted of stationary dots. For all experiments, a stimulus that consisted of a gray screen "blank" was interleaved randomly in 10% of trials. A few experiments (n=4) had blank trials that consisted of stationary dots during the coherent motion stimulus block, so the "blank" response was estimated using the pre- and post-stimulus presentation gray screen.

2-photon calcium imaging processing

Pre-processing was done using suite2p (Version 0.9.0), which included motion correction, cell body region-of-interests (ROI) detection, and neuropil estimation (Pachitariu et al., 2016). ROIs were visually inspected to include only cell bodies and cells that could be well-visualized in a max-intensity projection image of the registered frames. The fluorescent trace for each ROI and its corresponding neuropil was then extracted for data analysis. To estimate the contribution of the neuropil to the cell body response, the fluorescent traces were corrected using $F_{ROI\_corrected} = F_{ROI}(t) - \alpha F_{neuropil}(t)$ (Kerlin et al., 2010). The correction factor, α, was estimated by taking the average ratio of the fluorescence in the blood vessels of the FOV divided by the neuropil. For imaging sessions where 2 or more planes were simultaneously imaged, we identified overlapping ROIs that appeared in multiple planes by calculating the correlation coefficient between the normalized fluorescent signal of all neuron pairs within 25 pixels of each

other. ROI pairs with a correlation coefficient greater than 0.4 had the ROI with the lower mean fluorescent signal removed to avoid duplicate ROIs in the dataset.

ROI classification

For each ROI, the response to each trial was calculated by measuring the change in fluorescence from baseline, divided by baseline (dF/F). The baseline for each trial was taken as the mean fluorescence during the 2 second pre-stimulus period. ROIs that were not reliably responsive were eliminated based on 3 criteria. First, the mean fluorescence for the maximum trial condition had to be less than 6% of the maximum mean fluorescence for ROIs in the FOV. Second, these low fluorescence ROIs had to have a d-prime value ($\delta = (\mu_{max} - \mu_{blank})/(\sigma_{max} + \sigma_{blank})$) less than 0.5, where μ_{max} and μ_{blank} are the mean responses at the preferred and blank stimulus and σ_{max} and σ_{blank} are the standard deviation of the response at the preferred and blank stimulus (Marshel et al., 2011). Finally, some ROIs with extremely high dF/F due to division by a very small baseline were eliminated by removing any ROIs that had a trial dF/F that exceeded the median maximum trial dF/F per ROI + the 95% percentile maximum trial dF/F per ROI. ROIs were determined to be visually responsive for each experiment type (*e.g.* SF/TF experiments versus orientation tuning experiments) by one-way ANOVA with the blank condition included ($p<0.05$).

Quantification of tuning responses

All data analysis except for the Allen Brain Observatory datasets were analyzed in MATLAB R2018b. For Allen Visual Coding datasets, Python 3.6.10 was used to extract summary data for each ROI in Nr5a1-Cre and Scnn1a-Tg3-Cre V1 imaging experiments that was

subsequently analyzed and plotted in MATLAB. For 2PCI experiments, averaged responses to each stimulus condition were calculated by averaging the firing rate or dF/F during the stimulus presentation window. Trials were separated into running versus stationary trials based on the amount of movement that was recorded by the wheel encoder during each trial. For subsequent analysis, only stationary trials (<0.5 cm/s running) were used to avoid any confounds that running may have on neuronal activity (Niell & Stryker, 2010). Overall, approximately 61% of trials were stationary.

Estimation of visual tuning properties

SF, TF, and speed tuning were assessed by fitting the dF/F of each SF and TF combination to a modified 2-dimensional Gaussian function, below using lsqcurvefit in MATLAB (Priebe et al., 2003).

$$R(sf,tf) = A * exp\left(-\frac{\left((sf) - (sf_0)\ \right)^2}{2\sigma_{sf}^2}\right) * exp\left(-\frac{\left((tf) - \left(tf_p(sf)\right)\ \right)^2}{2\sigma_{tf}^2}\right)$$

where $tf_p(sf) = \xi(sf - sf_0) + tf_0$. Here A = amplitude of max firing, sf_0 = preferred SF, tf_o = preferred TF, σ_{sf} = SF tuning width (in octaves), σ_{tf} = TF tuning width (in octaves). The $tf_p(sf)$ variable accounts for the dependence of TF tuning on SF, where ξ is the speed tuning index/slope. When $\xi = 1$, the neuron is perfectly speed tuned as SF and TF vary in proportion. When $\xi = 0$, the cell is considered not speed tuned, as SF and TF tuning occur independently, and the preferred speed depends on the SF and TF. For neurons with high directional selectivity (DSI>0.4), only SF and TF trials in the preferred direction are included. Similarly, for neurons with orientation selectivity (OSI>0.2), only SF and TF trials at the preferred orientation were included. Trial responses below zero were rectified to zero prior to fitting. For neurons

responsive to all directions, all SF and TF trials were included for model fitting. 95% confidence intervals (CI) were generated by sampling with replacement 500 times. Only neurons that could be well-fit by the 2-D Gaussian were included for subsequent analysis. This criterion required that the 95% CI be less than 3 octaves for the SF_0, TF_0, and σ_{SF}, σ_{TF}, eliminating approximately 50- 70% of ROIs that were not well-fit. Neurons were considered "speed tuned" if the 95% CI for the speed tuning slope included a slope of 1, but not 0. All other cells were classified as "not speed tuned." The median value from the fits was taken as each neuron's speed tuning index and preferred speed (tf_0/sf_0). Sample fits are shown in Figure 2.3d.

Responses to coherent dot motion were estimated by fitting responses to each presented speed at the preferred direction to a smoothing spline in MATLAB using the fit function with the smoothing parameter set at 0.3. Neurons were considered well-fit if the 95% confidence interval (CI) for the preferred speed was less than 3 octaves. CIs were generated by sampling with replacement 500 times. From the fits, the preferred speed, upper and lower half max, and tuning half-widths were calculated. For neurons that were high or low pass, the upper and lower half max were set to NaN. A sample spline fit is shown in Figure 2.3e.

Orientation selectivity index and direction selectivity index (OSI and DSI) were calculated in the same manner as previous papers (Marshel et al., 2011).

$$OSI = (\mu_{max} - \mu_{orth})/(\mu_{max} + \mu_{orth})$$

$$DSI = (\mu_{max} - \mu_{opp})/(\mu_{max} + \mu_{opp})$$

where μ_{max} is the response at the preferred orientation/direction, μ_{orth} is the averaged response of the 2 directions orthogonal to the preferred, and μ_{opp} is the response opposite to the preferred. A small fraction of neurons (~9%) with either an OSI or DSI greater than 2 or less than 0 were

excluded from group analysis to match an exclusion criterion used by the Allen Brain Observatory Visual Coding dataset.

Histology

Animals were euthanized by intraperitoneal injection of euthasol (>100 mg/kg) and then perfused with phosphate-buffer saline (PBS), followed by 4% paraformaldehyde (PFA). Brains were removed from skulls and post-fixed in 2% PFA and 15% sucrose at 4C for 24 hours before being transferred to 30% sucrose at 4C for at least another 24 hours. Brains were sectioned coronally into 50 µm thick sections and then subsequently immunostained followed by DAPI staining. For all immunostaining experiments unless otherwise specified, sections were incubated with primary antibody at 4° overnight in 1% normal donkey serum/0.1% Triton-X 100 in PBS, followed by secondary antibody for 2 hours at room temperature.

For 2PCI brains, immunohistochemistry was performed to verify GCaMP6s viral expression by incubating sections with chicken anti-GFP (1:1000, GFP-1020, Aves Labs) followed by Alexa 488 donkey anti-chicken secondary (1:1000-1:500, 703-545-155, Jackson ImmunoResearch).

For cell counting sections, antigen retrieval was performed using 10 nM sodium citrate buffer and then sections were immunostained with rabbit anti-NeuN (1:1000, ab177487, Abcam), mouse anti-GAD67 (1:1000, MAB5406, MilliporeSigma), rat anti-RFP (1:1000, 5F8-100, Chromotek) followed by Alexa 488 donkey anti-rabbit (1:1000, A21207, Thermo Fisher), Alexa 647 donkey anti-mouse (1:500, A31571, Thermo Fisher), and CF568 donkey anti-rat (1:500, 89138-546, Biotium), secondaries. For cell counting brains where inhibitory neurons were labeled with mDlx virus, antigen retrieval was performed as before and then sections were

immunostained with rabbit anti-NeuN (1:1000, ab177487, Abcam), chicken anti-GFP (1:1000, GFP-1020, Aves Labs), and rat anti-RFP (1:1000, 5F8-100, Chromotek) followed by Alexa 647 donkey anti-rabbit (1:1000, A31573, Thermo Fisher), Alexa 488 donkey anti-chicken secondary (1:1000, 703-545-155, Jackson ImmunoResearch), and CF568 donkey anti-rat (1:500, 89138-546, Biotium) secondaries. Sections were first imaged on an Olympus BX63 microscope using a 10x/0.4 NA objective (Olympus) to identify the borders of V1 and layer 4. Sections for cell counting were then imaged on a Zeiss LSM880 confocal microscope using a 20x/0.8NA objective. A stitched z-stack image was taken so that the entirety of V1 in one of the hemispheres of that section could be used for quantification.

Cell counting

We used ImageJ and the Cell Counter plugin to quantify the number of neurons in layer 4 of V1 in each imaged section. We quantified the number of L4 neurons (NeuN), inhibitory neurons (GAD67 stain or mDlx virus), and tdT+ neurons labeled by each Ai14 mouse cross to estimate the proportion and depth of L4 excitatory neurons labeled by Nr5a1-Cre, Scnn1a-Tg3-Cre, and Nr5a1/Scnn1a-Tg3-Cre crossed mouse lines. We additionally counted all tdT+ neurons across the entire depth of V1 cortex since both mouse lines contain some non-layer 4 cortical expression. Counters were blinded to the mouse strain of the sections they were counting and were unblinded only after all sections were counted so that grouped analysis could be done. We found that both the GAD67 antibody and the mDlx virus labeled <10% of inhibitory neurons in layer 4, which is lower than the expected proportion of inhibitory neurons in cortex (~20%) (DeFelipe & Fariñas, 1992). Since both methods of labeling inhibitory neurons were similar, we analyzed these sections together and estimated the total number of layer 4 excitatory neurons by

multiplying the number of NeuN neurons by 0.8. Approximately 1-3 sections containing V1 from each mouse were quantified.

To estimate the depth within V1 of the neurons that Nr5a1 versus Scnn1a-Tg3-Cre mouse line labeled, we used ImageJ to first draw a line approximating the top and bottom edge of V1 in each section. Next, we created a Euclidean distance map based on these borders. We then used the Euclidean distance maps and the coordinates of each marked cell to calculate the distance of each tdT+ cell from the top and the bottom of the cortex. To account for variations in cortical thickness across sections, we normalized the depth as a fraction of the total thickness of cortex at that point (depth from top/(depth from top + depth from bottom)).

Estimation of apical dendrite length

Cell morphology reconstructions were downloaded from the Allen Cell Types database (*Dataset: Allen Institute for Brain Science*, 2015; Gouwens et al., 2019). Cells were selected by filtering the dataset for Nr5a1 or Scnn1a-Tg3 neurons recorded and filled from layer 4 of mouse primary visual cortex. Only cells where the primary branch of the apical dendrite was intact were used. Apical dendritic lengths were measured using the simple neurite tracer (SNT) plugin in ImageJ.

Allen Brain Observatory Visual Coding tuning preferences

To compare the tuning properties measured in this study to those measured from the Allen Brain Observatory 2PCI studies, we downloaded pre-computed tuning metrics of neurons from V1 layer 4 Nr5a1 and Scnn1a-Tg3 imaging experiments (*Dataset: Allen Institute MindScope Program*, 2016; de Vries et al., 2020). For orientation and direction tuning metrics,

we restricted the dataset to only neurons that were visually responsive to drifting grating experiments ($p<0.05$).

Experimental design and statistical analysis

For 2PCI, group differences were determined to be statistically significant by Wilcoxon Rank-Sum Test. For the correlation between preferred speed by coherent dots versus gratings, significance was determined by an F-test comparing the linear model versus a constant model (MATLAB fitlm function). Comparisons were considered significant if $p<0.05$.

2.4 Results

To determine if V1 layer 4 neurons labeled with two different mouse lines, Nr5a1-Cre and Scnn1a-Tg3-Cre, might differ in their locations, structure, or function, we first characterize the proportion and depth of layer 4 neurons each mouse line labeled (Figure 2.1). We also took advantage of a morphological dataset publicly available from the Allen Brain Atlas to measure differences in apical dendrite length (Figure 2.2). Next, given the morphological and anatomical differences that were observed, we then used 2PCI to characterize the functional tuning properties of Nr5a1versus Scnn1a-Tg3-Cre neurons in layer 4 of V1 for SF, TF, speed, and orientation/direction (Figure 2.3).

Layer 4 neurons labeled by mouse lines stratify different depths of layer 4 and have different apical dendrite lengths.

We crossed Nr5a1-Cre, Scnn1a-Tg3-Cre, and Nr5a1-Cre/Scnn1a-Tg3-Cre mice to an Ai14 reporter line that expresses Cre-dependent TdTomato (TdT) and stained coronal V1

sections for all neurons (anti-NeuN) and inhibitory neurons (anti-GAD67 or mDlx virus) in order to quantify the cells labeled by each mouse line separately and combined (Figure 2.1a). All Cre+ neurons were co-labeled with NeuN and no overlap was seen with inhibitory neurons, confirming that these mouse lines label excitatory cortical neurons. Across the depth of V1, Cre+ neurons in all mouse lines were concentrated between normalized depths of 0.3-0.5 from the pial surface, consistent with labelling primarily layer 4 neurons (Figure 2.1b). Interestingly, Nr5a1-Cre neurons were found more superficially in cortex, whereas Scnn1a-Tg3-Cre neurons were found deeper in cortex (Figure 2.1b). This trend was observed across all mouse sections. When calculating the proportion of excitatory layer 4 neurons labeled by each Cre line, we found that Nr5a1 labeled on average 9.5%, and Scnn1a-Tg3 labeled 49.3% (Figure 2.1c). When combined, Nr5a1/Scnn1a-Tg3-Cre+ neurons labeled 53.7% of layer 4, suggesting that there could be a small amount of overlap in layer 4 cells labeled by each mouse line. We also quantified the proportion of Cre+ neurons outside the borders of layer 4 and found some degree of labeling outside of layer 4 for each mouse line (Figure 2.1d), largely attributable to neurons near the layer 4 borders (Figure 2.1b).

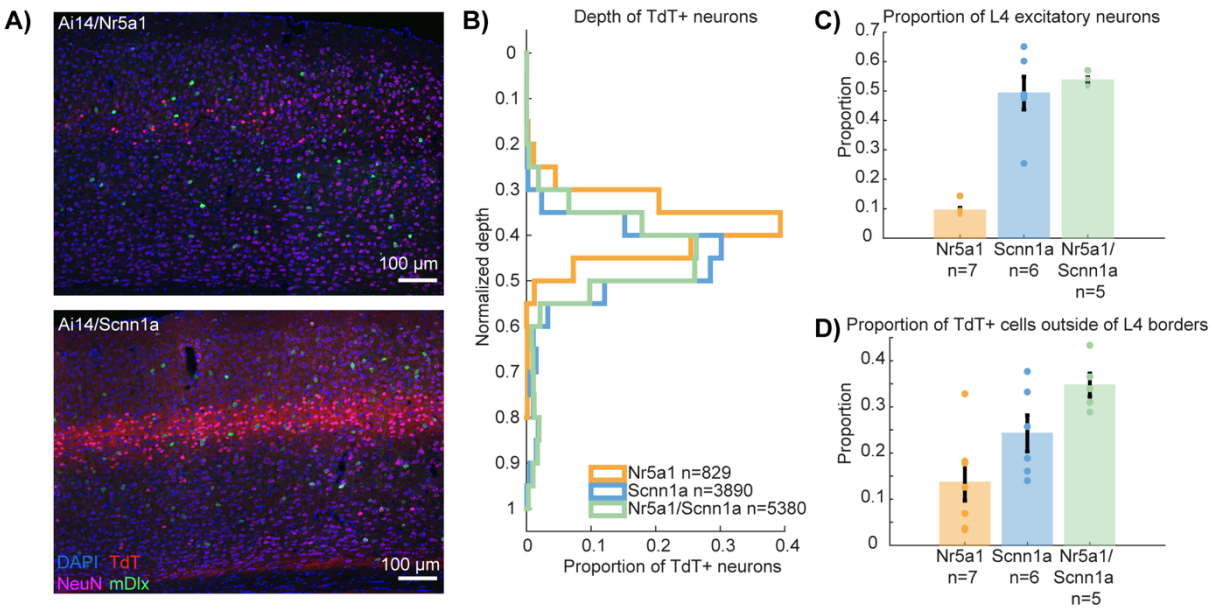

Figure 2.1: Quantification of proportion of layer 4 neurons labeled by Nr5a1 and Scnn1a-Tg3 mouse lines. (a) Sample section from z-stack images used for cell counting. Scale bar = 100 µm. (b) Normalized depth of TdT+ neurons in Ai14/Nr5a1, Ai14/Scnn1a-Tg3, and Ai14/Nr5a1/Scnn1a-Tg3 mice. n= total number of cells counted. (c) Proportion of excitatory neurons labeled by each Ai14 cross in layer 4. (d) Proportion of TdT+ neurons in each mouse line found outside of layer 4 borders. For (c) and (d), n = number of sections quantified. For (c) and (d) error bars represent standard error of the mean (sem).

To assess neuronal morphologies, we downloaded full apical dendrite reconstructions from the Allen Cell Types database of layer 4 Nr5a1 and Scnn1a-Tg3-Cre neurons in V1 (Figure 2.2a, inset) (*Dataset: Allen Institute for Brain Science*, 2015; Gouwens et al., 2019). Across many reconstructions, we noticed that most of the Nr5a1-Cre reconstructions had apical dendrites that often lacked an apical tuft, or had less extensive tufts. In contrast, many Scnn1a-Tg3-Cre reconstructions had more extensive apical tufts. To further quantify this, we measured the total apical dendrite length and found Scnn1a-Tg3 neurons had longer apical dendrite lengths compared to Nr5a1 neurons (Figure 2.2b, p=9.42e-4).

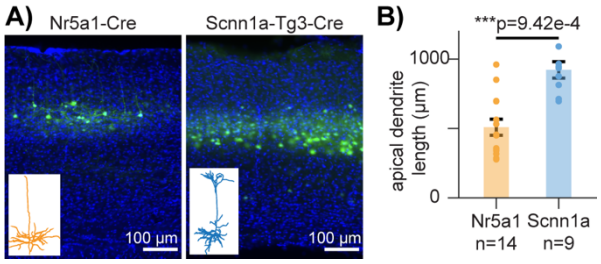

Figure 2.2: Two layer 4 transgenic mouse lines differ in apical dendrite length. (a) AAV1-FLEX-gCaMP6s expression in Nr5a1-Cre (left) and Scnn1a-Tg3-Cre (right) mice in V1. Scale bar = 100 µm. Inset images are sample dendrite reconstruction of a layer 4 cell from each mouse (Allen Brain Atlas Cell Types). (b) Apical dendritic length between Nr5a1 versus Scnn1a-Tg3 cells differ. Error bar represents standard error of the mean (sem). *p<0.05, **p<0.01, ***p<0.001, Wilcoxon Rank-Sum Test.

Nr5a1 and Scnn1a-Tg3 neurons are tuned for different spatiotemporal frequencies

Given the differences in cortical depths and apical dendrite length between Nr5a1-Cre and Scnn1a-Tg3-Cre neurons, we next tested whether these mouse lines labeled neurons tuned to different visual features (Figure 2.3). To compare the SF, TF, and speed tuning of Nr5a1 versus Scnn1a-Tg3 neurons, we presented drifting sine wave gratings at multiple combinations of SFs and TFs. While previous datasets from the Allen Brain Observatory have measured SF, TF tuning in the Nr5a1 and Scnn1a-Tg3-Cre mouse lines, these studies were done using a limited SF and TF sampling space that did not allow estimation of all SF, TF preferences or speed tuning and found only modest SF, TF differences between Nr5a1 and Scnn1a-Tg3 neurons (de Vries et al., 2020). Notably, SF tuning was assessed with flashed, static gratings, but previous studies have demonstrated that the preferred SF is dependent on the preferred TF and vice-versa, particularly for neurons that are speed tuned (Andermann et al., 2011; Movshon, 1975; Priebe et al., 2006).

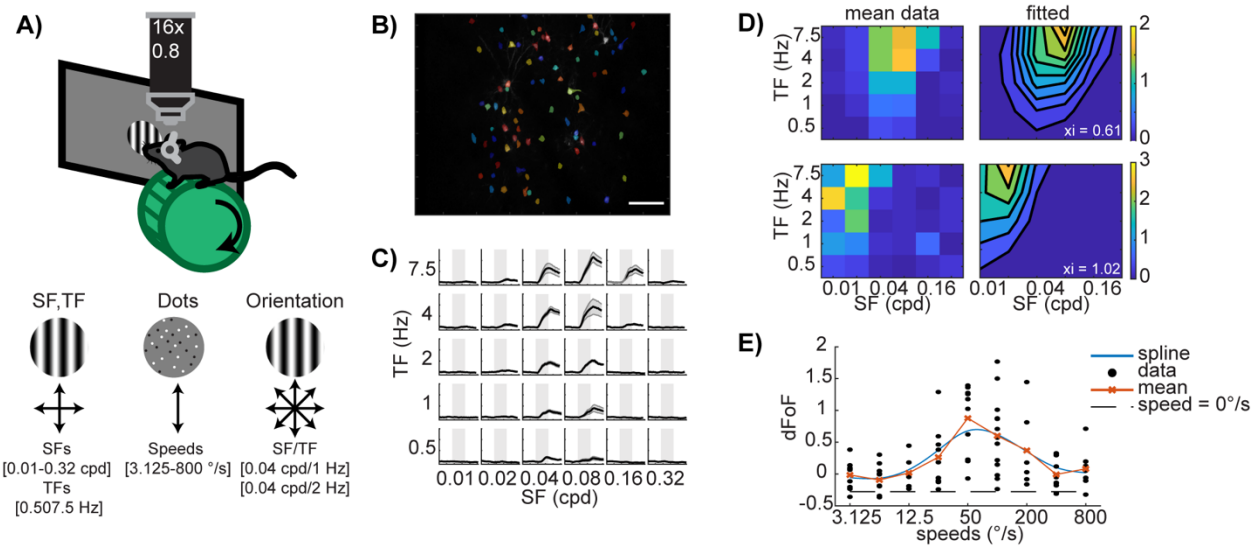

Figure 2.3: Summary of functional 2PCI, measurement, and analysis of tuning metrics for SF, TF, and speed. (a) 2PCI experimental setup. Top: schematic of 2PCI and visual stimulus setup. Bottom: diagram of stimulus sets used to measure tuning. Three different stimulus sets were used to measure SF tuning, TF tuning, speed tuning, and orientation/direction tuning. (b) sample field of view, with cell body region of interests segmented and pseudo-colored randomly. Scale bar = 100 µm. (c) Example dF/F responses to drifting gratings of different SF and TF combinations presented using the SF, TF stimulus set. Black line represents the mean response, gray shading surrounding the mean corresponds to the standard error of the mean. Shaded gray box corresponds to the 2 seconds stimulus presentation period. For each SF, TF combo x-axis is 0-6 seconds and y-axis is 0-6 dF/F. (d) Two example neurons (top and bottom row) and their fit to the 2-D Gaussian function. For each example, left is the mean dF/F response and right is the 2-D Gaussian fit. Fitted speed tuning slope (xi) is displayed in bottom right of each fit. (e) Example neuron response to dot motion and spline fit. Black dots are the individual trial dF/F responses, orange line is the mean response per combination of speed, dotted black line is the mean response to speed = 0 °/s, and blue line is the spline fit.

By sampling a greater range of SFs and TFs using drifting gratings, we found significant differences in the preferred SF, TF, and speed of Nr5a1 versus Scnn1a-Tg3 neurons. Nr5a1 neurons preferred lower SFs (median of 0.016 versus 0.046 cpd), higher TFs (median of 8.5 versus 1.1 Hz), and faster TF/SF ratios (median of 313.0 versus 23.3 °/s) (Figure 2.4a-c, p=5.53e-21, p=7.16e-41, p=1.52e-48) compared to Scnn1a-Tg3 neurons. We also calculated the preferred TF, SF, and TF/SF for all visually responsive neurons (not just neurons fit to the 2-D Gaussian function) and compared neurons from each line based on the stimulus condition that

elicited the strongest response. This analysis revealed comparable differences TF, SF, and TF/SF preferences between Nr5a1 and Scnn1a-Tg3-Cre neurons (Supplementary Figure S2.1).

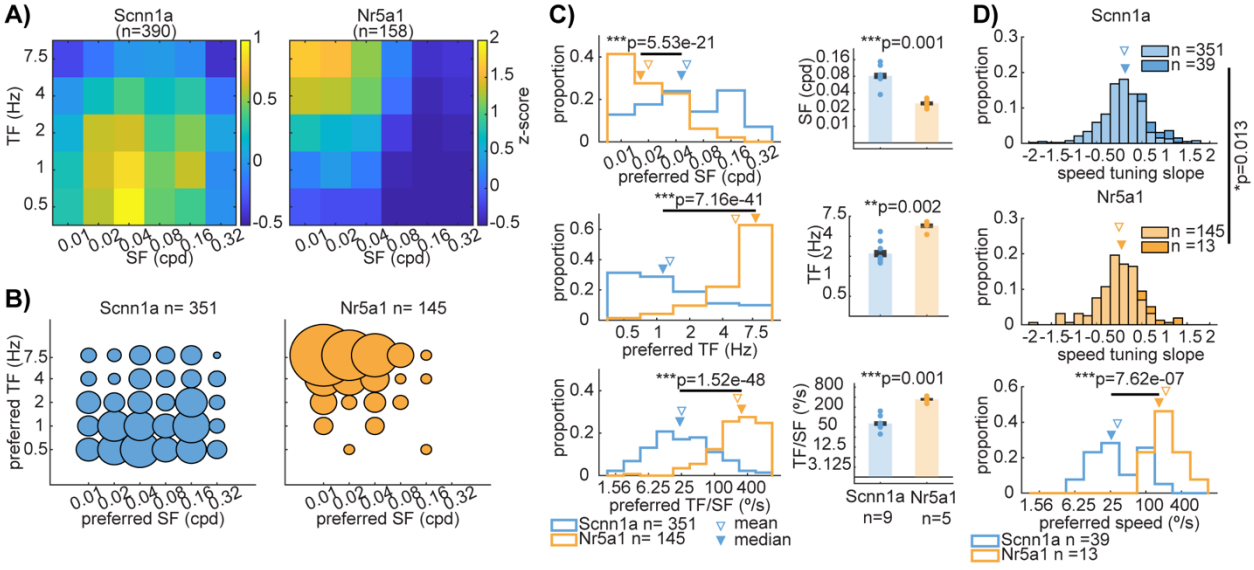

Figure 2.4: SF, TF, and speed tuning of Nr5a1 and Scnn1a-Tg3 neurons. (a) Mean z-scored responses at preferred orientation to SF, TF combinations presented for all neurons. (b) 2-D Histogram of preferred SF, TF combinations of non-speed tuned neurons. (c) Left: Histograms of preferred SF, TF, and TF/SF ratio of non-speed tuned neurons. Right: Mean preferred SF, TF, and TF/SF ratio per imaging session. Error bar denotes standard error (sem). (d) Top: Speed tuning index of Scnn1a-Tg3 versus Nr5a1 neurons. Lighter bars represent non-speed tuned neurons and darker bars represent speed tuned neurons. Bottom: preferred speed of speed tuned neurons. For (c) and (d), *p<0.05, **p<0.01, ***p<0.001, Wilcoxon Rank-Sum Test. For (c) and (d), filled triangles correspond to the median, and open triangles correspond to the mean of each distribution.

Nr5a1 and Scnn1a-Tg3 neurons are tuned for different speeds of visual motion

Because speed tuned neurons prefer a particular TF/SF ratio rather than a single SF or TF we also compared preferred speed for speed tuned neurons and found Nr5a1 neurons preferred faster speeds (Figure 2.4d bottom, p=7.62e-7). In both mouse lines, approximately 8-10% of well-fit neurons were considered speed tuned. However, Scnn1a-Tg3 neurons had slightly higher speed tuning slopes compared to Nr5a1 neurons (Figure 2.4d top, p= 0.013). We additionally measured preferred speed using coherent dot motion stimuli and found that while overall the proportion of neurons responsive to coherent dot motion was small (Table 2.1, Figure 2.5a),

neurons responsive to and well-fit by both dot and sine gratings measures of speed tuning were correlated in their preferred speed measured from each stimulus set (Figure 2.5a, p=3e-4). However, this linear fit was not significant when only fitting Scnn1a-Tg3 or Nr5a1 data on their own. Additionally, the direction of preferred speed was similar, with Nr5a1 neurons preferring faster speeds and higher lower and upper half max cutoffs for their speed tuning curves (Figure 2.5c,e p=5.9e-6, p=2.0e-5, p=2.7e-6). We also found that Nr5a1 neurons had slightly larger tuning half-widths compared to Scnn1a-Tg3 neurons (Figure 2.5d, p =0.003).

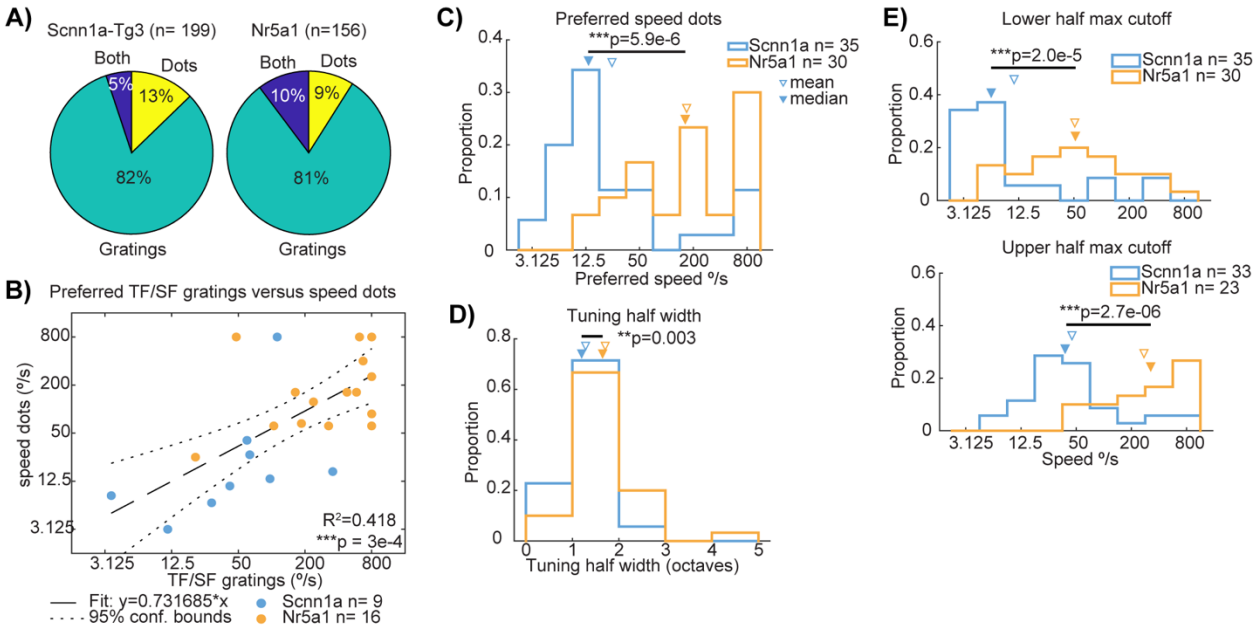

Figure 2.5: Coherent dot motion tuning preferences. (a) Proportion of neurons well-fit by speed tuning versus coherent motion speed or both. (b) Comparison of preferred speed as measured by sine wave gratings versus coherent dots for neurons fit and responsive to both stimuli. Linear model fit with intercept. (c) Preferred speed of all neurons responsive and well-fit to coherent motion stimulus. (d) Tuning half-width. (e) Upper and lower half-max cut offs for preferred speed by coherent motion stimulus. *p<0.05, **p<0.01, ***p<0.001. For (b) F-test, For (c)-(e) Wilcoxon Rank-Sum Test. For (c)-(e), filled triangles correspond to the median, and open triangles correspond to the mean of each distribution.

Differences in orientation and direction tuning

In a subset of mice, we additionally performed orientation and direction tuning experiments by presenting drifting gratings in 8 different directions. Because the preferred SF and TF of Nr5a1 versus Scnn1a-Tg3 neurons differed, we presented the gratings at different SF and TF combinations for each mouse line (see Methods). We additionally compared our orientation and direction selectivity findings to those from the Allen Brain Observatory Visual coding experiments (Figure 2.6b) (*Dataset: Allen Institute MindScope Program*, 2016; de Vries et al., 2020), where orientation and direction tuning were measured at multiple TFs using full field gratings, but at a fixed SF= 0.04 cpd. We found that while Scnn1a-Tg3 neurons were more orientation selective (Figure 2.6a top, p= 5.49e-6), Nr5a1 neurons were more direction selective (Figure 2.6a bottom, p = 1.51e-8). These differences in direction selectivity were consistent with direction tuning data from the Allen Brain Observatory Visual Coding experiments (Figure 2.6b bottom, p= 6.9e-4). While our comparison of differences in orientation selectivity differed from the findings of the Allen Brain Observatory dataset, we note that for both our study and theirs, that the mean and median OSI value did not differ by a large magnitude (Figure 2.6a, b top).

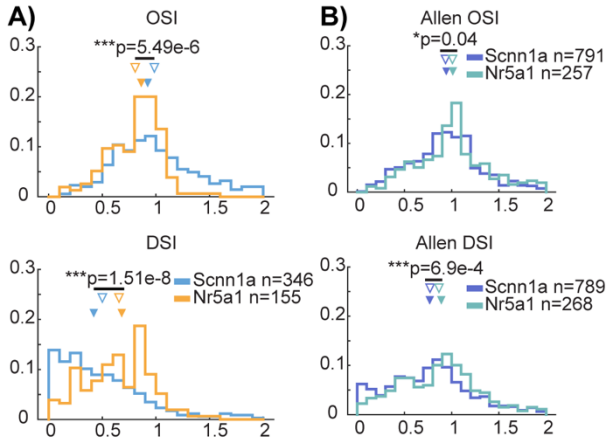

Figure 2.6: Orientation and direction tuning of Nr5a1 versus Scnn1a-Tg3 neurons. (a) Histogram of proportion of orientation and direction selectivity indices (top and bottom) of Nr5a1 versus Scnn1a-Tg3 neurons. (b) Same as (a) except from Allen Brain Observatory Visual Coding experiments. For (a) and (b) *p<0.05, **p<0.01, ***p<0.001, Wilcoxon Rank-Sum Test. Filled triangles correspond to the median, and open triangles correspond to the mean of each distribution.

2.5 Discussion

In primates, the early visual system from the retina, through the dLGN to V1 is organized into parallel magnocellular (M) and parvocellular (P) pathways composed of neurons tuned to different SFs and TFs. These different pathways originate from different RGC types responsive to coarse/fast versus fine/slow visual features (parasol versus midget cells) and remain segregated via different layers of the dLGN (magnocellular versus parvocellular layers) and different layers of V1 (layer 4Cα versus 4Cβ). Due to the lack of anatomical organization for most tuning properties in mouse V1, it is not clear if there are distinct layer 4 cell types that function like layer 4Cα and 4Cβ in primates. By characterizing two layer 4 mouse lines (Nr5a1-Cre and Scnn1a-Tg3-Cre) in V1, we identified layer 4 V1 neurons that differ in their cortical depth, apical dendrite length, and tuning properties for visual speed and direction. This suggests

that there is an organization for different SF, TF tuning in layer 4 of mouse V1, albeit less distinct compared to primate V1.

Anatomical and morphological differences in layer 4 visual cortex

We found that Nr5a1-Cre neurons are located more superficially in layer 4 and are tuned for faster visual speeds and higher TFs and lower SFs compared to Scnn1a-Tg3 neurons. Interestingly, neurons in primate layer 4 that receive input from high TF, low SF preferring magnocellular pathway are also located more superficially in layer 4Cα, whereas those that receive input from the low TF, high SF preferring parvocellular pathway are deeper in layer 4Cβ. Layer 4 is classically defined by the cytoarchitecture of cortex, where layer 4 is distinguished by dense Nissl cell labeling. Although different sub-layers of layer 4 are not identifiable in mouse V1 layer 4, it is intriguing to see this difference in laminar depth and tuning between these two mouse lines. This suggests that there is potentially a conversed laminar organization for layer 4 neurons tuned to these visual features.

In addition to different laminar depths, Nr5a1 and Scnn1a-Tg3-Cre neurons also differ in their apical dendrite length, with Scnn1a-Tg3-Cre neurons having longer apical dendrite lengths. This increased length may be due to increased numbers of apical dendrite tufts that are found in layer 1. Studies have identified 3 different morphologies for excitatory layer 4 neurons: spiny stellate, tufted pyramidal, and untufted (star) pyramidal (Staiger et al., 2004; Wang et al., 2018). In mouse V1, the majority of layer 4 cells are pyramidal, and very few are spiny stellate in morphology (Scala et al., 2019). Both tufted and untufted pyramidal neurons are found in mouse layer 4 (Harris et al., 2019). In our study, analysis of apical dendrite length from reconstructions found in the Allen Cell Types dataset (*Dataset: Allen Institute for Brain Science*, 2015; Gouwens

et al., 2019) suggests that Nr5a1-Cre and Scnn1a-Tg3-Cre neurons may be biased for different morphological cell types. Given the decreased apical dendrite length of Nr5a1-Cre neurons, Nr5a1 neurons may be biased towards untufted pyramidal neurons while Scnn1a-Tg3-Cre neurons may be biased towards tufted pyramidal neurons. Whether there is a functional or circuit difference between the tufted versus untufted pyramidal neurons in layer 4 is not known. In layer 5, neurons that project extratelencephalically have thicker apical dendrites and more extensive apical tufts compared to those that project intratelencelphalically (Hübener & Bolz, 1988; Kim et al., 2015). Characterization of the functional tuning properties of these neurons in V1 (Tlx3-Cre versus Glt25d2-Cre) also found differences in TF and direction tuning (Kim et al., 2015). The more extensive apical tufts in Scnn1a-Tg3-Cre neurons may allow these neurons to sample more inputs from layer 1 in addition to inputs in layer 4, which may be reflected in the differences in visual tuning preferences.

Functional differences in visual tuning of layer 4 visual cortex

Using two different types of visual stimuli for measuring responses to visual speed, we found that Nr5a1 neurons prefer faster speeds compared to Scnn1a-Tg3 neurons. Nr5a1 neurons also preferred lower SFs and higher TFs compared to Scnn1a-Tg3 neurons. While the preferred TF/SF ratio can be used as an estimate of a neuron's preferred speed, this ratio is dependent on the preferred TF and SF of the neuron. Neurons that are truly speed tuned prefer the same speed (TF/SF) regardless of the TF and SF (Movshon, 1975). Theories for how speed tuning emerges hypothesize that speed tuned neurons sum spatiotemporal frequency energy along "iso-speed" lines (Adelson & Bergen, 1985). We find that when measuring speed tuning using coherent dot motion stimuli, which consist of multiple SFs and TFs, the bias for fast versus slow speeds in Nr5a1 versus Scnn1a-Tg3-Cre neurons persists. We also find that Nr5a1-Cre neurons are more

direction selective, which is consistent with another study that also measured direction tuning in Nr5a1 and Scnn1a-Tg3-Cre neurons (*Dataset: Allen Institute MindScope Program*, 2016; de Vries et al., 2020). The higher direction selectivity and preference from faster speeds may reflect a greater role for Nr5a1-Cre neurons in motion-related visual information compared to Scnn1a-Tg3-Cre neurons.

Layer 4 cell types – morphological versus functional versus transcriptomic identity

Single cell RNA sequencing studies have revealed many new cell types, but the role of these new cell types and how they may relate to morphological or functional types is at times unclear. It is also unclear to what extent some cell types can be discretely separated from others. In layer 4 of mouse V1, cell identity may lie more on a gradient of transcriptomic identity rather than in a single laminar identity (Tasic et al., 2018). While the Scnn1a-Tg3-Cre and Nr5a1-Cre cells have been previously sequenced (Tasic et al., 2016, 2018), it is not clear if they have different or multiple transcriptomic identities. In Tasic et al. 2016, Nr5a1 and Scnn1a-Tg3 neurons were both found in all three of the layer 4 transcriptomic groups identified, but the proportion of each line found in each group differed slightly. In Tasic et al. 2018, only one layer 4 cluster was identified, although the study found a great deal of continuous heterogeneity within the cluster that was not further separated. Additionally, while Nr5a-Cre neurons were found in a single layer 4 transcriptomic cluster in Tasic et al. 2018, the same Nr5a1-Cre neurons were found in multiple different morphological and electrophysiological groups in Gouwens et al. 2019. It will be interesting in future studies to identify if there are differentially expressed genes between Scnn1a-Tg3-Cre and Nr5a1-Cre neurons and how they may relate to functional and morphological differences.

Our cell counting quantification of the Nr5a1-Cre, Scnn1a-Tg3-Cre, and Nr5a1/Scnn1a-Tg3-Cre crossed mouse lines demonstrates that not all layer 4 excitatory neurons are accounted for, and that there may be some overlap in the layer 4 cells labeled with these two mouse lines. For both mice, there is also a fraction of neurons that are labeled outside of layer 4, as evidenced by the location of Cre+ neurons in our study, and transcriptomic clustering in other studies (we note that the Nr5a1-Cre mouse line appears more specific for layer 4 compared to Scnn1a-Tg3 in these transcriptomic studies (Tasic et al., 2016, 2018)). However, the functional and morphological properties of Cre+ layer 4 neurons in these mice from our study and others suggest that these mouse lines are at least biased toward layer 4 cells with different morphological and functional properties, even if incomplete in their labeling. Additional studies using these mouse lines and other strategies for targeting layer 4 may more clearly identify how many layer 4 mouse V1 cell types are present and help develop new methods that more completely and specifically target layer 4 cells in V1.

Organization of layer 4 inputs

What could underlie these differences in tuning properties between Nr5a1-Cre and Scnn1a-Tg3-Cre neurons? One explanation for the differences in functional tuning properties of these two neurons could be differences in inputs from RGCs and the dLGN. Previous studies have identified a direct circuit from direction selective RGCs (DS-RGCs) through the dLGN shell to layer 1 of V1 (Bickford et al., 2015; Cruz-Martín et al., 2014; Huberman et al., 2009). Another study where DS-RGCs were inactivated demonstrated that some direction selectivity in V1 can be directly inherited from these DS-RGCs (Hillier et al., 2017). However, outside the core and shell distinction, it is not clear if there is an anatomical organization for different dLGN

neurons in rodents (Reese, 1988). In the dLGN core, neurons with different properties appear to be intermingled (Piscopo et al., 2013). While inputs to layer 1 from dLGN shell may influence functional tuning of deeper layer neurons that extend their apical dendrites to layer 1, the primary dLGN input to layer 4 of V1 arises from the dLGN core. Whether layer 4 neurons that differ in their functional tuning properties receive input from different dLGN core neurons or different RGCs remains to be resolved. In mice, there are approximately 30 distinct RGC types (Baden et al., 2016; Sanes & Masland, 2015). Characterization of these RGCs' functional properties demonstrates that there are several classes of RGCs that respond to different SFs and TFs (Baden et al., 2016). Thus, the differences in SF, TF tuning we see in Nr5a1 and Scnn1a-Tg3-Cre neurons may be due to different RGC inputs. Additionally, differences in direction selectivity between the two mouse lines also suggest differences in direction selective input, either through layer 1 or layer 4 (Cruz-Martín et al., 2014; Kondo & Ohki, 2016; Sun et al., 2015; Zhuang et al., 2021). Direction selectivity can also emerge *de novo* in layer 4 of V1 (Lien & Scanziani, 2018), so not all direction selective differences may be due to differences in dLGN cell or RGC type input.

Studies looking at RGC input to the dLGN reveal two modes of input, termed "relay" mode and "combination" mode. dLGN neurons that receive relay mode input typically receive input from 1-2 types of RGCs, whereas neurons that receive combination mode input receive input from multiple RGC types (Liang et al., 2018; Rompani et al., 2017). It is possible that dLGN neurons that receive combination mode input may integrate different functional information from different RGCs and provide novel tuning properties to V1 rather than simply passing on RGC properties to V1 (Marshel et al., 2012). In this case, tuning differences in Nr5a1 versus Scnn1a-Tg3-Cre neurons may reflect different modes of integration in dLGN rather than

different RGC types. The role of relay versus combination mode input in dLGN and its impact on the visual properties inherited in V1 is currently not well understood. Additional anatomical studies that trace the dLGN and RGC inputs to these functionally biased layer 4 neurons to determine how these differences in tuning properties arise would be interesting.

Overall, we have conducted a thorough functional characterization of the visual response properties of layer 4 neurons labeled by the Nr5a1-Cre and Scnn1a-Tg3-Cre mouse lines. These neurons not only differ in tuning properties for SF, TF, speed, and direction, but also differ in their apical dendrite length and laminar location. This suggests that these mouse lines are biased toward two different groups of layer 4 neurons. Further functional and anatomical studies with these mouse lines may reveal how spatiotemporal frequency tuning is organized in the mouse visual system and if parallel visual pathways from the retina and dLGN are a conserved organizing principle.

2.6 Tables and Appendix

Table 2.1: 2-Photon experiments summary numbers. Summary of animals, imaging sessions (expts), and cells (ROIs) used in calculating tuning preferences.

STF Experiments							
Strain	Animals	Expts	ROIs	resp	% resp	speed fit	%fit
Nr5a1	5	5	558	285	51%	158	55%
Scnn1a-Tg3	7	9	4503	1426	32%	390	27%
Coherent Motion Experiments							
Strain	Animals	Expts	ROIs	resp	% resp	speed fit	%fit
Nr5a1	4	4	327	54	17%	30	56%
Scnn1a-Tg3	3	5	1915	211	11%	35	17%
Orientation Experiments							
Strain	Animals	Expts	ROIs	resp	% resp		
Nr5a1	4	4	327	158	48%		
Scnn1a-Tg3	3	5	1915	395	21%		

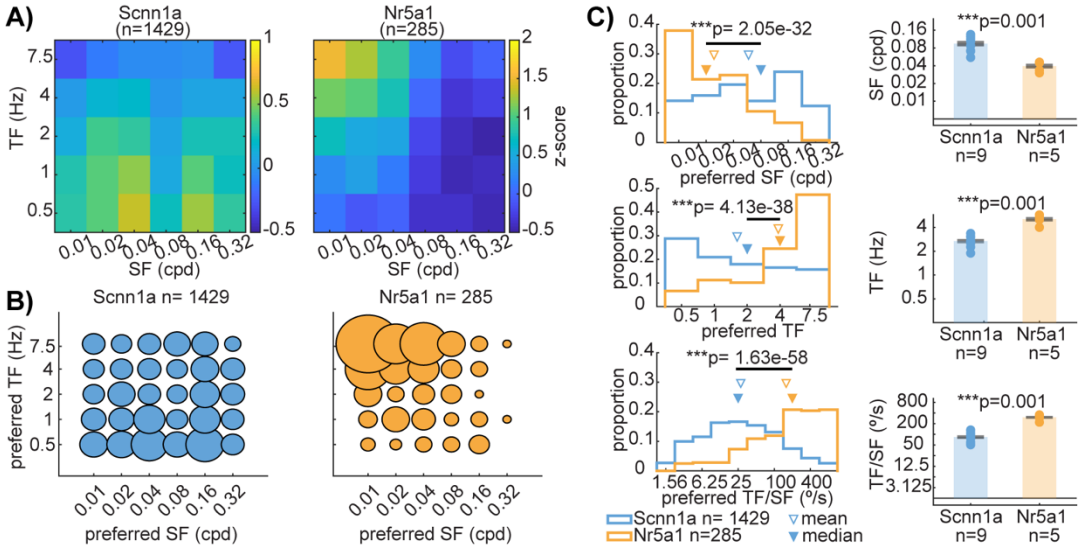

Supplementary Figure S2.1: SF, TF, and TF/SF tuning preferences for all visually responsive neurons. (a) Mean z-scored responses to SF, TF combinations presented at each neurons preferred direction. (b) 2-D histogram of preferred SF, TF combination for all responsive neurons. (c) Top to bottom: SF, TF, and TF/SF tuning preferences. Left: histograms of tuning preferences across all visually responsive neurons. Right: mean tuning preferences averaged per imaging session. Error bar denotes standard error (sem). *p<0.05, **p<0.01, ***p<0.001, Wilcoxon Rank-Sum Test. For (c), filled triangles correspond to the median, and open triangles correspond to the mean of each distribution.

2.7 Acknowledgements

This work was supported by the NIH grants EY029932 (HW), EY022577 (EMC), and EY031517 (BKS). Chapter 2, in full, is currently being prepared for submission for publication and will include Oyshi Dey, Willian N. Lagos, and Noor Behnam as co-authors and Professor Edward Callaway and Dr. Benjamin K. Stafford as co-senior authors. The dissertation author was the primary investigator and author of this material.

2.8 References

Adelson, E. H., & Bergen, J. R. (1985). Spatiotemporal energy models for the perception of motion. J. Opt. Soc. Am. A, 2(2).

Andermann, M. L., Kerlin, A. M., Roumis, D. K., Glickfeld, L. L., & Reid, R. C. (2011). Functional specialization of mouse higher visual cortical areas. Neuron, 72(6), 1025–1039. https://doi.org/10.1016/j.neuron.2011.11.013

Baden, T., Berens, P., Franke, K., Román Rosón, M., Bethge, M., & Euler, T. (2016). The functional diversity of retinal ganglion cells in the mouse. Nature, 529(7586), 345–350. https://doi.org/10.1038/nature16468

Bickford, M. E., Zhou, N., Krahe, T. E., Govindaiah, G., & Guido, W. (2015). Retinal and Tectal "Driver-Like" Inputs Converge in the Shell of the Mouse Dorsal Lateral Geniculate Nucleus. Journal of Neuroscience, 35(29), 10523–10534. https://doi.org/10.1523/JNEUROSCI.3375-14.2015

Cruz-Martín, A., El-Danaf, R. N., Osakada, F., Sriram, B., Dhande, O. S., Nguyen, P. L., Callaway, E. M., Ghosh, A., & Huberman, A. D. (2014). A dedicated circuit links direction-selective retinal ganglion cells to the primary visual cortex. Nature, 507(7492), 358–361. https://doi.org/10.1038/nature12989

Dataset: Allen Institute for Brain Science. (2015). Allen Cell Types Database -- Mouse Morphology-Electrophysiology [dataset]. celltypes.brain-map.org/data. RRID:SCR_014806

Dataset: Allen Institute MindScope Program. (2016). Allen Brain Observatory -- 2-photon Visual Coding [dataset]. brain-map.org/explore/circuits

de Vries, S. E. J., Lecoq, J. A., Buice, M. A., Groblewski, P. A., Ocker, G. K., Oliver, M., Feng, D., Cain, N., Ledochowitsch, P., Millman, D., Roll, K., Garrett, M., Keenan, T., Kuan, L., Mihalas, S., Olsen, S., Thompson, C., Wakeman, W., Waters, J., Williams, D., Barber, C., Berbesque, N., Blanchard, B., Bowles, N., Caldejon, S. D., Casal, L., Cho, A., Cross, S., Dang, C., Dolbeare, T., Edwards, M., Galbraith, J., Gaudreault, N., Gilbert, T. L., Griffin, F., Hargrave, P., Howard, R., Huang, L., Jewell, S., Keller, N., Knoblich, U., Larkin, J. D., Larsen, R., Lau, C., Lee, E., Lee, F., Leon, A., Li, L., Long, F., Luviano, J., Mace, K., Nguyen, T., Perkins, J., Robertson, M., Seid, S., Shea-Brown, E., Shi, J., Sjoquist, N., Slaughterbeck, C., Sullivan, D., Valenza, R., White, C., Williford, A., Witten, D. M., Zhuang, J., Zeng, H., Farrell, C., Ng, L., Bernard, A., Phillips, J. W., Reid, R. C., & Koch, C. (2020). A large-scale standardized physiological survey reveals functional organization of the mouse visual cortex. Nature Neuroscience, 23(1), 138–151. https://doi.org/10.1038/s41593-019-0550-9

DeFelipe, J., & Fariñas, I. (1992). The pyramidal neuron of the cerebral cortex: Morphological and chemical characteristics of the synaptic inputs. Progress in Neurobiology, 39(6), 563–607. https://doi.org/10.1016/0301-0082(92)90015-7

Gao, E., DeAngelis, G. C., & Burkhalter, A. (2010). Parallel Input Channels to Mouse Primary Visual Cortex. Journal of Neuroscience, 30(17), 5912–5926. https://doi.org/10.1523/JNEUROSCI.6456-09.2010

Gouwens, N. W., Sorensen, S. A., Berg, J., Lee, C., Jarsky, T., Ting, J., Sunkin, S. M., Feng, D., Anastassiou, C. A., Barkan, E., Bickley, K., Blesie, N., Braun, T., Brouner, K., Budzillo, A., Caldejon, S., Casper, T., Castelli, D., Chong, P., Crichton, K., Cuhaciyan, C., Daigle, T. L., Dalley, R., Dee, N., Desta, T., Ding, S.-L., Dingman, S., Doperalski, A., Dotson, N., Egdorf, T., Fisher, M., de Frates, R. A., Garren, E., Garwood, M., Gary, A., Gaudreault, N., Godfrey, K., Gorham, M., Gu, H., Habel, C., Hadley, K., Harrington, J., Harris, J. A., Henry, A., Hill, D., Josephsen, S., Kebede, S., Kim, L., Kroll, M., Lee, B., Lemon, T., Link, K. E., Liu, X., Long, B., Mann, R., McGraw, M., Mihalas, S., Mukora, A., Murphy, G. J., Ng, L., Ngo, K., Nguyen, T. N., Nicovich, P. R., Oldre, A., Park, D., Parry, S., Perkins, J., Potekhina, L., Reid, D., Robertson, M., Sandman, D., Schroedter, M., Slaughterbeck, C., Soler-Llavina, G., Sulc, J., Szafer, A., Tasic, B., Taskin, N., Teeter, C., Thatra, N., Tung, H., Wakeman, W., Williams, G., Young, R., Zhou, Z., Farrell, C., Peng, H., Hawrylycz, M. J., Lein, E., Ng, L., Arkhipov, A., Bernard, A., Phillips, J. W., Zeng, H., & Koch, C. (2019). Classification of electrophysiological and morphological neuron types in the mouse visual cortex. Nature Neuroscience, 22(7), 1182–1195. https://doi.org/10.1038/s41593-019-0417-0

Harris, J. A., Mihalas, S., Hirokawa, K. E., Whitesell, J. D., Choi, H., Bernard, A., Bohn, P., Caldejon, S., Casal, L., Cho, A., Feiner, A., Feng, D., Gaudreault, N., Gerfen, C. R., Graddis, N., Groblewski, P. A., Henry, A. M., Ho, A., Howard, R., Knox, J. E., Kuan, L., Kuang, X., Lecoq, J., Lesnar, P., Li, Y., Luviano, J., Mcconoughey, S., Mortrud, M. T., Naeemi, M., Ng, L., Oh, S. W., Ouellette, B., Shen, E., Sorensen, S. A., Wakeman, W., Wang, Q., Wang, Y., Williford, A., Phillips, J. W., Jones, A. R., Koch, C., & Zeng, H. (2019). Hierarchical organization of cortical and thalamic connectivity. Nature, 575(7781), 195–202. https://doi.org/10.1038/s41586-019-1716-z

Hillier, D., Fiscella, M., Drinnenberg, A., Trenholm, S., Rompani, S. B., Raics, Z., Katona, G., Juettner, J., Hierlemann, A., Rozsa, B., & Roska, B. (2017). Causal evidence for retina-dependent and -independent visual motion computations in mouse cortex. Nature Neuroscience, 20(7), 960–968. https://doi.org/10.1038/nn.4566

Hübener, M., & Bolz, J. (1988). Morphology of identified projection neurons in layer 5 of rat visual cortex. Neuroscience Letters, 94(1–2), 76–81. https://doi.org/10.1016/0304-3940(88)90273-x

Huberman, A. D., Wei, W., Elstrott, J., Stafford, B. K., Feller, M. B., & Barres, B. A. (2009). Genetic Identification of an On-Off Direction- Selective Retinal Ganglion Cell Subtype Reveals a Layer-Specific Subcortical Map of Posterior Motion. Neuron, 62(3), 327–334. https://doi.org/10.1016/j.neuron.2009.04.014

Kerlin, A. M., Andermann, M. L., Berezovskii, V. K., & Reid, R. C. (2010). Broadly Tuned Response Properties of Diverse Inhibitory Neuron Subtypes in Mouse Visual Cortex. Neuron, 67(5), 858–871. https://doi.org/10.1016/j.neuron.2010.08.002

Kim, E. J., Juavinett, A. L., Kyubwa, E. M., Jacobs, M. W., & Callaway, E. M. (2015). Three Types of Cortical Layer 5 Neurons That Differ in Brain-wide Connectivity and Function. Neuron, 88(6), 1253–1267. https://doi.org/10.1016/j.neuron.2015.11.002

Kondo, S., & Ohki, K. (2016). Laminar differences in the orientation selectivity of geniculate afferents in mouse primary visual cortex. Nature Neuroscience, 19(2), 316–319. https://doi.org/10.1038/nn.4215

Liang, L., Fratzl, A., Goldey, G., Ramesh, R. N., Sugden, A. U., Morgan, J. L., Chen, C., & Andermann, M. L. (2018). A Fine-Scale Functional Logic to Convergence from Retina to Thalamus. Cell, 173(6), 1343-1355.e24. https://doi.org/10.1016/j.cell.2018.04.041

Lien, A. D., & Scanziani, M. (2018). Cortical direction selectivity emerges at convergence of thalamic synapses. Nature, 1. https://doi.org/10.1038/s41586-018-0148-5

Marshel, J. H., Garrett, M. E., Nauhaus, I., & Callaway, E. M. (2011). Functional specialization of seven mouse visual cortical areas. Neuron, 72(6), 1040–1054. https://doi.org/10.1016/j.neuron.2011.12.004

Marshel, J. H., Kaye, A. P., Nauhaus, I., & Callaway, E. M. (2012). Anterior-Posterior Direction Opponency in the Superficial Mouse Lateral Geniculate Nucleus. Neuron, 76(4), 713–720. https://doi.org/10.1016/j.neuron.2012.09.021

Movshon, J. A. (1975). The velocity tuning of single units in cat striate cortex. The Journal of Physiology, 249(3), 445–468. https://doi.org/10.1113/jphysiol.1975.sp011025

Nassi, J. J., & Callaway, E. M. (2009). Parallel processing strategies of the primate visual system. Nature Reviews Neuroscience, 10(5), 360–372. https://doi.org/10.1038/nrn2619

Niell, C. M., & Stryker, M. P. (2008). Highly Selective Receptive Fields in Mouse Visual Cortex. Journal of Neuroscience, 28(30), 7520–7536. https://doi.org/10.1523/JNEUROSCI.0623-08.2008

Niell, C. M., & Stryker, M. P. (2010). Modulation of Visual Responses by Behavioral State in Mouse Visual Cortex. Neuron, 65(4), 472–479. https://doi.org/10.1016/j.neuron.2010.01.033

Ohki, K., Chung, S., Ch'ng, Y. H., Kara, P., & Reid, R. C. (2005). Functional imaging with cellular resolution reveals precise micro-architecture in visual cortex. Nature, 433(7026), 597–603. https://doi.org/10.1038/nature03274

Ohki, K., & Reid, R. C. (2007). Specificity and randomness in the visual cortex. Current Opinion in Neurobiology, 17(4), 401–407. https://doi.org/10.1016/j.conb.2007.07.007

Pachitariu, M., Stringer, C., Schröder, S., Dipoppa, M., Rossi, L. F., Carandini, M., & Harris, K. D. (2016). Suite2p: Beyond 10,000 neurons with standard two-photon microscopy. BioRxiv, 061507. https://doi.org/10.1101/061507

Piscopo, D. M., El-Danaf, R. N., Huberman, A. D., & Niell, C. M. (2013). Diverse Visual Features Encoded in Mouse Lateral Geniculate Nucleus. Journal of Neuroscience, 33(11), 4642–4656. https://doi.org/10.1523/JNEUROSCI.5187-12.2013

Priebe, N. J., Cassanello, C. R., & Lisberger, S. G. (2003). The neural representation of speed in macaque area MT/V5. The Journal of Neuroscience, 23(13), 5650–5661. https://doi.org/23/13/5650 [pii]

Priebe, N. J., Lisberger, S. G., & Movshon, J. A. (2006). Tuning for Spatiotemporal Frequency and Speed in Directionally Selective Neurons of Macaque Striate Cortex. Journal of Neuroscience, 26(11), 2941–2950. https://doi.org/10.1523/JNEUROSCI.3936-05.2006

Reese, B. E. (1988). 'Hidden lamination' in the dorsal lateral geniculate nucleus: The functional organization of this thalamic region in the rat. Brain Research Reviews, 13(2), 119–137. https://doi.org/10.1016/0165-0173(88)90017-3

Rompani, S. B., Müllner, F. E., Wanner, A., Zhang, C., Roth, C. N., Yonehara, K., & Roska, B. (2017). Different Modes of Visual Integration in the Lateral Geniculate Nucleus Revealed by Single-Cell-Initiated Transsynaptic Tracing. Neuron, 93(4), 767-776.e6. https://doi.org/10.1016/j.neuron.2017.01.028

Sanes, J. R., & Masland, R. H. (2015). The Types of Retinal Ganglion Cells: Current Status and Implications for Neuronal Classification. Annual Review of Neuroscience, 38(1), 221–246. https://doi.org/10.1146/annurev-neuro-071714-034120

Scala, F., Kobak, D., Shan, S., Bernaerts, Y., Laturnus, S., Cadwell, C. R., Hartmanis, L., Froudarakis, E., Castro, J. R., Tan, Z. H., Papadopoulos, S., Patel, S. S., Sandberg, R., Berens, P., Jiang, X., & Tolias, A. S. (2019). Layer 4 of mouse neocortex differs in cell types and circuit organization between sensory areas. Nature Communications, 10(1). https://doi.org/10.1038/s41467-019-12058-z

Siegle, J. H., Jia, X., Durand, S., Gale, S., Bennett, C., Graddis, N., Heller, G., Ramirez, T. K., Choi, H., Luviano, J. A., Groblewski, P. A., Ahmed, R., Arkhipov, A., Bernard, A., Billeh, Y. N., Brown, D., Buice, M. A., Cain, N., Caldejon, S., Casal, L., Cho, A., Chvilicek, M., Cox, T. C., Dai, K., Denman, D. J., de Vries, S. E. J., Dietzman, R., Esposito, L., Farrell, C., Feng, D., Galbraith, J., Garrett, M., Gelfand, E. C., Hancock, N., Harris, J. A., Howard, R., Hu, B., Hytnen, R., Iyer, R., Jessett, E., Johnson, K., Kato, I., Kiggins, J., Lambert, S., Lecoq, J., Ledochowitsch, P., Lee, J. H., Leon, A., Li, Y., Liang, E., Long, F., Mace, K., Melchior, J., Millman, D., Mollenkopf, T., Nayan, C., Ng, L., Ngo, K., Nguyen, T., Nicovich, P. R., North, K., Ocker, G. K., Ollerenshaw, D., Oliver, M., Pachitariu, M., Perkins, J., Reding, M., Reid, D., Robertson, M., Ronellenfitch, K., Seid, S., Slaughterbeck, C., Stoecklin, M., Sullivan, D., Sutton, B., Swapp, J., Thompson, C., Turner, K., Wakeman, W., Whitesell, J. D., Williams, D., Williford, A., Young, R., Zeng, H., Naylor, S., Phillips, J. W., Reid, R. C., Mihalas, S., Olsen, S. R., & Koch, C. (2021). Survey of spiking in the mouse visual system reveals functional hierarchy. Nature, 592(7852), 86–92. https://doi.org/10.1038/s41586-020-03171-x

Staiger, J. F., Flagmeyer, I., Schubert, D., Zilles, K., Kötter, R., & Luhmann, H. J. (2004). Functional diversity of layer IV spiny neurons in rat somatosensory cortex: Quantitative

morphology of electrophysiologically characterized and biocytin labeled cells. Cerebral Cortex, 14(6), 690–701. https://doi.org/10.1093/cercor/bhh029

Sun, W., Tan, Z., Mensh, B. D., & Ji, N. (2015). Thalamus provides layer 4 of primary visual cortex with orientation- and direction-tuned inputs. Nature Neuroscience, 19(2), 308–315. https://doi.org/10.1038/nn.4196

Tasic, B., Menon, V., Nguyen, T. N., Kim, T. K., Jarsky, T., Yao, Z., Levi, B., Gray, L. T., Sorensen, S. A., Dolbeare, T., Bertagnolli, D., Goldy, J., Shapovalova, N., Parry, S., Lee, C., Smith, K., Bernard, A., Madisen, L., Sunkin, S. M., Hawrylycz, M., Koch, C., & Zeng, H. (2016). Adult mouse cortical cell taxonomy revealed by single cell transcriptomics. Nature Neuroscience, 19(2), 335–346. https://doi.org/10.1038/nn.4216

Tasic, B., Yao, Z., Graybuck, L. T., Smith, K. A., Nguyen, T. N., Bertagnolli, D., Goldy, J., Garren, E., Economo, M. N., Viswanathan, S., Penn, O., Bakken, T., Menon, V., Miller, J., Fong, O., Hirokawa, K. E., Lathia, K., Rimorin, C., Tieu, M., Larsen, R., Casper, T., Barkan, E., Kroll, M., Parry, S., Shapovalova, N. V., Hirschstein, D., Pendergraft, J., Sullivan, H. A., Kim, T. K., Szafer, A., Dee, N., Groblewski, P., Wickersham, I., Cetin, A., Harris, J. A., Levi, B. P., Sunkin, S. M., Madisen, L., Daigle, T. L., Looger, L., Bernard, A., Phillips, J., Lein, E., Hawrylycz, M., Svoboda, K., Jones, A. R., Koch, C., & Zeng, H. (2018). Shared and distinct transcriptomic cell types across neocortical areas. Nature, 563(7729), 72–78. https://doi.org/10.1038/s41586-018-0654-5

Wang, Y., Ye, M., Kuang, X., Li, Y., & Hu, S. (2018). A simplified morphological classification scheme for pyramidal cells in six layers of primary somatosensory cortex of juvenile rats. IBRO Reports, 5(October), 74–90. https://doi.org/10.1016/j.ibror.2018.10.001

Zhuang, J., Wang, Y., Ouellette, N. D., Turschak, E. E., Larsen, R. S., Takasaki, K. T., Daigle, T. L., Tasic, B., Waters, J., Zeng, H., & Reid, R. C. (2021). Laminar distribution and arbor density of two functional classes of thalamic inputs to primary visual cortex. Cell Reports, 37(2), 109826. https://doi.org/10.1016/j.celrep.2021.109826